Research Paper

GEOSPHERE

GEOSPHERE

https://doi.org/10.1130/GES02613.1

15 figures; 3 tables; 1 set of supplemental files

CORRESPONDENCE: Rosie.Cobbett@yukon.ca

CITATION: Cobbett, R.N., Beranek, L.P., Piercey, S.J., Crowley, J.L., and Colpron, M., 2023, Early Ordovician seamounts preserved in the Canadian Cordillera: Implications for the rift history of western Laurentia: Geosphere, https://doi.org/10.1130/GES02613.1.

Science Editor: Christopher J. Spencer
Associate Editor: Nancy Riggs

Received 17 October 2022
Revision received 3 May 2023
Accepted 23 May 2023

Published online 18 August 2023

Early Ordovician seamounts preserved in the Canadian Cordillera: Implications for the rift history of western Laurentia

Rose N. Cobbett[1,2], Luke P. Beranek[1], Stephen J. Piercey[1], James L. Crowley[3], and Maurice Colpron[2]

[1]Department of Earth Sciences, Memorial University of Newfoundland, 9 Arctic Avenue, St. John's, Newfoundland and Labrador A1B 3X5, Canada
[2]Yukon Geological Survey, PO Box 2703 (K14), Whitehorse, Yukon Y1A 2C6, Canada
[3]Department of Geosciences, Boise State University, 295 University Drive, Boise, Idaho 83706, USA

ABSTRACT

The breakup of the supercontinent Rodinia and development of the western Laurentian rifted margin are in part recorded by Neoproterozoic to mid-Paleozoic igneous and sedimentary rock successions in the Canadian Cordillera. New bedrock mapping and volcanic facies analysis of Early Ordovician mafic rocks assigned to the Menzie Creek Formation in central Yukon allow reconstruction of the depositional environment during the volcanic eruptions, whole-rock geochemical data constrain the melting depth and crust-mantle source regions of the igneous rocks within the study area, and zircon U-Pb age studies provide determination of the precise timing of submarine eruptions. Menzie Creek Formation volcanic rocks are interlayered with continental slope strata and show lithofacies consistent with those of modern seamount systems. Representative seamount facies contain several kilometers of hyaloclastite breccia and pillow basalt with rare sedimentary rocks. Menzie Creek Formation seamounts form a linear array parallel to the Twopete fault, an ancient extensional or strike-slip fault that localized magmatism along the nascent western Laurentian margin. Zircon grains from two volcanic successions yielded high-precision chemical abrasion–thermal ionization mass spectrometry (CA-TIMS) dates of ca. 484 Ma (Tremadocian), which are interpreted as the age of eruption. Menzie Creek Formation rocks are alkali basalt and have oceanic-island basalt–like geochemical compositions. The whole-rock trace element and Nd-Hf isotope compositions are consistent with the partial melting of subcontinental lithospheric mantle at ~75–100 km depth. Post-rift, Early Ordovician seamounts in central Yukon record punctuated eruptive activity along a rift-related fault, the separation of a continental fragment from western Laurentia, or the oblique post-breakup kinematics from the counterclockwise rotation of Laurentia that facilitated local extension in the passive margin.

Rose N. Cobbett https://orcid.org/0000-0001-9392-3258

INTRODUCTION

The breakup of the supercontinent Rodinia is partially recorded by syn- to post-rift, Neoproterozoic to mid-Paleozoic continental margin strata of the ancient Pacific or western Laurentian margin system from southern California, USA, to northern Yukon (e.g., Bond and Kominz, 1984; Li et al., 2008). The timing of the lithospheric breakup and establishment of the western Laurentian margin are generally constrained by: (1) the ages of mafic to felsic igneous rocks that are known or inferred to result from lithospheric extension (Colpron et al., 2002; Lund et al., 2003, 2010; Pigage et al., 2012, 2015; Yonkee et al., 2014; MacNaughton et al., 2016; Eyster et al., 2018; Campbell et al., 2019; Isakson et al., 2022); (2) tectonic subsidence trends of passive margin successions (e.g., Bond and Kominz, 1984); and (3) regional unconformities (e.g., Moynihan et al., 2019). These constraints indicate that the rift-to-drift transition or change from tectonic to thermal subsidence along western Laurentia was diachronous, with proposed breakup ages of ca. 570–530 Ma in the U.S. and southern Canadian Cordillera and ca. 500 Ma in the northern Canadian Cordillera (e.g., Colpron et al., 2002; Keller et al., 2012; Yonkee et al., 2014; Moynihan et al., 2019; Macdonald et al., 2023).

Mafic to felsic volcanic and plutonic rocks are recognized in post-rift, Upper Cambrian and Ordovician successions along the length of the Cordilleran orogen (e.g., Larson et al., 1985; Evans and Zartman, 1988; Lund et al., 2010; Campbell et al., 2019), but their relation to western Laurentian rift evolution remains uncertain. Most of the volcanic rock occurrences remain poorly characterized in terms of their eruptive age, crust-mantle sources, whole-rock geochemical compositions, depositional environments, and tectonic significance. Igneous rocks generated in modern, non-plume–related rifts, such as the Newfoundland-Iberia system, provide essential information for deciphering the temporal and structural evolution of continental margins (e.g., Whitmarsh et al., 2001; Manatschal, 2004; Jagoutz et al., 2007; Tucholke et al., 2007; Keen et al., 2014) because tectonism and magmatism are linked during rifting. For example, decompression melting can be a result of lithospheric extension, and the ability to precisely date igneous rocks associated with lithospheric thinning provides temporal constraints on this process (e.g., Jagoutz et al., 2007).

The location of igneous rocks can also highlight structural corridors or areas of structural complexity because crustal breaks can facilitate the migration of magma to the surface. Several volcanic provinces with seamounts have been identified in offshore Newfoundland and are interpreted to be coincident with transform faults or fracture zones (e.g., Pe-Piper et al., 1994; Keen et al., 2014). The mantle and crustal architecture of the margin that remains after rifting provides a primary constraint on how the passive margin develops, specifically where and how faults form and the nature and location of post-rift magmatism.

The Menzie Creek Formation is a belt of mafic volcanic rocks and associated gabbros exposed in central Yukon, northeast of the Tintina fault (Fig. 1). The unit was formalized by Gordey (2013) using a type section that mostly includes 400 m of basalt, basalt breccia, and volcanic tuff. The depositional age of the Menzie Creek Formation is constrained by fossil-bearing, Ordovician–Silurian carbonate rocks and shale units that are sparsely interbedded with volcanic rocks (Pigage, 2004; Gordey, 2013). For example, calcareous sandstone interbedded with the volcanic rocks and a limestone lens within basaltic lava yield Tremadocian and unconstrained Early Ordovician conodonts, respectively. Shale interbedded with and overlying the volcanic rocks have Floian to lower Darriwilian (late Early to late Middle Ordovician) to Llandovery (Early Silurian) graptolites, respectively. Darriwilian to Katian (late Middle to Late Ordovician) brachiopod fauna occur in shale units that overlie the volcanic rocks.

The Menzie Creek Formation occurs gradationally above calcareous phyllite and well-bedded limestone of the Cambrian to Ordovician Vangorda formation, which is regionally equivalent to the Rabbitkettle Formation, and interfingers with dark shale of the Ordovician to Silurian Road River Group (Fig. 2; Gordey, 2013; Gordey and Anderson, 1993). The Menzie Creek Formation is regionally coeval with the upper parts of the Crow Formation, which partly comprise mafic volcanic horizons that crop out in the southeast part of the Yukon (Figs. 1 and 2). The Cambrian to Ordovician Kechika group of the Cassiar terrane is also correlative with the Rabbitkettle and Menzie Creek formations and contains Late Cambrian to Early Ordovician igneous rocks (Figs. 1 and 2; Campbell et al., 2019) The Menzie Creek, Rabbitkettle, and Crow formations and the Road River Group rocks were deposited in an offshelf environment termed the Selwyn basin, a marine depocenter that persisted from the late Proterozoic to Early Devonian (Fig. 1).

In this article, we present the results of new bedrock mapping, whole-rock geochemical and Nd-Hf isotope data, and high-precision zircon U-Pb dating of the Menzie Creek Formation basaltic rocks. A geological map, three schematic stratigraphic sections, and a block diagram show the distribution, volume, and facies distribution of these rocks. In addition, we report the results of U-Pb zircon dating for a sample of the Crow Formation and evaluate correlations with other Lower Ordovician volcanic units in southern Yukon. The primary objectives of this study are to characterize the depositional environments, eruptive ages, and geochemical compositions of the Menzie Creek Formation rocks and evaluate published depth-dependent extension scenarios to gain an understanding of the architecture of the mantle and crust during rifting along western Laurentia. We also aim to evaluate potential mechanisms for post-rift magmatism that occurs after lithospheric rupture but is still influenced by the rift architecture that has been imposed on the continental margin.

RIFT MODELS FOR WESTERN LAURENTIA

Proposed rift models for the western Laurentian margin include: (1) homogenous pure-shear extension that resulted in uniform thinning and symmetric conjugate margins (e.g., Bond et al., 1985); (2) depth-dependent, simple-shear extension with lithospheric detachments that resulted in asymmetric conjugate rift margins (e.g., Lister et al., 1986); and (3) depth-dependent extension that resulted in coupled to decoupled thinning, crustal necking, and perhaps mantle exhumation (e.g., Yonkee et al., 2014). Hansen et al. (1993), Cecile et al. (1997), and Lund (2008) generally followed the simple-shear models of Lister et al. (1986) and divided the western Laurentian margin into several upper- and lower-plate segments based on the locations of crustal-scale lineaments or transfer zones and regional stratigraphic and structural relationships. The Yukon region is interpreted to occupy a lower-plate segment in these divisions that requires the upper crust to be extensively thinned by listric normal faults. Simple-shear rift models predict that rift-related magmatism is more likely to occur in upper-plate segments where the thinning of lithospheric mantle is most extensive (Wernicke, 1985). These two features are inconsistent with geological relationships in the Yukon Cordillera because: (1) there is little evidence for extensive structural disruption within pre- and syn-rift stratigraphic successions, as the model predicts (see fig. 2 in Lister et al., 1986); and (2) igneous rocks within the lower-plate segment are generally of greater frequency and volume than those of the neighboring upper-plate segments (e.g., Goodfellow et al., 1995; MacIntyre, 1998). This discrepancy between geologic features in the northern Cordillera and those predicted by simple-shear models requires new models or the refinement of existing models of western Laurentian rift processes and the post-rift crust and mantle architecture that remained after breakup. Early Paleozoic magmatism has generally been attributed to episodic, post-rift extension along the length of the western Laurentian margin (e.g., Turner et al., 1989; Poole et al., 1992; Goodfellow et al., 1995). Although post-rift magmatism has been documented in modern non-plume-related rifted margins, the mechanisms responsible for magma generation are not well understood (e.g., Jagoutz et al., 2007; Peron-Pinvidic et al., 2010). In addition, periodic extension after breakup remains problematic because extension should concentrate along a mid-oceanic ridge, where hot, thin, and ruptured lithosphere can extend under relatively low stress compared to adjacent areas of the rift margin that are intact (e.g., Fletcher and Munguia, 2000). Thomas (2014) reconciled this problem for the Iapetan rifted margin of eastern Laurentia by proposing that ductile flow in the mantle can transmit extensional stresses to the crust inboard of the rift even after breakup has occurred. This provides a mechanism for the generation of intracratonic grabens along the Iapetan margin that have post-rift fill and igneous rocks (e.g., Rome and Rough Creek basins, east-central USA). Peron-Pinvidic et al. (2010) discusses the possibility

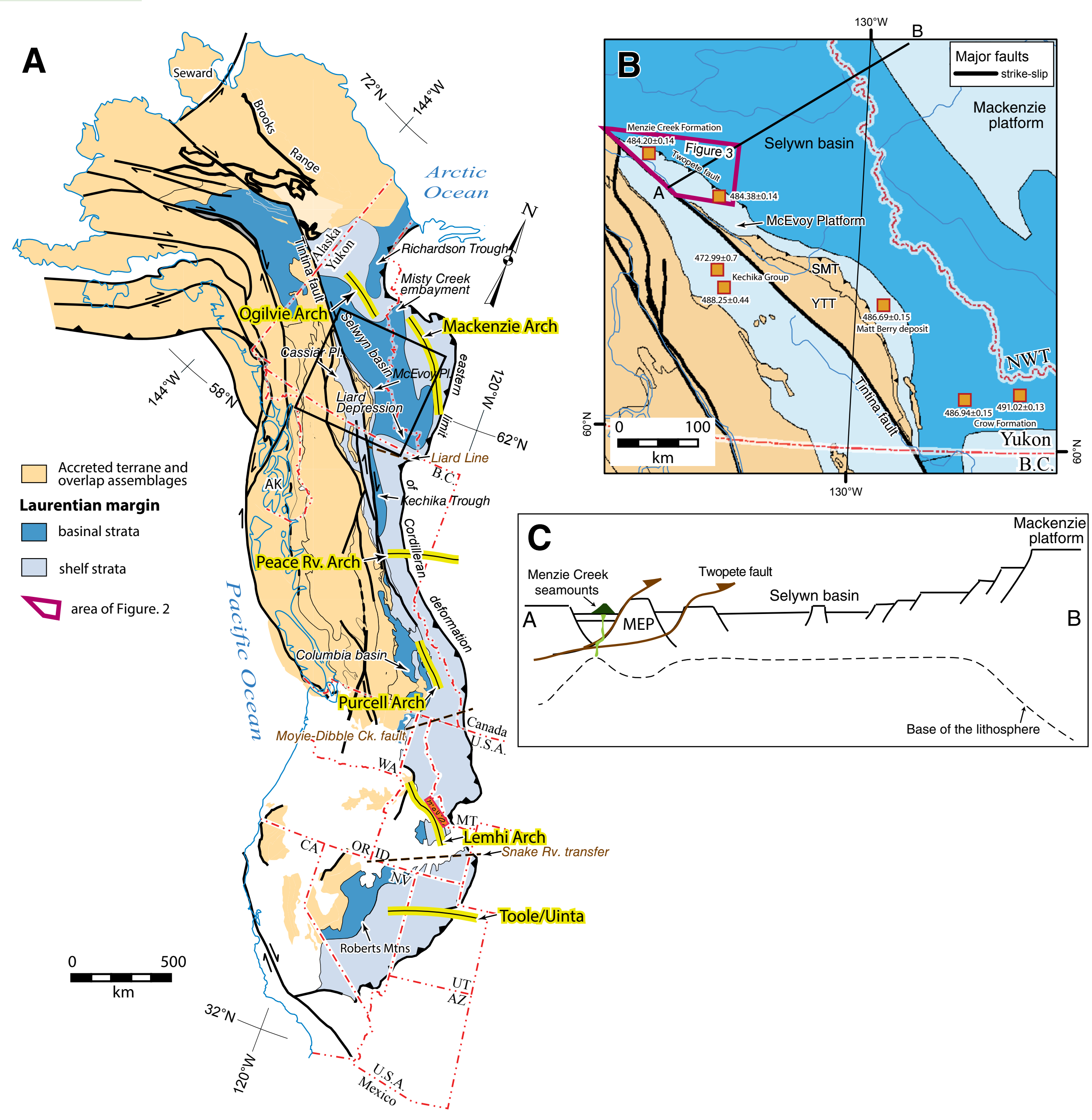

Figure 1. (A) Simplified terrane map showing the extent of the North American Cordillera. Ancestral North American rocks are shown in shades of blue, and accreted terranes are beige. WA—Washington, ID—Idaho, MT—Montana, OR—Oregon, UT—Utah, AZ—Arizona, CA—California, NV—Nevada, AK—Alaska. (B) Terrane map inset showing central and southeast Yukon. Orange squares are locations of Early Ordovician igneous rocks. Study area is outlined in a thick red line in central Yukon. YTT—Yukon Tanana terrane, SMT—Slide Mountain terrane; B.C.—British Columbia. (C) Schematic cross section from the Tintina fault (left) to the Mackenzie platform (right) showing one possibility for the crustal and mantle structure in the Early Ordovician. Brown lines delineate the future trace of the Twopete fault. Dashed line below the section shows the relative thickness of the lithosphere across the margin. Cross section is drawn using vertical exaggeration to show important features. MEP—McEvoy platform block, which is labeled on the geology map in Figure 3. Rv.—River.

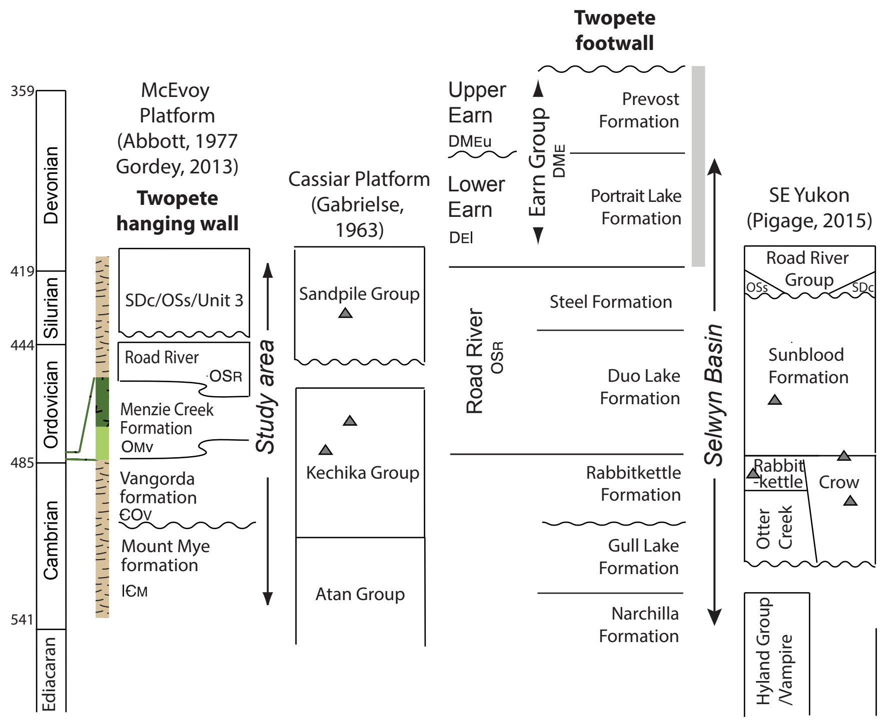

Figure 2. Regional stratigraphy of the Selwyn basin in central Yukon, Cassiar platform, and McEvoy platform. The Mount Mye and Vangorda formations correlate with the Gull Lake and Rabbitkettle formations of Selwyn basin, respectively. The Menzie Creek Formation occurs between the Vangorda formation and the Road River Group in the hanging wall of the Twopete fault. Grey triangles indicate the approximate level of mafic volcanic rocks that occur in southeast Yukon and the Cassiar platform. SDc—Silurian to Devonian carbonate of Gordey (2013); OSs—Ordovician and/or Silurian sandstone of Pigage et al. (2015); Unit 3—siltstone, silty dolostone and limestone, dolostone, quartz arenite, and dolomitic sandstone of Abbott (1997).

of off-axis magmatism persisting for tens of millions of years after breakup caused by thermal and/or compositional perturbations (i.e., convection cells) in the mantle and variations in lithospheric thickness that arise from rifting.

Some Mesozoic and younger continental margins have been studied by geophysical surveys, oceanic drilling, and oceanic floor bathymetry, which allows an in-depth understanding of continental extension through time (e.g., Tucholke et al., 2007; Peron-Pinvidic et al., 2013; Soares et al., 2012; Alves and Cunha, 2018; Zhao et al., 2021). For example, the Newfoundland (SE Grand Banks)-Iberia rift system is divided into several structural domains that run parallel to the rift axis and formed sequentially as extension migrated out toward the area of eventual breakup (Peron-Pinvidic et al., 2013). Proximal domains correspond to regions of thick crust (>30 km) with major basin-forming faults that sole out at mid-crustal levels and contain wedge-shaped, syn-rift basins. The necking and distal domains occur further outboard, near the edge or off the continental shelf, and are characterized by the transition to highly thinned or hyperextended crust (<10 km) and zones of exhumed continental mantle (e.g., Peron-Pinvidic et al., 2013). Beranek (2017) and Campbell et al. (2019) proposed that the inboard, easternmost platformal successions of the western Laurentian margin represent proximal domain deposits, whereas the outboard, westernmost basinal successions formed offshelf in the necking and distal domains. Based on the interpretations of Beranek (2017) and Campbell et al. (2019), and the stratigraphic models of Moynihan et al. (2019), the Ordovician Menzie Creek Formation is interpreted to have formed within the proximal or necking domain after breakup.

REGIONAL GEOLOGY

The northern Cordilleran orogenic belt parallels the western edge of North America and preserves, along its eastern part, lower to mid-Paleozoic platformal and basinal continental margin successions (Fig. 1; Bond et al., 1985; Cecile et al., 1997). Despite the effects of Mesozoic deformation that obscure the original size and geometry of paleogeographic features (e.g., Gordey and Anderson, 1993), much of the lower Paleozoic stratigraphy of the Cordilleran margin in Yukon is intact within major thrust panels (e.g., Roots, 2003; Cobbett, 2019). The Selwyn basin is one of the larger Paleozoic basins along the Cordilleran margin and is connected to smaller V-shaped depocenters, including the Kechika trough and Misty Creek embayment (Fig. 1; Cecile, 1982; MacIntyre, 1998; Ferri et al., 1999). The Selwyn basin contains fine-grained, post-rift marine deposits and volcanic rocks from the Cambrian Vampire, Gull Lake, and Rabbitkettle formations and the Ordovician to Silurian Road River Group (Fig. 2; Gordey and Anderson, 1993). In southeast Yukon, the Crow Formation is coeval with these marine formations but represents deposition in a deltaic environment (Pigage et al., 2015). The Selwyn basin is bounded to the southwest by the McEvoy platform, to the northeast by the Mackenzie platform, and to the north by the Ogilvie platform (Fig. 1). The Cassiar platform is situated outboard of the Kechika trough after restoration of the Tintina fault, a northwest-trending, strike-slip fault that accommodated >430 km of post-Cretaceous dextral displacement (Fig. 1; Gabrielse et al., 2006). Mafic volcanic and intrusive rocks occur within several Cambrian to Ordovician successions of the Selwyn basin and coeval strata of the surrounding carbonate platforms, Kechika trough, and Misty Creek embayment (Green, 1972; Gabrielse et al., 1973; Cecile, 1982; Roots, 1988; Goodfellow et al., 1995; Abbott, 1997; Pyle and Barnes, 2003; Pigage, 2004; Gordey, 2013; Campbell et al., 2019). These igneous rocks are both mapped as separate formations and as members within the sedimentary successions listed above (e.g., Old Cabin Formation, volcanic member of the Vampire Formation).

The Menzie Creek area is located in the northern part of the Selwyn basin, where pelitic and calc-silicate schist are regionally correlated with the Gull Lake and Rabbitkettle formations (Figs. 2 and 3). This metamorphosed stratigraphy extends to the southeast, where metavolcanic rocks are intercalated with gray phyllite at the Matt Berry occurrence, an alkaline volcanogenic massive sulphide (VMS) occurrence (Fig. 1; Fonseca, 2001). In the Menzie Creek area, the Twopete fault parallels the regional structural trend and coincides with the Selwyn basin–McEvoy platformal boundary. Its hanging wall to the south locally comprises older metamorphosed strata and volcanic and intrusive rocks of the Menzie Creek Formation, and its footwall contains younger sedimentary rocks to the north (Figs. 2 and 3; Cobbett, 2016b, 2019). A splay of the Twopete fault in the northwestern part of the mapped area separates Menzie Creek Formation rocks from Ordovician to Silurian graptolitic shale and sandstone that contain shallow-water features such as cross-beds and ripples. This stratigraphy is not subdivided in Figure 3 but occurs in the thrust-bound panel between the Macmillan River and Earn Lake (labeled MEP). Regionally, the McEvoy platform is a feature that developed in the Silurian; however, shallow-water features mapped during this study suggest the platform may have locally developed in the Ordovician (Gordey, 2013). The Menzie Creek Formation and Road River Group are the basement to the future shallow-water deposits that comprise the McEvoy platform (Fig. 1C). Lower Ordovician volcanic and volcaniclastic strata and cogenetic sills of the Menzie Creek Formation crop out in a linear belt in the hanging wall of the Twopete fault. The volcanic rocks typically form prominent mountain peaks, whereas sills intercalated with sedimentary rocks comprise relatively flat topography with abundant soil and till cover and sparse rock outcrops. In most places, the Menzie Creek Formation is the structurally highest part of the stratigraphy observed. A gradational upper contact with the Road River Group is suggested by the interfingering of the Menzie Creek Formation with graptolitic shale and volcanic rock units that locally grade upwards into fine-grained volcaniclastic rocks interbedded with micrite (Pigage, 2004; Cobbett, 2016a). Cretaceous plutons intrude all stratigraphic units and crosscut the latest movement on the Twopete fault.

The Neoproterozoic to Cambrian Vampire Formation comprises phyllite with lesser siltstone and sandstone and rare volcanic horizons. These volcanic horizons were sampled with the goal of constraining the age of the Vampire Formation; however, the geochronological results presented below indicate that the volcanic rocks mapped within the Vampire Formation are probably part of the Crow Formation, a younger succession of rocks comprising quartz-rich sandstone and minor mafic volcanic rocks. The sparse outcrops and similarity in lithologies of the Vampire and Crow formations could result in the inaccurate assignment of one formation or the other in southeast Yukon. The age constraint published in this paper suggests the reassignment of parts of the Vampire Formation mapped in southeast Yukon to the Crow Formation.

Ordovician igneous rocks crop out along the length of the Canadian and U.S. Cordilleran passive margin system in local zones (Fig. 1), including gabbro of the Kechika group in the Cassiar terrane of southeast Yukon (Campbell et al., 2019), volcanic and pyroclastic rocks of the Crow and Sunblood formations in southeast Yukon to the north of the Liard line (Pigage et al., 2015), alkaline plutonic rocks (e.g., Beaverhead pluton) in central Idaho north of the Snake River transfer zone (Evans and Zartman, 1988; Lund et al., 2010), seamount complexes in central Nevada to the south of the Snake River transfer zone (Watkins and Browne, 1989), and mafic igneous rocks in southwest Colorado, USA (Larson et al., 1985).

METHODS

Field Mapping and Stratigraphic Studies

Regional (1:50,000) and detailed (1:25,000) bedrock mapping, combined with petrographic studies and lithofacies analysis, facilitated the construction of stratigraphic sections and 3-D block diagrams of the Menzie Creek Formation and surrounding rock units (Fig. 4). Stratigraphic sections were compiled from foot traverses and are reasonable representations of the geology with 1 km of the sections marked in Figure 3. Lithofacies analyses were based on map, outcrop, and petrographic observations (Table 1).

Zircon U-Pb Geochronology

Two volcaniclastic rock samples from the Menzie Creek Formation and one from the Crow Formation were analyzed using a combination of laser

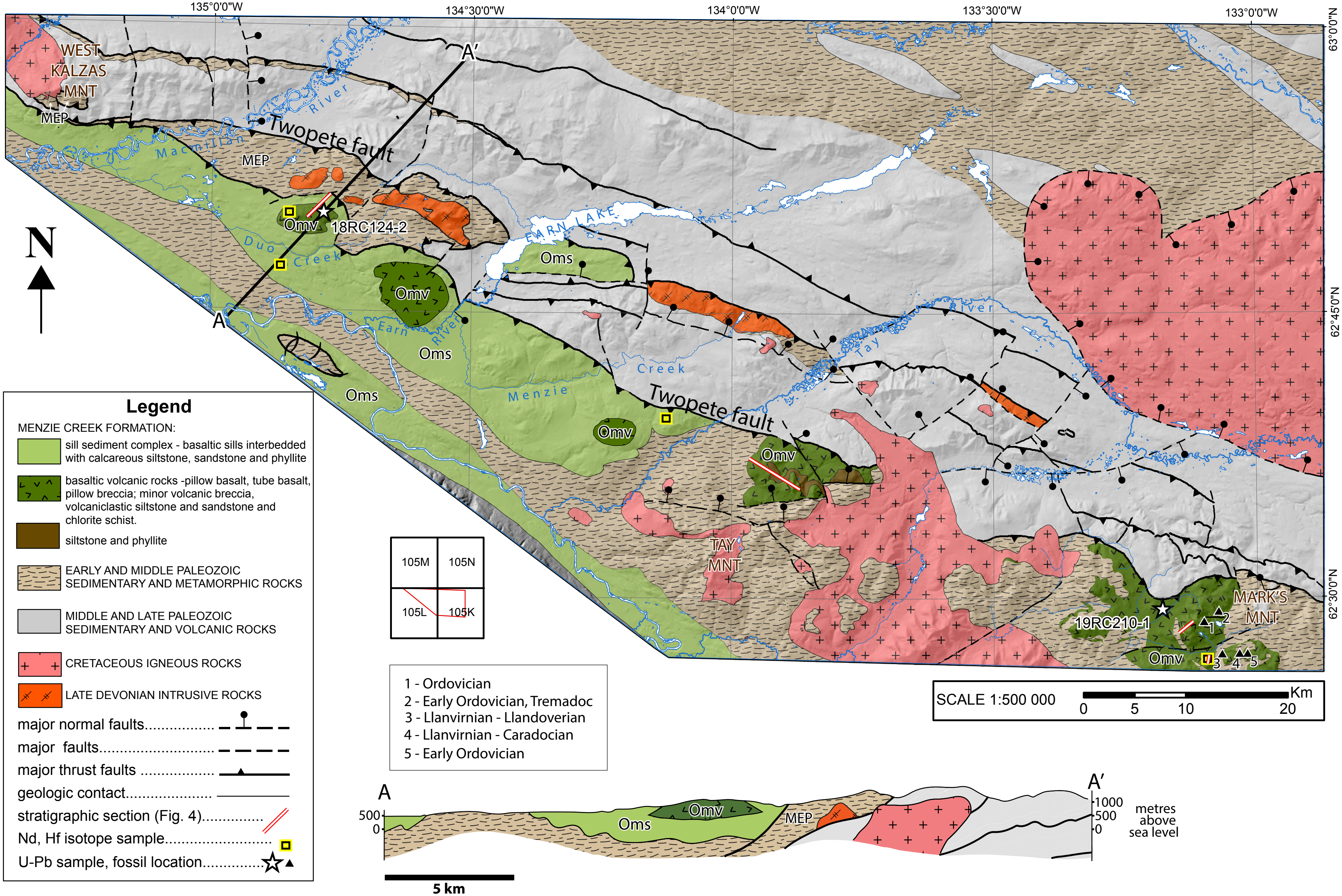

Figure 3. Simplified geological map of the Menzie Creek area, central Yukon. Stars indicate locations of zircon U-Pb samples, triangles are locations of fossil collections, red and white striped lines are locations of stratigraphic sections presented in Figure 4, and yellow squares are locations of whole-rock Hf and Nd isotope samples. MEP—McEvoy platform; these areas contain Ordovician to Silurian rocks with shallow-water features such as cross-beds and ripples. Oms—gabbro intruding fine-grained sedimentary rocks and phyllite; Omv—basaltic volcanic rocks and resedimented volcanogenic rocks; MNT—Mountain.

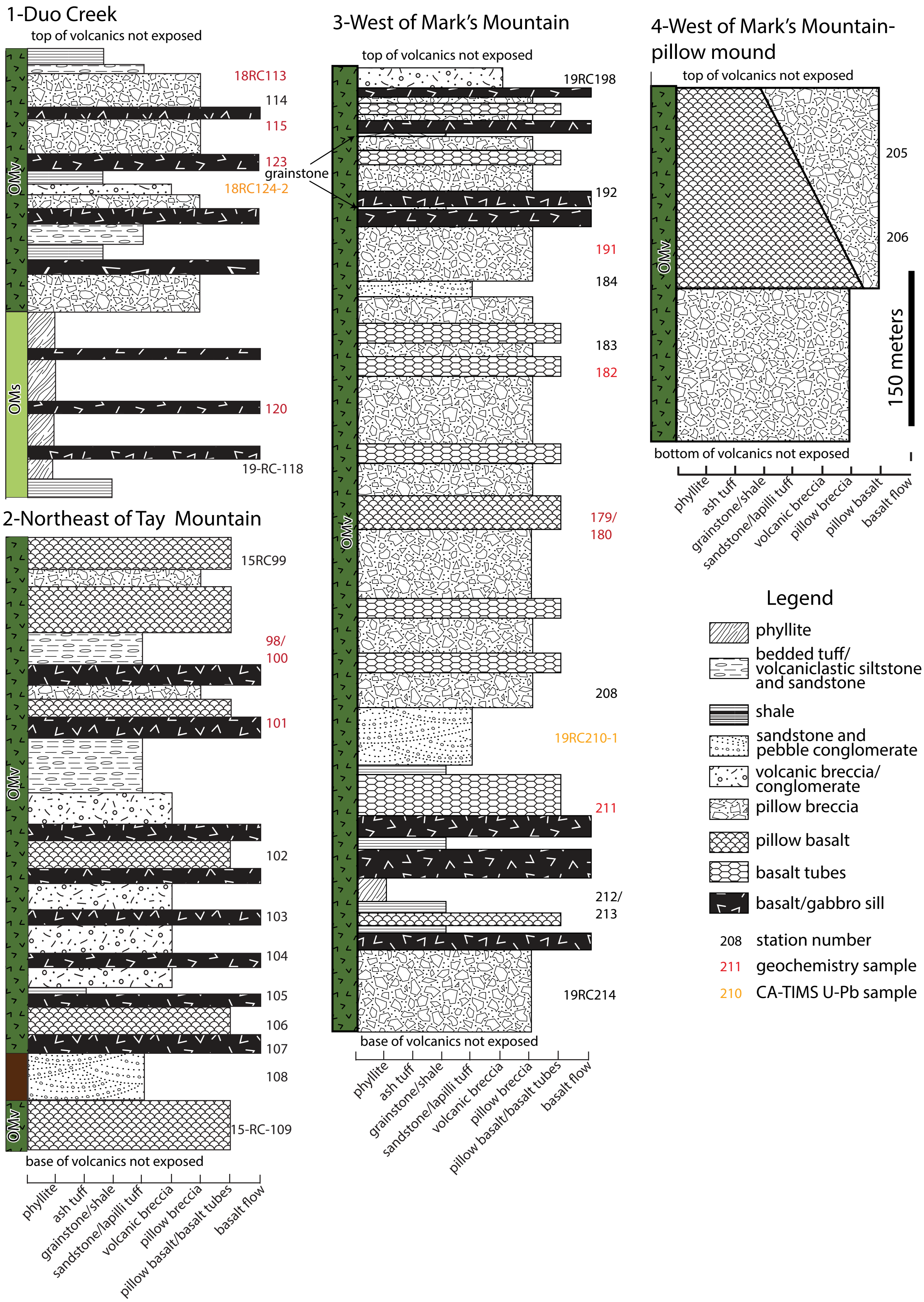

Figure 4. Schematic stratigraphy of (1) volcanic edifices and underlying sill sediment complex north of Duo Creek, (2) volcanic facies northeast of Tay Mountain, and (3) the volcanic edifices west of Mark's Mountain including (4) a section through the largest pillow mound in the study area. OMs—fine-grained sedimentary rocks and phyllite; OMv—resedimented volcanogenic rocks.

TABLE 1. LITHOFACIES OF MENZIE CREEK FORMATION

Lithofacies	**Rock name:** Spatial distribution	Map unit	Description	Field characteristics	Facies interpretation	Photos
Facies association 1: coherent	**Sparsely amygdaloidal dark green-grey pillow basalt:** exposed in all areas mapped as Omv except north of Duo Creek	Omv	Green, aphanitic basalt forming semi-spherical shapes that range in size from 15 cm to several meters. Semi-spherical shapes commonly conform to neighboring blocks or have triangular-shaped interstitial space filled with calcite. Outer 1–2 cm of the spheres comprise chlorite-altered basaltic material. Spheres can have radiating pipe vesicles or a single 5–8 cm vesicle in their centers.	Occurs in mounds of up to 200 m high or greater. Smaller pillows commonly have pipe-shaped amygdules radiating toward pillow margins filled with chlorite or calcite. Larger, meter-scale pillows commonly have large central amygdules. All pillows show an altered, fine-grained, glassy rind.	Interpreted to be pillow basalts formed where there is low magma effusive rate of lava into water. Effusive rate is greater than sedimentation rate.	Figs. 5C–5E (Mark's Mt.; Tay Mt.)
	Pyroxene ± plagioclase-phyric, fine-grained, dark grey-green basalt; rarely amygdaloidal basalt: exposed in areas mapped as Omv. Basalt forming tubes surrounded by breccia is common near Mark's Mountain	Omv	Dark grey-green, fine-grained basalt that has slightly larger crystals of pyroxene and plagioclase in a groundmass of similar composition. Rarely there are amygdules in the basalt. Locally, basalt forms bodies that have cross-sectional shapes characterized by flat bottoms with arcuate tops. These bodies are surrounded by basalt breccia comprising angular clasts of basalt that range in size from 1 cm to 5 cm in a chlorite-altered, fine-grained matrix.	Massive basalt on the scale of exposed outcrops; some outcrops show massive basalt with amygdules filled with calcite.	Massive and amygdaloidal basalt interpreted to be sheet flows that occur proximal (up to 1km) to vents. Basalt tubes are interpreted to be farther from vents than flows, and the surrounding basalt breccia is interpreted to be hyaloclastite breccia formed from shattering/quenching of basalt upon contact with cold sea water.	Figs. 5A, 5B (Earn River; Mark's Mt.)
	Pyroxene (±feldspar)-phyric moderately porphyritic fine- to coarse-grained gabbro with chilled margins: common everywhere except near Mark's Mountain	Oms	Orange weathering, green and grey fresh, fine- to coarse-grained pyroxene-bearing gabbro. Pyroxene crystals commonly are altered to chlorite and actinolite. Smaller grain size occurs within 30 cm of contact with sedimentary rocks and gradually becomes coarse-grained approximately 1 m from contact with sedimentary rocks. Rarely, gabbro is fine-grained with small, 2–3-mm-sized amygdules.	Ranges from sheet-like bodies that are 30 cm to tens of meters thick to large equidimensional bodies up to 250 × 500 m. Many have chilled margins, leading to the interpretation that these bodies are sills that intrude fine-grained sediments. Common in the northwestern part of the map, where gabbro is interlayered with thin-bedded, calcareous siltstone and sandstone, and locally increases in thickness into small, intrusion-like bodies. Indurated sedimentary rocks above and below the igneous body are interpreted to result from metamorphism of heat from intrusive bodies.	Locally may be flows or cryptoflows where basalt is erupting and flowing in large sheets or sills are locally breaching the surface. Many other occurrences are interpreted to be sills or make up sill-sediment complexes based on fine-grained top and bottom chilled margins with coarse-grained sill centers. Suggests magma effusive rate is less than sedimentation rate.	Figs. 5F, 5G (Duo Creek)
Facies association 2: autoclastic basalt breccia	**Matrix-supported, monolithic, grey-green, basalt breccia**: small percentage of exposed rocks near Duo Creek, Menzie Creek, and Mark's Mountain	Omv	Matrix-supported breccia to volcanic conglomerate, dominated by subrounded to angular clasts of basalt, amygdaloidal basalt, and lesser volcaniclastic and tuffaceous rocks. Matrix is fine-grained and basaltic in composition.	Commonly exposed in isolated outcrops along the fringes of the basaltic piles; this is a resistant, cliff-forming rock type.	Sub-rounded clasts suggest they were transported after fragmentation. Deposition on the flanks of mounded volcanic piles from local breakdown (spalling) of oversteepened sections. Commonly crudely bedded, which supports the idea that these are comprised of transported volcanic detritus. Alternatively, rounding of clasts occurred due to deposition while still hot and in this case may be proximal to distal.	Figs. 6D, 6E (D-Mark's Mt.; E-Menzie Creek)
	Clast-supported, monolithic, grey-green basalt breccia with very fine-grained interstitial matrix: common rock type in the southeastern part of the map area	Omv	The breccia comprises two clast types: (1) sub-angular 0.5–1-cm-sized clasts of very fine-grained, chlorite-altered basalt, and (2) angular 5–10 cm clasts of aphanitic basalt in a similar composition, very fine-grained, chlorite-altered matrix. Devitrified rims on clasts are common, and spherulites within matrix are locally observed.	Sections of basalt breccia that form massive thicknesses >10 m.	Interpreted to be formed from quench fragmentation as basaltic flows, tubes, and pillows encountered cold seawater. Note: in some areas the smaller, sub-angular clasts are interpreted to be pieces of altered pillow rinds and larger, more angular clasts of aphanitic basalt from pillow centers.	Figs. 6A, 6B (South of Mark's Mt.)
	Sparsely spherulitic, devitrified glassy, dark grey-green hyaloclastite breccia: abundant near Mark's Mountain	Omv	Matrix- and clast-supported, sometimes jigsaw-fit textures comprising 5–15-cm-sized angular clasts that commonly show devitrified alteration along clast margins. Matrix and interstitial material is glass.	Forms massive, resistance cliff-faces up to 25 m high.	Interpreted to be formed by quench fragmentation of lava tubes, flows, and pillows when they encounter cold seawater.	Fig. 6C (Mark's Mt.)
Facies association 3: resedimented volcanic rocks	**Volcaniclastic siltstone and sandstone/chlorite schist:** exposed locally everywhere that is mapped as Omv except near Mark's Mountain, where it is only found in one outcrop	Omv	Green, thin-bedded, volcanic-derived siltstone and sandstone with rare pebble trains, and rare conglomerate dominated by rounded mafic volcanic clasts. Green, fine-grained, chlorite-rich rock with a well-developed pervasive foliation.	Scattered, isolated outcrops exposed along the margins of the resistant, blocky piles of basaltic rocks.	Chlorite-rich, foliated rocks are interpreted to be a deformed equivalent to fine-grained volcaniclastic rocks. Bedded volcaniclastic rocks are interpreted to be formed by local erosion of volcanic piles and subsequent deposition of detritus near the bottom of seamount slopes.	Figs. 7A–7D (A, B: Mark's Mt.; C: Tay Mt.; D: Duo Creek)

Notes: Oms—gabbro sills intruding fine-grained sedimentary rocks and phyllite; Omv—basaltic volcanic rocks and resedimented volcanogenic rock; Mt.—Mountain.

ablation–inductively coupled plasma–mass spectrometry (LA-ICP-MS; Table S1 in the Supplemental Material[1]) and chemical abrasion–isotope dilution–thermal ionization mass spectrometry (CA-ID-TIMS; Table 2) methods at the Isotope Geology Laboratory, Boise State University, Idaho, USA (detailed methods are in the text of the Supplemental Material). Zircon grains were imaged by cathodoluminescence and analyzed by LA-ICP-MS to characterize the age populations (Fig. S1; see footnote 1). A subset of the zircon grains that comprised the youngest, statistically coherent population with similar chemical composition and morphology was subsequently analyzed by CA-ID-TIMS. Weighted mean $^{206}Pb/^{238}U$ dates were calculated from equivalent CA-ID-TIMS dates (probability of fit >0.05) using Isoplot 3.0 (Ludwig, 2003). Errors on weighted mean dates are given as ± x / y / z, where x is the internal error based on analytical uncertainties only, including counting statistics, subtraction of tracer solution, and blank and initial common Pb subtraction; y includes the tracer calibration uncertainty propagated in quadrature; and z includes the ^{238}U decay constant uncertainty propagated in quadrature. Internal errors should be considered when comparing our dates with $^{206}Pb/^{238}U$ dates from other laboratories that used the same tracer solution or a tracer solution that was cross-calibrated using EARTHTIME gravimetric standards. Errors, including the uncertainty in the tracer calibration, should be considered when comparing our dates with those derived from other geochronological methods using the U-Pb decay scheme (e.g., LA-ICP-MS). Errors are reported at 2σ and include uncertainties in the tracer calibration and ^{238}U decay constant (Jaffey et al., 1971) should be considered when comparing our dates with those derived from other decay schemes (e.g., $^{40}Ar/^{39}Ar$, ^{187}Re-^{187}Os).

Whole-Rock Lithogeochemistry

Fifty basalt and gabbro samples were analyzed for whole-rock geochemical analysis (Table 3) based on: (1) the volcanic rock type (breccia and volcaniclastic rocks were not sampled); and (2) the lowest degree of alteration and deformation. Samples collected from 2015 to 2018 were prepared and analyzed at Activation Laboratories in Ancaster, Ontario, Canada; results are presented in Table 3, and the full methodology is presented in the text of the Supplemental Material (footnote 1). Samples collected in 2019 were analyzed for major and trace elements at ALS Laboratories in North Vancouver, British Columbia, Canada (Table 3; methodology is presented in the text of the Supplemental Material). An interlaboratory comparison shows that major and trace element variation is ≤5% and ≤12%, respectively, except for some elements with concentrations near the detection limit (e.g., Pb; Fig. S2, see footnote 1). For all elements used in the interpretation of the Menzie Creek volcanic rocks, precision ranges from 1% to 5% of relative standard deviation and accuracy ranges from 0% to 13% of relative difference (Table S3; Jenner, 1996).

Whole-Rock Hf and Nd Isotope Geochemistry

Whole-rock Hf and Nd isotope ratios were determined at the Pacific Centre for Isotopic and Geochemical Research (PCIGR), University of British Columbia. The Nd and Hf isotope ratios of separate aliquots of sample powders prepared at Activation Laboratories and ALS for lithogeochemical analyses were measured by multi-collector (MC)-ICP-MS (Nu Instruments Ltd., Nu II 214 or Nu 1700) following the protocols of Weis et al. (2006, 2007). Samples were normalized to the JNDi (Nd) and JMC 475 (Hf) standards using sample-standard bracketing. Normalization values were $^{143}Nd/^{144}Nd = 0.512116$ for JNDi (Tanaka et al., 2000) and $^{176}Hf/^{177}Hf = 0.282160$ for JMC 475 (Blichert-Toft and Albarède, 1997). Initial or age-corrected epsilon values were calculated using new zircon U-Pb age results and present-day values of $^{176}Hf/^{177}Hf = 0.282785$, $^{143}Nd/^{144}Nd = 0.512630$, $^{176}Lu/^{177}Hf = 0.0336$, and $^{147}Sm/^{144}Nd = 0.1960$ for the chondritic uniform reservoir (CHUR; Bouvier et al., 2008). Detailed methods are included in the text of the Supplemental Material.

RESULTS

Principal Lithofacies of the Menzie Creek Formation

Menzie Creek Formation igneous rocks are broadly grouped into two mappable units. The first group includes basalt-dominated facies, volcanic breccia, and resedimented volcanogenic rocks (Omv). The second unit includes fine- to coarse-grained gabbro bodies that are interlayered with fine-grained sedimentary rocks and phyllite (Oms). The relationship between these two units is uncertain; however, north of Duo Creek the gabbro bodies structurally underlie the volcanic facies of unit Omv (Figs. 3 and 4, Duo Creek section). Pigage (2004) reported gabbro dikes and sills within calc-silicate schist below the Menzie Creek Formation to the east of the Anvil batholith, and these are interpreted to be correlative with Oms facies.

Basaltic volcanic rocks (Omv) are exposed at five discrete locations along a linear belt that parallels the Twopete fault (Fig. 3). Coherent basalt and volcanic breccia units grade upwards into reworked volcanogenic sedimentary breccia, sandstone, and siltstone north of Duo Creek (Fig. 4). Massive and amygdaloidal basalt with chlorite schist occurs near Earn River. The section is dominated by volcanic breccia south of Menzie Creek. Coherent basalt and basalt breccia are interlayered with fine-grained sedimentary rocks northeast of Tay Mountain (Fig. 4). Reworked volcanogenic strata are mapped several kilometers away from the thickest part of the basaltic rocks. Several mountains are almost entirely made up of basaltic rocks west of Mark's Mountain. An

[1]Supplemental Material. Detailed analytical methods for whole-rock trace-element and isotope geochemistry and U-Pb geochronology, including quality assurance and quality control calculations for geochemical data. Additional geochemistry diagrams, cathodoluminescence images of zircon crystals, and LA-ICP-MS data table are also included. Please visit https://doi.org/10.1130/GEOS.S.23412350 to access the supplemental material, and contact editing@geosociety.org with any questions.

TABLE 2. CHEMICAL ABRASION–THERMAL IONIZATION MASS SPECTROMETRY ZIRCON U-Pb ISOTOPIC DATA

Sample	LA-ICP-MS spot label	Th/U	^{206}Pb* × 10^{-13} mol	mol % ^{206}Pb*	Pb* (pg)	Pb_c (pg)	Pb*/Pb_c	Pb_c (pg)	^{206}Pb/^{204}Pb	Radiogenic isotope ratios								Isotopic dates						Include in weighted mean?	Weighted mean calculations	
										^{208}Pb/^{206}Pb	^{207}Pb/^{206}Pb	% err	^{207}Pb/^{235}U	% err	^{206}Pb/^{238}U	% err	Corr. coef.	^{207}Pb/^{206}Pb	±	^{207}P/^{235}U	±	^{206}Pb/^{238}U	±			
(a)		(b)	(c)	(c)	(c)	(c)	(c)	(c)	(d)	(e)	(e)	(f)	(e)	(f)	(e)	(f)		(g)	(f)	(g)	(f)	(g)	(f)			
18RC124-2 (62.83593, –134.78627) Menzie Creek Formation																										
z2	5,6	0.581	0.3988	99.14	10.19	0.29	36	0.29	2101	0.182	0.056865	0.217	0.611818	0.267	0.078033	0.078	0.733	486.28	4.79	484.71	1.03	484.37	0.36	x	^{206}Pb/^{238}U ± random (+tracer) [+decay constant]	MSWD = 0.5
z3	19	0.545	0.7031	99.43	17.81	0.33	54	0.33	3187	0.171	0.056970	0.144	0.612821	0.197	0.078016	0.074	0.803	490.39	3.18	485.34	0.76	484.27	0.35	x	**484.20 ± 0.14** (0.27) [0.57]	pof = 0.77
z4	11	0.407	0.7556	99.39	18.46	0.39	48	0.39	2943	0.128	0.056861	0.158	0.611607	0.214	0.078012	0.085	0.771	486.13	3.49	484.57	0.83	484.24	0.40	x		n = 7
z7	21	0.699	1.1544	99.73	30.39	0.26	117	0.26	6668	0.219	0.056861	0.120	0.611584	0.176	0.078009	0.083	0.803	486.13	2.65	484.56	0.68	484.23	0.38	x		
z1	12,13	0.613	0.7311	99.56	18.84	0.27	71	0.27	4116	0.192	0.056874	0.121	0.611704	0.175	0.078006	0.071	0.851	486.65	2.66	484.63	0.68	484.21	0.33	x		
z5	22,23	0.477	0.4135	98.56	10.29	0.50	20	0.50	1252	0.149	0.056916	0.314	0.612059	0.363	0.077993	0.082	0.666	488.29	6.93	484.86	1.40	484.13	0.38	x		
z6	20	0.732	0.7971	99.35	21.16	0.43	49	0.43	2777	0.229	0.056855	0.153	0.611175	0.205	0.077964	0.072	0.801	485.91	3.39	484.30	0.79	483.96	0.33	x		
19RC210-1 (62.47071, –133.14167) Menzie Creek Formation																										
z4	209,210	0.502	3.2681	99.95	81.85	0.15	559	0.15	33461	0.157	0.056910	0.064	0.612402	0.129	0.078081	0.069	0.971	487.05	1.41	485.07	0.50	484.66	0.32	x	^{206}Pb/^{238}U ± random (+tracer) [+decay constant]	MSWD = 0.9
z5		0.757	1.0799	99.81	28.84	0.17	166	0.17	9322	0.237	0.056899	0.088	0.611942	0.149	0.078036	0.070	0.921	486.64	1.95	484.78	0.57	484.39	0.33	x	**484.38 ± 0.14** (0.27) [0.57]	pof = 0.46
z1	212,213	0.482	3.4811	99.95	86.73	0.13	663	0.13	39895	0.151	0.056897	0.066	0.611906	0.130	0.078036	0.070	0.960	486.54	1.45	484.76	0.50	484.39	0.33	x		n = 6
z2	214,215	0.654	0.8880	99.83	23.12	0.12	188	0.12	10831	0.205	0.056997	0.108	0.612910	0.166	0.078026	0.078	0.842	490.43	2.39	485.39	0.64	484.33	0.36	x		
z6		0.749	1.7001	99.91	45.31	0.12	371	0.12	20847	0.234	0.056940	0.068	0.612243	0.134	0.078020	0.070	0.973	488.20	1.50	484.97	0.52	484.29	0.33	x		
z3	211	0.829	1.3270	99.90	36.06	0.11	325	0.11	17910	0.260	0.056909	0.076	0.611776	0.140	0.078002	0.072	0.943	487.01	1.68	484.68	0.54	484.19	0.34	x		
20RC234-1 (60.51329, –127.283) Crow Formation																										
z3	919	0.594	1.0480	99.70	26.87	0.26	103	0.26	6056	0.186	0.056905	0.105	0.615688	0.162	0.078506	0.072	0.875	486.86	2.31	487.14	0.63	487.20	0.34	x	^{206}Pb/^{238}U ± random (+tracer) [+decay constant]	MSWD = 1.0
z2	921	0.719	1.4262	99.86	37.73	0.16	231	0.16	13077	0.225	0.056934	0.074	0.615756	0.139	0.078475	0.070	0.963	487.99	1.63	487.18	0.54	487.01	0.33	x	**486.94 ± 0.15** (0.21) [0.55]	pof = 0.39
z1	930	0.850	0.7040	99.72	19.23	0.17	116	0.17	6394	0.266	0.056949	0.135	0.615769	0.186	0.078456	0.072	0.813	488.58	2.97	487.19	0.72	486.90	0.34	x		n = 5
z5	923	0.775	0.9804	99.35	26.30	0.53	49	0.53	2775	0.243	0.056943	0.148	0.615600	0.198	0.078442	0.071	0.802	488.35	3.25	487.09	0.77	486.82	0.33	x		
z4	918	0.591	1.7971	99.88	46.05	0.18	258	0.18	15115	0.185	0.056885	0.073	0.614926	0.136	0.078437	0.069	0.956	486.07	1.61	486.66	0.53	486.79	0.32	x		

Notes: LA-ICP-MS—laser ablation–inductively coupled plasma–mass spectrometry; pof—probability of fit; MSWD—mean square of weighted deviates; n—number.
(a) z1, z2, etc. are labels for analyses composed of single zircon grains that were annealed and chemically abraded (Mattinson, 2005).
(b) Model Th/U ratio was calculated from radiogenic ^{208}Pb/^{206}Pb ratio and ^{207}Pb/^{235}U date.
(c) Pb* and Pbc are radiogenic and common Pb, respectively. mol % ^{206}Pb* is with respect to radiogenic and blank Pb.
(d) Measured ratio was corrected for spike and fractionation only. Pb fractionation correction of 0.16 ± 0.03 (1 sigma) %/amu (atomic mass unit) was applied to samples 18RC124-2 and 20RC234-1, based on recent analyses of EARTHTIME ^{202}Pb-^{205}Pb ET2535 tracer solution. Pb fractionation correction of 0.20 ± 0.03 (1 sigma) %/amu (atomic mass unit) was applied to sample 19RC210-1.
(e) Corrected for fractionation and spike. Common Pb in zircon analyses was assigned to procedural blank with composition of ^{206}Pb/^{204}Pb = 18.04 ± 0.61%; ^{207}Pb/^{204}Pb = 15.54 ± 0.52%; ^{208}Pb/^{204}Pb = 37.69 ± 0.63% (1 sigma). ^{206}Pb/^{238}U and ^{207}Pb/^{206}Pb ratios were corrected for initial disequilibrium in ^{230}Th/^{238}U using a D(Th/U) of 0.20 ± 0.05 (1 sigma).
(f) Errors are 2 sigma, propagated using algorithms of Schmitz and Schoene (2007) and Crowley et al. (2007).
(g) Calculations were based on the decay constants of Jaffey et al. (1971). ^{206}Pb/^{238}U and ^{207}Pb/^{206}Pb dates were corrected for initial disequilibrium in ^{230}Th/^{238}U using a D(Th/U) of 0.20 ± 0.05 (1 sigma).

TABLE 3. MAJOR AND TRACE ELEMENT GEOCHEMICAL COMPOSITION OF MENZIE CREEK FORMATION ROCKS

Sample	13RC205-1	13RC218-1	15RC080-1	15RC100-1	15RC101-1	15RC114-1	15RC263-1	15RC264-1	15RC282-1	15RC285-1-2	16RC153-1	16RC161-1	16EW012-1	18RC199-1	18RC201-1	18RC206-1	18RC210-3-1	18RC212-1-1	18RC215-2-1	18RC222-1-1	18RC225-1	18RC237-1	18RC036-1	18RC112-2-1	18RC113-2-2
Rock type	gabbro	gabbro	basalt	basalt	basalt	p. basalt	basalt	p. basalt	basalt	basalt	basalt	a. basalt	basalt	basalt	basalt	basalt	basalt	basalt	basalt	basalt	p. basalt	a. basalt	basalt	a. basalt	crystal tuff
Lat	62.609702	62.610903	62.577125	62.597175	62.595317	62.582022	62.638427	62.631167	62.656722	62.651755	62.78131	62.799816	62.770787	62.914831	62.913457	62.929945	62.787499	62.785381	62.782869	62.792384	62.803297	62.789544	62.786311	62.835695	62.833015
Long	−133.76618	−133.73283	−133.8779	−133.88255	−133.89997	−133.8643	−134.25972	−134.24069	−134.12617	−134.11227	−134.6119	−134.3244	−134.62548	−135.36706	−135.38462	−135.41118	−134.85449	−134.83997	−134.79624	−134.85017	−134.85603	−134.87124	−134.71853	−134.82676	−134.83721
%																									
SiO_2	47.61	48.45	48.51	43.99	43.41	46.08	47.68	47.78	50.99	51.39	44.44	47.1	52.14	49.72	48.24	49.2	48.96	48.95	47.15	49.03	50.22	46.89	47.88	44.16	49.78
Al_2O_3	13.46	13.35	14.91	13.85	14.41	14.86	13.65	15.07	13.18	11.58	16.18	15.41	15.71	14.39	13.63	14.57	14.8	15	14.23	12.75	13.48	11.94	12.96	14.69	13.91
$Fe_2O_3(T)$	11.73	10.22	12.19	12.75	12.8	14.48	11.59	11.75	11.99	15.24	14.01	10.7	14.09	14.18	15.6	13.86	10.08	11.7	15.05	11.35	13.46	11.35	12.7	11.4	11.1
MnO	0.16	0.15	0.17	0.15	0.13	0.17	0.16	0.16	0.17	0.28	0.15	0.15	0.05	0.12	0.20	0.16	0.15	0.18	0.21	0.12	0.20	0.16	0.19	0.16	0.13
MgO	8.92	10.82	5.46	5.03	5.92	6.1	6.89	5.53	4.89	3.85	6.45	5.93	4.74	6.06	5.05	7.15	7.86	5.68	5.18	9.49	5.27	12.64	9.33	6.32	5.12
CaO	9.18	8.86	11.9	9.32	6.76	11.46	7.11	8.2	9.23	5.72	3.9	10.92	1.37	2.99	6.13	2.3	6.4	5.37	6.73	5.05	6.88	8.53	7.32	7.03	5.1
Na_2O	2.91	3.24	3.36	2.6	3.77	2.67	4.57	3.19	2.68	3.58	3.84	2.79	4.28	3.41	4.26	4.34	4.58	4.98	3.4	2.25	4.91	2.82	3.41	3.07	4.74
K_2O	0.65	0.7	0.33	0.71	0.37	0.35	0.08	1.3	1.25	0.99	0.6	0.37	0.13	1.01	0.26	0.94	0.05	0.11	1.35	0.01	0.24	0.02	1.06	1.46	0.16
TiO_2	2.24	1.84	2.74	2.24	3.02	2.56	2.53	2.63	2.44	3.05	2.34	1.94	3.00	2.86	3.17	2.69	2.00	2.50	3.12	2.03	3.16	1.82	2.19	2.02	2.96
P_2O_5	0.28	0.23	0.34	0.27	0.41	0.29	0.27	0.21	0.24	0.71	1.05	0.37	0.4	0.41	0.32	0.39	0.26	0.37	0.42	0.23	0.42	0.22	0.24	0.55	0.36
LOI	3	1.22	0.63	9.47	7.73	0.6	4.47	2.89	1.64	3.82	7.69	4.57	4.34	4.26	3.82	4.62	4.99	5.54	2.96	7.6	1.98	3.79	3.39	9.16	7.17
ppm																									
Sc	33	33	33	27	32	32	35	33	28	23	14	33	34	33	34	31	36	26	33	34	34	33	37	34	32
Be	1	1	2	1	2	1	2	2	2	3	3	1	1	2	<1	2	<1	2	1	2	<1	1	<1	<1	<1
V	295	237	338	273	331	304	326	414	338	140	133	261	302	406	459	329	269	291	361	263	368	234	287	269	297
Cr	490	590	170	80	80	150	190	<20	70	<20	30	210	130	50	30	60	420	30	60	600	130	830	190	110	150
Co	48	46	33	33	47	35	38	34	33	24	33	43	43	49	45	39	40	36	42	51	38	62	52	39	37
Ni	250	300	50	60	50	80	90	<20	40	<20	<20	100	70	60	50	30	140	40	50	210	70	310	120	50	60
Cu	50	100	10	140	140	<10	170	30	40	20	<10	60	70	390	160	30	100	90	210	110	170	80	110	130	80
Zn	90	90	90	80	100	80	110	70	90	150	110	90	110	60	120	130	80	100	140	80	110	100	110	80	80
Ga	19	16	19	18	19	21	19	19	19	22	19	19	22	21	19	22	17	20	24	17	17	15	18	17	20
Ge	1.7	1.9	0.6	0.7	1	0.8	1	1.2	1.1	1.1	2.2	1.8	2.4	1.5	1.9	1.3	1.5	1.6	1.3	1.9	1.1	1.5	2	1.4	1.3
As	24	<5	<5	<5	<5	<5	<5	<5	9	<5	<5	10	<5	10	<5	8	<5	6	<5	<5	<5	<5	<5	<5	5
Rb	15	24	2	11	7	6	<1	33	25	21	16	9	3	13	6	31	1	4	37	<1	5	<1	12	29	3
Sr	294	312	299	224	168	245	219	500	571	146	328	355	91	169	429	265	621	670	358	382	429	214	131	641	118
Y	20.7	17.8	25.1	24.1	28.7	23.3	24.2	24.1	28	52.3	34.8	27.7	31.5	32	27.1	30.2	20.2	26	35	19.8	33.2	18.4	21.1	20.4	28.4
Zr	158	122	200	159	235	174	194	169	192	384	347	181	230	200	157	210	129	186	219	147	234	124	129	147	218
Nb	27.3	21.9	29.9	21.1	34.6	23.3	29.1	30.8	24.1	59	121	32.5	37.2	27.7	27.7	31.4	26.5	35.5	35.9	20.8	36	23.5	21.9	51.7	37.5
Mo	<2	<2	<2	<2	<2	<2	<2	<2	<2	4	2	<2	<2	5	<2	<2	<2	<2	<2	<2	<2	<2	<2	<2	<2
Ag	1.5	1.1	0.6	<0.5	0.6	<0.5	<0.5	<0.5	0.5	1.1	<0.5	<0.5	<0.5	0.5	<0.5	0.5	<0.5	<0.5	0.5	<0.5	0.6	<0.5	<0.5	0.5	0.7
In	<0.1	<0.1	<0.1	<0.1	<0.1	<0.1	<0.1	<0.1	<0.1	0.1	0.1	<0.1	<0.1	0.1	0.1	0.1	0.1	0.1	0.1	0.1	0.1	0.1	0.1	0.1	0.1
Sn	<1	<1	1	<1	1	1	1	<1	1	2	2	1	2	3	1	2	1	1	2	1	2	1	1	1	2
Sb	6.4	0.5	7.4	<0.2	0.9	9.1	<0.2	<0.2	1.5	1.2	0.6	1.1	<0.2	0.2	1.3	3.2	0.7	0.6	3.7	0.9	<0.2	0.3	<0.2	<0.2	2.1
Cs	1.3	2.9	0.3	0.3	0.2	0.7	0.3	0.5	0.5	12.6	1.8	1.2	0.2	2.2	9.3	15.8	0.3	1.6	2.4	0.1	2.8	0.2	2	2	0.7
Ba	483	607	135	348	127	353	403	952	1364	425	838	667	244	6234	974	4325	199	258	1307	51	569	61	1627	6580	509
La	19.4	16.8	23.2	17.4	25.2	21.8	25	28.5	25.1	53.1	116	30.4	33.5	31.3	22.5	27.7	27.5	39.6	32.6	22.2	31.7	25	16.2	43.3	27.8
Ce	42.2	36.1	54	39.4	58.5	46.9	54.2	58.7	53.1	113	213	59.4	66.9	65.5	48.6	61.8	54.8	78.3	69	47.4	68.1	49.9	34.8	83.7	57.7
Pr	5.59	4.75	6.73	4.87	7.34	5.45	6.51	6.82	6.22	13.4	21.3	6.82	8.15	7.86	5.93	7.71	6.47	8.92	8.37	5.71	8.38	5.87	4.55	9.54	7.23
Nd	23.8	20.1	29.7	21.7	32.2	23.7	28	27.8	25.8	56.3	75.1	26.7	33.7	34	25.6	32.8	26.1	36.3	36.2	23.9	34.5	23	19.8	37.5	30.7
Sm	5.24	4.61	6.51	5.47	7.3	5.36	6.02	6.02	6.13	12.1	13.1	5.68	8.08	7.92	6.08	7.76	5.6	7.44	8.5	5.71	7.84	5.14	4.85	6.76	6.78
Eu	1.63	1.4	2.12	1.84	2.34	2.06	1.9	1.81	2.13	3.56	3.59	2	2.42	2.89	2.08	2.56	2.2	2.3	2.82	1.46	2.49	1.64	1.59	1.41	2.04
Gd	4.74	4.03	6.24	5.8	6.99	5.51	6.02	5.52	6.36	12	9.8	5.5	7.6	6.98	5.75	6.73	4.74	6.31	7.29	4.41	7.27	4.22	4.85	5.64	6.76
Tb	0.74	0.64	0.92	0.89	1.03	0.81	0.86	0.82	0.98	1.84	1.32	0.92	1.16	1.15	0.85	1.07	0.73	0.89	1.22	0.71	1.09	0.63	0.79	0.81	1.04
Dy	3.97	3.46	5.01	4.9	5.8	4.77	4.65	4.54	5.56	10.4	7.11	5.52	6.66	6.56	5.06	6.05	3.96	5.16	6.78	4.07	6.5	3.65	4.44	4.24	5.56
Ho	0.75	0.62	0.92	0.88	1.05	0.87	0.89	0.83	1.02	1.92	1.24	1.01	1.18	1.18	0.92	1.09	0.71	0.93	1.27	0.71	1.2	0.66	0.77	0.75	1.07
Er	1.94	1.66	2.37	2.49	2.78	2.33	2.35	2.22	2.76	5.16	3.33	2.89	3.23	3.36	2.7	2.8	1.92	2.41	3.5	1.98	3.24	1.85	2.13	1.99	2.91
Tm	0.28	0.24	0.31	0.34	0.37	0.32	0.32	0.31	0.40	0.69	0.47	0.41	0.43	0.50	0.38	0.38	0.25	0.32	0.48	0.27	0.45	0.26	0.30	0.27	0.39
Yb	1.63	1.52	1.94	1.99	2.25	2.04	1.97	1.95	2.5	4.15	2.89	2.44	2.58	3.14	2.34	2.53	1.56	2.11	3.05	1.65	2.73	1.59	1.78	1.63	2.54
Lu	0.23	0.21	0.29	0.30	0.33	0.31	0.29	0.31	0.36	0.62	0.46	0.41	0.38	0.45	0.35	0.40	0.24	0.32	0.47	0.24	0.40	0.24	0.24	0.222	0.37
Hf	3.6	2.9	4.5	3.7	5.5	3.9	4.3	3.8	4.5	8.6	7.2	4.3	6	5.1	4.4	5.5	3.5	4.9	6	3.7	5.9	3.4	3.2	3.5	5.3
Ta	2.1	1.5	2.08	1.45	2.39	1.59	1.97	2.08	1.66	4.03	6.48	1.84	2.36	1.94	1.85	2.26	1.6	2.32	2.41	1.48	2.39	1.51	1.28	3.07	2.25
W	4.8	20.2	<0.5	0.7	0.7	1.8	0.5	0.7	0.7	1.1	1	<0.5	0.5	1.4	1.2	1.1	1.9	2	0.9	1.4	0.8	1	<0.5	<0.5	<0.5
Tl	0.08	0.09	<0.05	<0.05	<0.05	0.09	<0.05	0.05	0.06	0.14	<0.05	<0.05	<0.05	0.23	0.11	0.21	0.07	0.08	0.15	<0.05	0.06	0.05	<0.05	0.1	<0.05
Pb	<5	<5	<5	<5	<5	8	<5	<5	<5	<5	<5	<5	<5	<5	<5	<5	<5	<5	<5	<5	<5	<5	<5	<5	<5
Bi	<0.1	<0.1	<0.1	<0.1	<0.1	<0.1	<0.1	<0.1	0.1	<0.1	<0.1	<0.1	<0.1	<0.1	<0.1	<0.1	<0.1	<0.1	<0.1	<0.1	<0.1	<0.1	<0.1	<0.1	<0.1
Th	2.75	1.94	2.88	2.23	3.29	2.3	2.78	4.3	3.63	5.95	14.7	3.68	4	3.07	2.41	4.26	3.77	5.59	3.79	3.55	3.69	3.62	1.73	3.74	3.9
U	0.67	0.48	1.04	0.57	0.92	0.56	0.7	1.04	0.96	1.56	3.26	0.9	0.86	0.73	0.58	0.99	0.91	1.36	0.88	0.78	0.88	0.88	0.46	0.95	0.89
Total	100.1	99.07	100.6	100.4	98.73	99.63	99	98.71	98.69	100.2	100.7	100.2	100.2	99.41	100.7	100.2	100.2	100.4	99.8	99.9	100.2	100.2	100.7	100	100.5

Sample	18RC115-2	18RC120-1	18RC123-1	19RC174-1	19RC176-1	19RC177-1	19RC178-1	19RC179-1	19RC180-1	19RC182-1	19RC185-2	19RC187-1	19RC189-1	19RC190-1	19RC191-1	19RC195-1	19RC196-1	19RC199-2-1	19RC205-1	19RC206-1-2	19RC211-1	19RC220-1	19RC229-1	19RC231-1	19RC235-1
Rock type	basalt	basalt	basalt	basalt	basalt	basalt	basalt	p. basalt	basalt	basalt	basalt	basalt	basalt	basalt	basalt	basalt	basalt	basalt	basalt	basalt	basalt	basalt	p. basalt	p. basalt	basalt
Lat	62.834594	62.850472	62.840495	62.465852	62.465376	62.466487	62.469462	62.470018	62.472834	62.4793	62.466963	62.464673	62.470213	62.4767	62.47039	62.48521	62.489023	62.494199	62.437287	62.438662	62.468791	62.456963	62.461328	62.459622	62.441758
Long	−134.85467	−134.7811	−134.7963	−133.10426	−133.11318	−133.11739	−133.12348	−133.1267	−133.12675	−133.1261	−133.09816	−133.09059	−133.09536	−133.093	−133.1024	−133.07539	−133.0819	−133.108877	−133.1304	−133.13304	−133.1467	−133.0404	−133.0076	−132.99688	−132.97517
%																									
SiO_2	49.23	46.82	41.98	47.62	47.18	45.71	45.55	45.04	45.81	47.16	49.91	47.93	46.9	46.27	45.59	41.18	48.44	47.96	47.34	48.1	46.2	39.8	44.23	44.6	45.49
Al_2O_3	14.14	13.67	14.16	14.3	14.62	14.48	14.55	14.42	14.43	14.52	13.47	13.88	13.54	13.3	14.77	14.39	13.98	13.4	13.6	13.52	13.95	14.01	15.94	14.46	15.24
$Fe_2O_3(T)$	14.06	14.83	12.09	13.17	13.49	12.4	12.68	13.16	12.84	12.04	12.66	11.7	15.5	13.98	16.2	13.31	12.72	14.74	11.5	11.61	13.25	12.52	8.48	11.8	9.38
MnO	0.16	0.10	0.13	0.14	0.21	0.18	0.20	0.21	0.18	0.19	0.13	0.14	0.19	0.15	0.13	0.12	0.11	0.19	0.18	0.16	0.18	0.08	0.15	0.19	0.14
MgO	5.81	6.31	6.94	6.13	6.26	5.47	6.06	7.21	7.26	7.17	5.78	5.93	6.02	5.62	6.14	5.21	5.38	4.99	6.74	6.94	7.37	5.52	3.57	5.05	3.87
CaO	5.88	2.78	7.62	6.13	6.42	12.75	10.8	8.16	7.46	6.54	6.79	4.29	5.56	6.96	3.67	8.86	5.36	7.65	8.64	8.29	7.59	8.81	9.64	8.18	8.39
Na_2O	2.31	1.98	3.31	3.99	3.59	1.74	2.09	1.42	2.21	2.04	5.34	3.14	3.51	2.73	3.92	2.67	4.33	3.13	3.35	3.37	3.91	2.18	0.89	2.04	0.49
K_2O	1.78	3.53	0.55	1.63	1.87	1.88	2.03	3.53	3.03	3.99	0.34	3.8	1.56	1.04	1.14	2.98	0.79	1.88	1.66	1.67	0.52	1.88	3.82	2.45	2.82
TiO_2	3.15	2.60	2.63	2.60	2.65	2.61	2.53	2.53	2.54	2.15	2.71	2.48	3.69	3.04	4.04	2.97	2.88	2.76	2.42	2.33	3.09	2.81	2.55	2.25	3.19
P_2O_5	0.46	0.4	0.35	0.31	0.32	0.32	0.3	0.3	0.31	0.24	0.35	0.31	0.48	0.41	0.52	0.42	0.41	0.35	0.32	0.31	0.43	0.35	0.32	0.28	0.56
LOI	3.29	5.68	9.73	2.89	2.42	2.02	2.3	2.73	3.55	2.61	2.41	5.02	2.49	5.82	3.33	7.84	5.09	1.77	2.76	2.25	2.69	11.08	9.09	7.57	9.33
ppm																									
Sc	34	31	32	9.6	5.4	2.7	3.3	3.5	4.4	5.3	5.3	28.9	4.5	12.5	13.5	11.3	17.8	4.3	4.4	3.5	5.4	21.9	13.8	26.4	14.7
Be	1	2	1																						
V	353	332	315	356	346	359	339	346	349	311	355	326	475	401	532	408	397	381	328	314	374	393	341	305	313
Cr	130	50	290	120	120	120	130	130	130	220	150	140	40	70	40	110	100	40	230	200	190	50	80	80	100
Co	54	45	47	45	48	34	42	45	42	46	37	37	42	42	45	40	39	45	43	43	48	42	27	40	23
Ni	100	30	200	78	80	70	78	80	77	103	68	61	36	63	40	60	59	41	115	92	103	53	63	68	38
Cu	200	60	140	132	122	122	128	134	137	124	121	56	56	83	20	13	7	87	137	137	140	63	123	149	13
Zn	170	140	120	101	117	69	91	98	97	94	92	104	131	126	191	222	126	136	77	108	119	143	28	75	61
Ga	23	25	21	23.1	22.8	22.5	24	25.6	25.2	21.3	16.2	22.4	27.6	22.5	24.3	24.1	23.5	22.9	18.6	16.2	17.8	24.4	22.3	22.8	26.3
Ge	1.9	1.4	1.4	<5	<5	<5	<5	<5	<5	<5	<5	<5	<5	<5	<5	<5	<5	<5	<5	<5	<5	<5	<5	<5	<5
As	<5	<5	<5	0.4	0.4	0.3	0.2	0.3	0.1	0.2	0.2	0.2	0.2	0.3	0.2	0.2	0.2	0.3	1.6	0.4	1.3	0.2	0.4	27.1	7.7
Rb	41	44	7	36	16.9	33.9	47.3	106.5	100.5	67.4	5.8	127	26.4	18.5	16.3	52.7	13.8	33	15.4	15.4	4.7	39.2	64.3	37	57.4
Sr	251	86	363	154	668	954	2310	783	612	345	349	222	303	275	71.3	113.5	123.5	460	218	207	283	225	82.8	111	124.5
Y	32.7	27.7	25.1	28.3	28.5	28.6	28.1	29.1	29.1	24.4	30.6	31	39.5	33	31	40	37	34.7	24.8	23.7	31.1	27.3	25.8	23.9	31.4
Zr	235	216	183	212	213	210	203	205	205	161	231	228	286	258	294	287	278	242	213	200	281	223	201	180	328
Nb	45	35.6	32.2	31.7	31.1	30.9	29.9	29.8	29.6	23	34.2	34.8	45.8	43.3	47.4	46.9	45	37.8	34.3	33	44.6	30.8	28.1	25.5	51
Mo	<2	<2	<2	<1	<1	1	2	<1	<1	<1	1	<1	1	1	1	1	1	1	1	<1	1	1	1	1	1
Ag	0.8	0.6	0.6	<0.5	<0.5	<0.5	<0.5	<0.5	<0.5	<0.5	<0.5	<0.5	<0.5	<0.5	<0.5	<0.5	<0.5	<0.5	<0.5	<0.5	<0.5	<0.5	<0.5	<0.5	<0.5
In	0.1	0.1	0.1	0.036	0.016	0.014	0.015	0.014	0.029	0.022	0.033	0.081	0.035	0.033	0.086	0.048	0.064	0.017	0.028	0.019	0.016	0.054	0.043	0.141	0.061
Sn	2	2	2	2	2	2	2	2	2	1	2	2	2	2	2	2	2	2	2	2	2	2	1	1	2
Sb	<0.2	<0.2	<0.2	<0.05	<0.05	<0.05	<0.05	<0.05	<0.05	<0.05	<0.05	0.06	<0.05	<0.05	0.05	<0.05	0.06	<0.05	<0.05	<0.05	0.05	0.64	0.91	2.84	1.49
Cs	2.8	1.3	1.9	3.49	0.4	0.85	0.85	2.22	2.05	1.41	0.38	23.9	0.49	0.79	0.27	0.73	0.49	1.42	0.96	1.21	0.3	1.62	4.38	3.42	8.18
Ba	3476	4856	2815	2760	2840	640	2530	1785	745	9510	1565	7630	1420	650	764	884	610	2030	7340	4560	531	2020	569	740	1070
La	31.8	29.6	25.5	24.3	25.5	24.8	23.6	22.9	24.3	18	25.7	29.2	34.7	32.6	32.8	25.3	34.6	31	27.7	21.7	29.4	24	21.8	14.6	37.7
Ce	69.5	61.8	54	53.3	54.3	53.9	52.1	51.8	52.2	39.5	56	61.9	74.9	69.1	72.9	64.1	76.2	65.1	60	53.2	72	52.6	49.1	32.5	81.2
Pr	8.48	7.71	6.79	6.65	6.91	6.75	6.81	6.68	6.55	5.13	7.18	7.71	9.55	8.55	8.9	8.36	9.23	8.18	7.75	6.77	9.76	6.61	6.45	4.19	10.4
Nd	35.3	33.1	28.5	29.8	30.5	30.1	29.9	30.5	29.3	22.9	32.2	32	41	37.3	39.8	36.9	39.2	36	31.5	30.6	43.1	26.9	24.9	16.8	38.9
Sm	8.15	7.05	6.01	7.33	6.96	6.92	6.85	6.48	6.75	5.55	7.28	7.27	10.75	8.12	9.22	8.83	9.01	8.37	6.74	6.62	9.02	5.88	5.82	3.95	8.39
Eu	2	1.88	1.84	1.86	1.9	2.23	2.14	2.19	2.15	1.81	2.06	1.99	2.82	2.53	2.17	2.73	2.42	2.1	1.97	1.92	2.68	2.2	2.04	1.4	2.65
Gd	7.52	6.68	5.97	7.08	7.28	6.69	6.76	6.69	6.82	5.8	7.37	7.36	9.57	8.2	8.82	8.61	8.05	7.8	6.18	5.82	8.53	5.46	5.82	4.3	7.78
Tb	1.19	1.07	0.93	0.94	1.04	1.02	1.03	0.97	1.02	0.8	1.08	1.09	1.38	1.19	1.19	1.45	1.21	1.13	0.88	0.86	1.13	0.98	0.88	0.74	1.13
Dy	6.43	5.67	4.88	6.06	6.22	6.34	5.51	5.95	6.13	5.15	6.56	6.27	7.93	6.9	7.55	8.52	7.79	7.15	5.16	5.26	7.1	5.85	5.13	4.3	6.48
Ho	1.19	1	0.91	1.12	1.06	1.13	1.06	1.09	1.09	0.8	1.23	1.21	1.49	1.33	1.33	1.51	1.36	1.33	0.98	0.87	1.27	1.13	1	0.92	1.24
Er	3.24	2.74	2.43	3.08	3.11	3.14	2.64	3.17	2.7	2.65	3.17	3.08	4.2	3.77	3.44	4.33	3.68	3.78	2.46	2.61	3.36	2.73	2.58	2.34	2.89
Tm	0.44	0.38	0.33	0.36	0.36	0.38	0.39	0.38	0.36	0.32	0.45	0.44	0.53	0.46	0.48	0.55	0.52	0.54	0.33	0.32	0.41	0.41	0.35	0.39	0.48
Yb	2.79	2.24	2.04	2.29	2.44	2.45	2.23	2.52	2.44	2.05	2.65	2.7	3.26	3.03	3.14	3.42	3.3	3.22	2.1	1.96	2.46	2.4	2.16	1.97	2.51
Lu	0.40	0.32	0.28	0.34	0.31	0.37	0.32	0.33	0.34	0.31	0.38	0.35	0.45	0.38	0.43	0.51	0.46	0.4	0.27	0.26	0.42	0.34	0.28	0.3	0.36
Hf	5.9	5.3	4.4	5.5	5.2	5.1	5.1	5.3	5	4.2	5.4	5.8	6.7	6.3	7.5	6.9	6.7	6	4.8	4.6	6.6	5.1	5	4.7	7.8
Ta	2.6	2.12	1.98	2	1.9	2	1.8	1.8	1.8	1.4	2	2	2.8	2.4	2.7	2.6	2.7	2.1	2.1	2	2.5	2.1	1.8	1.6	3.1
W	<0.5	<0.5	<0.5	1	2	1	1	1	1	1	1	1	1	1	1	3	1	1	<1	1	1	1	1	1	1
Tl	0.23	0.2	<0.05	0.05	<0.02	0.02	0.02	0.03	0.03	0.05	<0.02	0.31	<0.02	<0.02	<0.02	<0.02	<0.02	0.02	0.1	0.03	<0.02	0.03	0.18	0.28	0.15
Pb	<5	<5	<5	<2	5	4	7	3	6	4	<2	3	5	<2	<2	4	6	2	4	<2	<2	3	10	7	2
Bi	<0.1	<0.1	<0.1	<0.01	<0.01	<0.01	0.01	<0.01	<0.01	<0.01	0.01	0.01	<0.01	<0.01	0.01	<0.01	0.01	0.01	0.01	0.01	0.02	0.01	0.01	0.01	0.01
Th	3.88	4.32	2.93	2.63	2.63	2.63	2.53	2.47	2.53	1.78	2.85	3.97	4.05	3.9	4.31	5.33	5.04	3.97	3.16	3.09	4.01	2.77	2.64	2.4	4.78
U	0.95	1.12	0.69	0.63	0.65	0.71	0.62	0.59	0.62	0.48	0.75	0.97	1.04	0.94	1.09	1.31	1.16	0.95	0.78	0.75	0.92	0.71	0.72	0.54	0.88
Total	100.3	98.71	99.49	99.3	99.51	99.84	99.69	99.09	99.89	99.76	100.2	99.51	99.74	99.53	99.66	100.2	99.7	99.2	99.72	99.31	99.49	99.45	99.23	99.36	99.29

almost continuous section of basalt and associated volcanic breccia is at least 500 m thick (Fig. 4). Basalt near the base of this volcanic pile is interlayered with calcareous phyllite and rare lenses of reworked volcanogenic sandstone and siltstone. The volcanic succession may be 1800 m in true thickness according to the cross section of Pigage (2004); however, if interpreted normal faults are restored, the Menzie Creek Formation could be as thick as 2800 m.

Lithofacies and Lithofacies Associations

Menzie Creek Formation lithofacies and lithofacies associations are presented in Table 1 and Figure 4 based on the terminology of McPhie et al. (1993). Multiple lines of evidence suggest these rock units are submarine and include abundant pillow basalt and quench fragmentation textures.

Facies Association 1—Coherent Basalt and Gabbro

Coherent basalt up to several meters thick, including aphanitic, porphyritic, and amygdaloidal varieties, is found west of Mark's Mountain and near the Earn River (Figs. 3 and 5A). In this location, based on the description in Table 1, basalt with cross-sectional shapes characterized by flat bottoms and arcuate tops are interpreted to be lava tubes surrounded by basalt breccia (Fig. 5B).

Basalt that forms mounds made up of individual spherical-shaped bodies, as described in detail in Table 1, is interpreted to be pillow basalt. Pillow basalt is abundant near Mark's Mountain and occurs at several locations northeast of Tay Mountain (Fig. 3). Pillows range in size from 10 cm to 1 m in diameter (Figs. 5C–5E). Larger pillows typically have a large vesicle or amygdule in the center (Figs. 5D and 5E), whereas smaller pillows have small elongate vesicles radiating outward from the core of the pillow and small vesicles and amygdules near their outside edge (Fig. 5C). One ridge to the southwest of Mark's Mountain is partially composed of pillow basalts with a minimum thickness of 200 m (Fig. 4). Elsewhere, occurrences of pillow basalt typically form 10–50-m-thick mounds.

Coherent basalt and gabbro units are intercalated with calcareous sandstone and phyllite south of West Kalzas Mountain and near Duo Creek (Figs. 3 and 4). Gabbro bodies have a medium- and coarse-grained center with fine-grained margins and are generally concordant with bedding in the sedimentary rocks (Fig. 5F); however, locally, the gabbro is discordant with laminations in adjacent sedimentary rocks (Fig. 5G). Hornfels developed in sedimentary rocks adjacent to mafic intrusions.

Facies Association 2—Autoclastic Rocks

Several varieties of basalt breccia have been described in Table 1 and interpreted as pillow breccia and hyaloclastite breccia that surround pillow basalt and basalt tubes to the west of Mark's Mountain (Fig. 3). Some outcrop exposures show >20 m of breccia. Pillow breccia units contain two different volcanic clast sizes, including smaller (1–3 cm) altered clasts, and larger (6–8 cm), relatively fresh angular clasts (Fig. 6A). The breccia has a basaltic matrix with rare spherulites that is interpreted to be original glassy material (Fig. 6B). Hyaloclastite breccia comprises angular clasts of very fine-grained basalt in a glassy (?) basaltic matrix (Fig. 6C). A third variety of breccia is composed of smaller aphanitic basalt clasts with devitrified or altered rims between larger, variably vesicular basalt clasts (Fig. 6D). The matrix of this volcanic breccia comprises angular ash to lapilli-sized basaltic clasts.

Facies Association 3—Resedimented Volcanic Rocks

This facies association comprises rocks that show sorting of volcanic fragments and subtle to prominent bedding features. West of Mark's Mountain, lenses of volcanic-derived siltstone interbedded with sandstone occur in the lowermost part of the volcanic stratigraphy (Figs. 3 and 7A). Coarse-grained, volcanic-derived sandstone units contain clasts of well-rounded scoria and basalt (Fig. 7B). This sandstone horizon yields zircon grains that were large enough to be separated and dated by U-Pb methods (sample 19RC210-1). Volcanogenic siltstone, northeast of Tay Mountain (Fig. 3), contains ash-sized grains of feldspar and chlorite-altered mafic minerals interbedded with fine-grained volcanogenic sandstone with rare pebble trains. Volcanogenic conglomerate at one location is crudely bedded with pebbly sandstone (Fig. 7C). Several outcrops near the top of the topographic high, north of Duo Creek, comprise volcanogenic breccia with both lapilli and ash-sized volcanic grains and lithic grains that are interpreted to be resedimented (Figs. 3 and 7D); a rock from this location contained zircon crystals that were dated by U-Pb methods (sample 18RC124-2). Locally, these rocks are well bedded, with coarse-grained sandstone beds that contain euhedral feldspar grains interlayered with thin beds of siltstone.

GEOCHRONOLOGY

19RC210-1: Volcaniclastic Sandstone (Menzie Creek Formation)

Coarse-grained, volcaniclastic sandstone near the interpreted base of the Menzie Creek Formation, ~7 km west-southwest of Mark's Mountain (Figs. 3 and 4), yielded euhedral, oscillatory, and/or sector-zoned elongate (aspect ratios of ~2:1) zircon grains that range in size from 100 µm to 160 µm (Fig. S1). Seven LA-ICP-MS analyses of four zircon grains yielded individual $^{206}Pb/^{238}U$ dates of 488 ± 8–475 ± 9 Ma (Table S1). Six zircon grains analyzed by CA-TIMS yielded weighted mean $^{206}Pb/^{238}U$ dates of 484.38 ± 0.14/0.27/0.57 Ma (mean square of weighted deviates [MSWD] = 0.9, probability of fit [pof] = 0.46; Table 2; Fig. 8).

Figure 5. Coherent volcanic facies. (A) Amygdaloidal basalt where banded amygdules are filled with calcite. (B) Tube of basalt displaying an arcuate top (black arrow) and flat bottom surrounded by basalt breccia. (C–E) Pillow basalt displaying the range in sizes of pillows from meter scale to 10-cm scale. (F) Weathered surface of coarse-grained gabbro from a larger intrusive body. (G) Fine-grained gabbro sill with a chilled margin that cuts off bedding at a moderate angle (S_0).

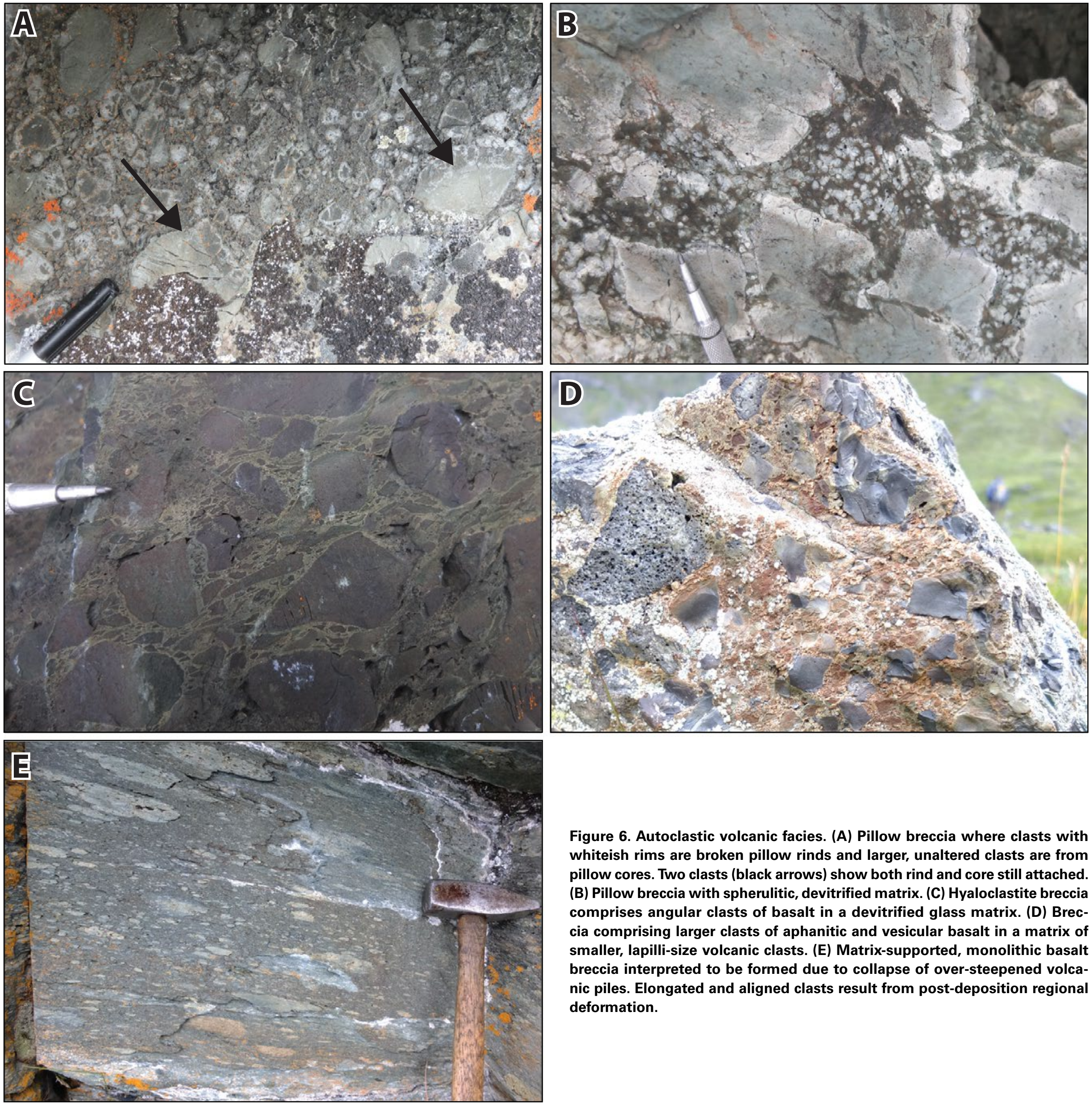

Figure 6. Autoclastic volcanic facies. (A) Pillow breccia where clasts with whiteish rims are broken pillow rinds and larger, unaltered clasts are from pillow cores. Two clasts (black arrows) show both rind and core still attached. (B) Pillow breccia with spherulitic, devitrified matrix. (C) Hyaloclastite breccia comprises angular clasts of basalt in a devitrified glass matrix. (D) Breccia comprising larger clasts of aphanitic and vesicular basalt in a matrix of smaller, lapilli-size volcanic clasts. (E) Matrix-supported, monolithic basalt breccia interpreted to be formed due to collapse of over-steepened volcanic piles. Elongated and aligned clasts result from post-deposition regional deformation.

18RC124-2: Volcanogenic Sandy Breccia (Menzie Creek Formation)

Menzie Creek Formation volcanogenic breccia that contains subangular clasts of orange-brown weathering basalt and shale chips in a sandy matrix was collected 1 km south of Duo Creek (Figs. 3 and 4). Zircon crystals range in size from 80 µm to 180 µm and show equant to elongate morphologies with aspect ratios of 1:1–4:1. Stubby grains have sector zoning, and elongate grains have oscillatory zoning (Fig. S1). Twenty-three zircon grains yielded individual $^{206}Pb/^{238}U$ LA-ICP-MS dates of 507 ± 10–465 ± 8 Ma (Table S1). Seven grains analyzed by CA-TIMS yielded weighted mean $^{206}Pb/^{238}U$ dates of 484.20 ± 0.14/0.27/0.57 Ma (MSWD = 0.5, pof = 0.77; Table 2; Fig. 8).

20RC234-1: Volcanogenic Pebbly Sandstone (Crow Formation)

Purplish, quartz-rich, volcanogenic pebbly sandstone of the Crow Formation contains both angular and rounded quartz, feldspar, and calcite grains, rounded grains of basalt, and dark gray shale chips in a fine-grained, calcareous

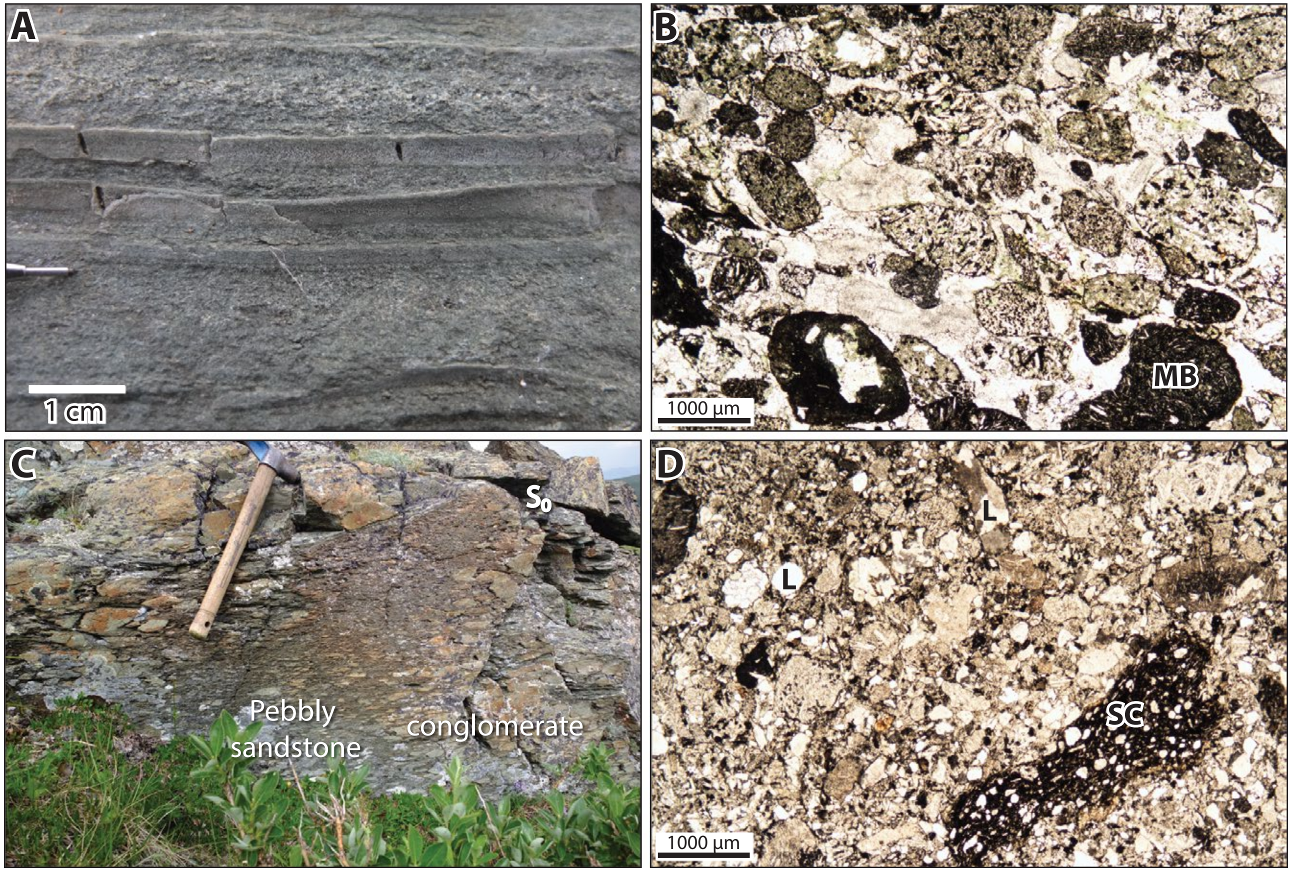

Figure 7. Volcaniclastic facies. (A) Thin-bedded siltstone and sandstone comprising basaltic detritus. Coarse-grained sandstone layer yielded zircon that was dated by chemical abrasion–thermal ionization mass spectrometry (CA-TIMS; 19RC210-1). (B) Photomicrograph of sandstone layer from the same outcrop as in panel A. MB—aphanitic basalt. (C) Crudely bedded conglomerate (S_0) comprising subrounded clasts of volcanic rocks interlayered with pebbly volcanogenic sandstone. (D) Crystal-lithic lapilli-tuff comprising sand- to pebble-sized clasts of scoria (SC) and lithic (L) grains. This sample yielded zircon that was dated by CA-TIMS (18RC124-2).

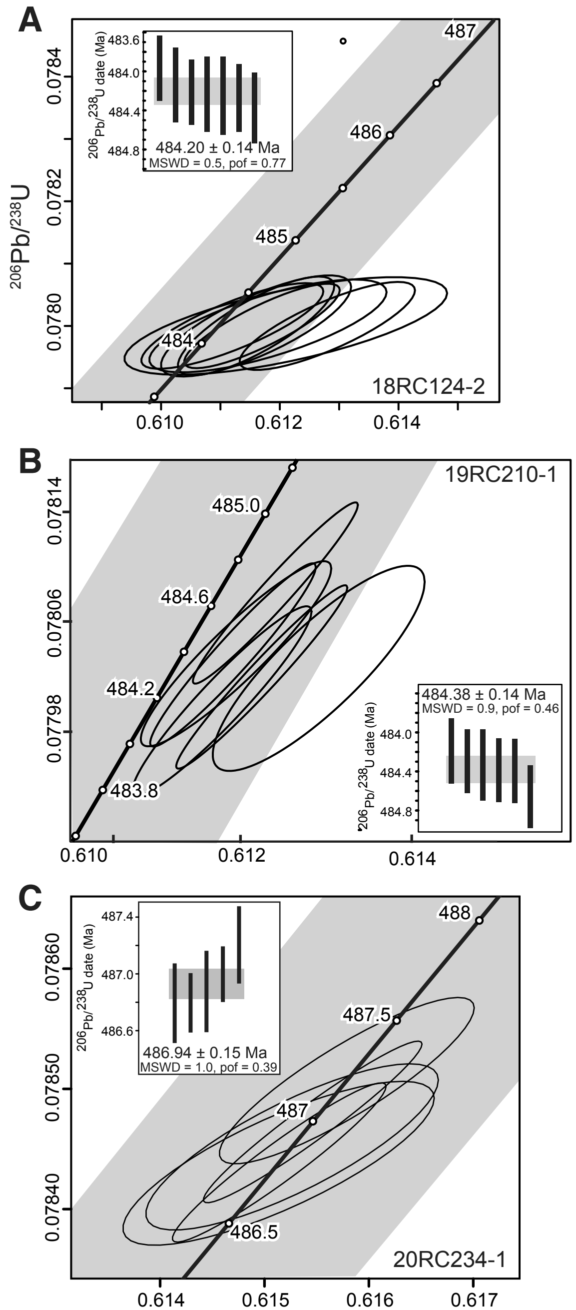

matrix. Zircon crystals range in size from 90 µm to 500 µm and are dominantly equant with sector zoning (Fig. S1). Forty-four zircon grains yielded individual ^{206}Pb/^{238}U LA-ICP-MS dates of 507 ± 31–447 ± 17 Ma (Table S1). Five grains analyzed by CA-TIMS yielded weighted mean ^{206}Pb/^{238}U dates of 486.94 ± 0.15/0.21/0.55 Ma (MSWD = 1.0, pof = 0.39, Table 2; Fig. 8). Based on age data, we assign this sample, 20RC234-1, to the Crow Formation and use that designation throughout the paper.

LITHOGEOCHEMISTRY

Whole-Rock Major and Trace Element Compositions

Efforts were taken to sample the least altered rocks of the Menzie Creek Formation because they have been metamorphosed to greenschist facies during regional deformation (Read et al., 1991). Mafic minerals and glass are replaced by epidote and chlorite; in some cases, secondary calcite fills amygdules and occurs as cross-cutting veinlets, and sulfides are present as disseminated crystals. Major elements (except Al_2O_3, TiO_2, and P_2O_5) and low field strength elements (LFSEs: Ba, Sr, Cs, and Rb) are considered mobile during seafloor alteration and greenschist facies metamorphism. As a result, the discussions below are based on immobile element systematics (Whitford et al., 1989; MacLean, 1990). Rare earth elements (REEs), high field strength elements (HFSEs: Zr, Hf, Nb, Ta, and Y), transition elements (Ti, V, Cr, and Ni), and Th are considered relatively immobile under the metamorphic and alteration conditions experienced by rocks of the Menzie Creek Formation (Lesher et al., 1986; MacLean, 1990; Jenner, 1996). To ensure confidence in the immobility of key element and element ratios used in the interpretation of the Menzie Creek Formation rocks, they are plotted against the Al_2O_3/Na_2O alteration index to ensure that no correlation exists that would suggest the element concentrations are controlled by secondary processes, such as those listed above (Figs. 9A and S3, see footnote 1; Spitz and Darling, 1978; Piercey et al., 2002). Some of the samples from the Menzie Creek Formation exhibit evidence of Na loss (Fig. 9B; e.g., Ruks et al., 2006); however, only three samples were omitted from the results based on: (1) high loss on ignition values (LOI >10); (2) very high Al_2O_3/Na_2O (>35); (3) very low silica values (SiO_2 <39%); and (4) abundant secondary calcite replacing feldspar phenocrysts. All other samples are presented herein.

Figure 8. Concordia plot of chemical abrasion–thermal ionization mass spectrometry ^{206}Pb/^{238}U dates from zircon and ranked date plot (inset) for (A) 18RC124-2, (B) 19RC210-1, and (C) 20RC234-1. Grey band on concordia plot shows decay constant uncertainty. Error bars and ellipses are at 2 sigma. Weighted mean date is shown and represented by gray box behind the error bars. MSWD—mean square of weighted deviates; pof—probability of fit.

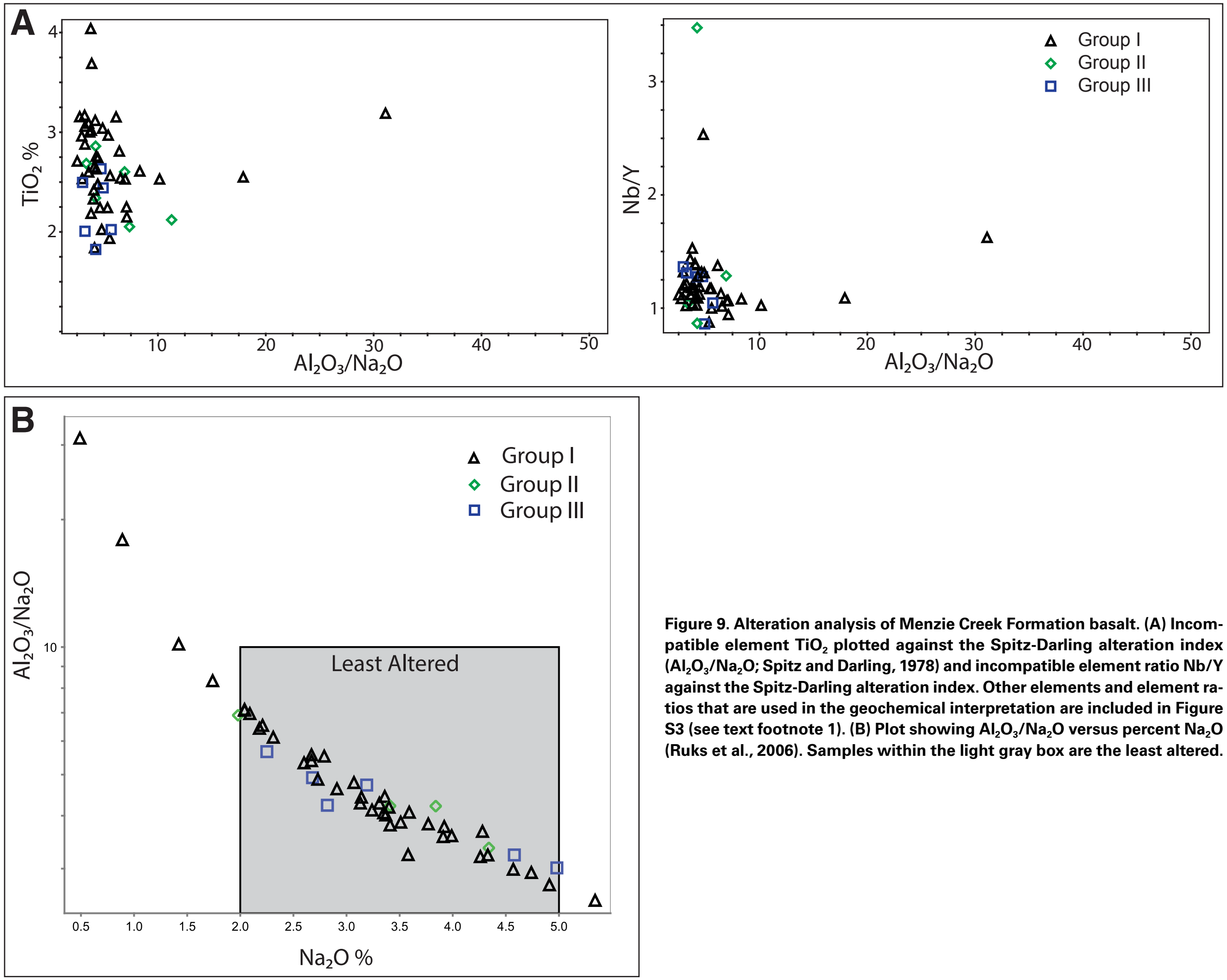

Figure 9. Alteration analysis of Menzie Creek Formation basalt. (A) Incompatible element TiO_2 plotted against the Spitz-Darling alteration index (Al_2O_3/Na_2O; Spitz and Darling, 1978) and incompatible element ratio Nb/Y against the Spitz-Darling alteration index. Other elements and element ratios that are used in the geochemical interpretation are included in Figure S3 (see text footnote 1). (B) Plot showing Al_2O_3/Na_2O versus percent Na_2O (Ruks et al., 2006). Samples within the light gray box are the least altered.

Menzie Creek Formation rocks have basaltic Zr/Ti ratios (0.008–0.039) and are alkaline based on elevated Nb/Y (0.86–3.48) ratios (Fig. 10). Chromium and Ni concentrations range from 30 ppm to 800 ppm and 30–300 ppm, respectively. The suite has elevated TiO_2 (1.82–4.04%) contents relative to those of the primitive mantle (TiO_2 = 0.22%), and the Al_2O_3/TiO_2 ratios (5–8) are lower than those of the primitive mantle (~21) and normal mid-oceanic-ridge basalt (N-MORB; ~11). Some samples have values between those of oceanic-island basalt (OIB) and enriched mid-oceanic-ridge basalt (E-MORB; ~5–9.5; Table 3; Sun and McDonough 1989). The P_2O_5 values range from 0.21% to 0.71%, with one sample having a value of 1.05%, which is in the range of average OIB (~0.62%; Sun and McDonough 1989). Compared to the primitive mantle, the Menzie Creek Formation rocks have strong light rare earth element (LREE) enrichment (La_{pm}/Sm_{pm} = 1.8–4.1, with one sample ~5.7) and heavy rare earth element (HREE) depletion compared to LREE (Sm_{pm}/Yb_{pm} = 2.2–5.0; Table 3).

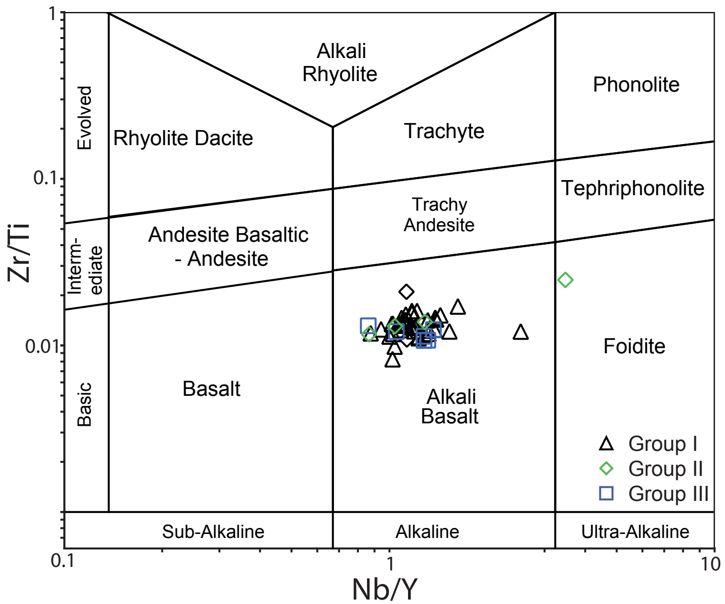

Figure 10. Menzie Creek Formation volcanic rocks plotted on discrimination diagram of Pearce (1996).

Menzie Creek Formation rocks are divided into three geochemical groups based on their primitive mantle (pm)-normalized Th-Nb-La systematics. Group I rocks comprise the majority of the samples and have positive Nb anomalies relative to Th and La (Fig. 11A). Group II rocks show a flat pattern among these three elements (Fig. 11B), and Group III rocks have a negative Nb anomaly with respect to Th and La (Fig. 11C). All three groups have elevated Hf and Zr relative to Sm (Zr_{pm}/Sm_{pm} = 0.86–1.81, pm-normalized; Figs. 11A, inset, and 12A). The primary distinction between groups I and III is the higher Th concentration in the latter, whereas the Nb concentrations have a similar range of concentrations among the groups.

Basalt samples typically plot on or near the mantle array and show within-plate affinities in Zr-Th-Nb space (Figs. 12B and S4, see footnote 1). Group I rocks plot entirely within the mantle array in Th/Yb-Nb/Yb space, between average OIB and E-MORB values (Fig. 12B; Pearce, 2014; Shervais, 2022). Group III rocks sit outside the mantle array toward higher Th/Yb values, and Group II rocks straddle the edge of the mantle array and have Th/Yb values intermediate between those of Groups I and III. Similarly, on plots of Th/Nb versus La/Sm and Zr, Group I rocks plot near the average values of OIB and between those of OIB and E-MORB, whereas those of Groups II and III plot toward higher Th/Nb for given values of both La/Sm and Zr (Figs. 12C and S4); in all of these plots, the Th/Nb values approach the average values of lower and bulk continental crust. There is a clear separation between Nb/U values among Group I and groups II and III (Fig. S4). Although U can be mobile in environments exposed to oxidizing fluids (Brenan et al., 1995), the correlation between U and Nb suggests that the patterns shown in Figure S4 are a feature of primary magmatic processes and not secondary processes such as alteration. On a plot of Nb versus U, Group I overlaps with the Nb/U values of modern oceanic basalts, and groups II and III are displaced toward lower Nb/U values typical of continental crust.

Whole-Rock Nd and Hf Isotope Compositions

Group I rock samples to the southwest of Mark's Mountain (19RC205-1) and north of Duo Creek (18RC115-1; Fig. 1) yield initial $^{143}Nd/^{144}Nd$ = 0.512166–0.512161 and εNd_{484} = +2.9–3.0, and initial $^{176}Hf/^{177}Hf$ = 0.282600–0.282622 and εHf_{484} = +4.3 to + 5.0 (Figs. 13 and S1), respectively. Group III rock samples collected south of Duo Creek (18RC237-1) and Mount Menzie (Fig. 3; 15RC282-1) yielded initial $^{143}Nd/^{144}Nd$ = 0.512066–0.512090 and εNd_{484} = +1.0 to +1.3, and initial $^{176}Hf/^{177}Hf$ = 0.282542 and 0.282571 and εHf_{484} = +3.3 to +4.3 (Fig. 13; Table S2, see footnote 1).

DISCUSSION

Volcanic Facies Interpretations of the Menzie Creek Formation

Submarine volcanism associated with rift systems is dominated by mafic magmas that typically erupt effusively, resulting in either flows, tubes, or pillows, depending on flow rate and distance to a vent or fissure (White et al., 2015). For example, massive basalt flows are abundant at fast-spreading mid-oceanic ridges where the magma flow rate is high (Soule, 2015). This contrasts with seamounts where massive flows are rare and pillow basalt is the most common lava type (Staudigel and Koppers, 2015). Some modern seamounts show a progression from sheet flows to tubes to pillows with increasing distance from a vent (White et al., 2015). Brecciation of coherent basalt is also common during submarine eruptions, because: (1) magma quenches when it encounters cold seawater; (2) gravitational collapse of flow fronts occurs on the flanks of seamounts; and (3) steep parts of volcanic edifices collapse into disaggregated basaltic material (i.e., spalling and granulation; McPhie et al., 1993). Bedded volcaniclastic rocks are typically found skirting seamounts as aprons and are less common near vents (Staudigel and Koppers, 2015).

The fine-grained texture of coherent, aphanitic, and porphyritic basalt units in Facies Association 1, the local occurrence of amygdaloidal basalt, and the association of basalt with basalt-dominated volcaniclastic rocks (e.g., volcanic breccia) may indicate that the Menzie Creek Formation formed due to subaqueous eruptions. Gabbro bodies with chilled margins and coarser-grained centers,

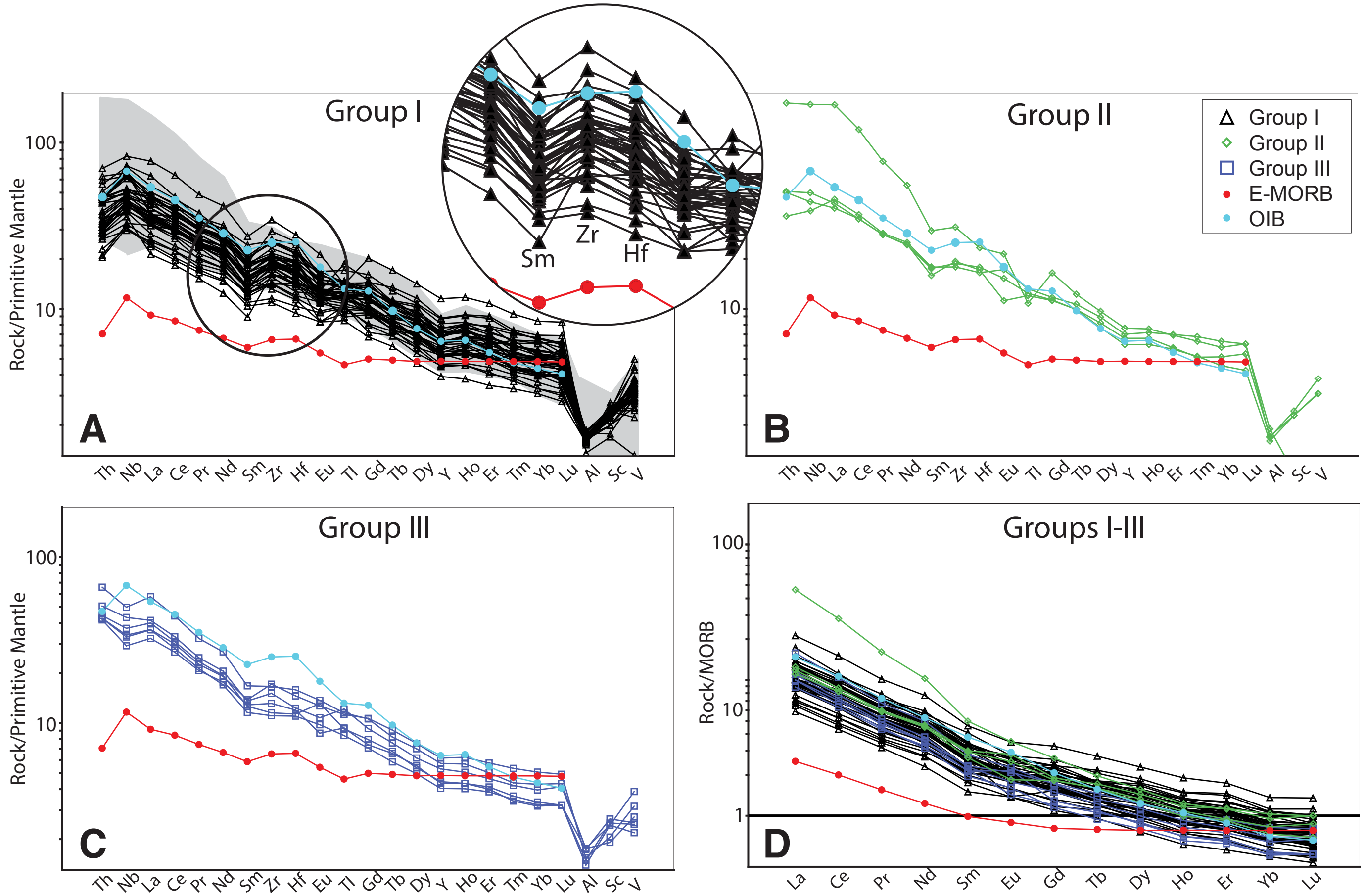

Figure 11. (A–C) Primitive mantle-normalized plots using immobile elements. Element incompatibility increases to the left of the diagrams. Grey polygon delineates Kechika group gabbro and basalt from south-central Yukon (Campbell et al., 2019). (D) Mid-oceanic-ridge basalt (MORB)–normalized plots using rare earth elements for all Menzie Creek Formation samples. Light blue curve is average oceanic-island basalt (OIB), and red curve is average enriched mid-oceanic-ridge basalt (E-MORB; Sun and McDonough, 1989).

the lack of spatially associated volcaniclastic rocks, and the bedding-parallel nature of the Facies Association 1 units suggest they are sills. These intrusions are interpreted to be part of a sill-sediment complex that may contain up to three stacked sills. Near Duo Creek, larger bodies of coarse-grained gabbro are interpreted to be bulbous sills or enlarged dikes (Fig. 3).

The abundance of hyaloclastite breccia units in Facies Association 2 suggests that basalt erupted in a submarine environment, and by association, the units in Facies Association 1 must have also erupted subaqueously. The hyaloclastite and pillow breccia units formed when lava flows, tubes, and pillows quenched and fragmented upon contact with cold seawater (White et al., 2015). Spherulites and chlorite-rich matrix are interpreted to be devitrification textures that formed following the breakdown of basaltic glass.

Bedded volcanogenic deposits of Facies Association 3 are interpreted to have formed from a combination of: (1) eruptive events during which particles were ejected into the water column and sorted during deposition; and (2) collapse and deposition of over-steepened parts of the seamount. Laminated to thin-bedded volcanogenic units likely formed from ash transported through water where the deposits were well-sorted during transport and deposition

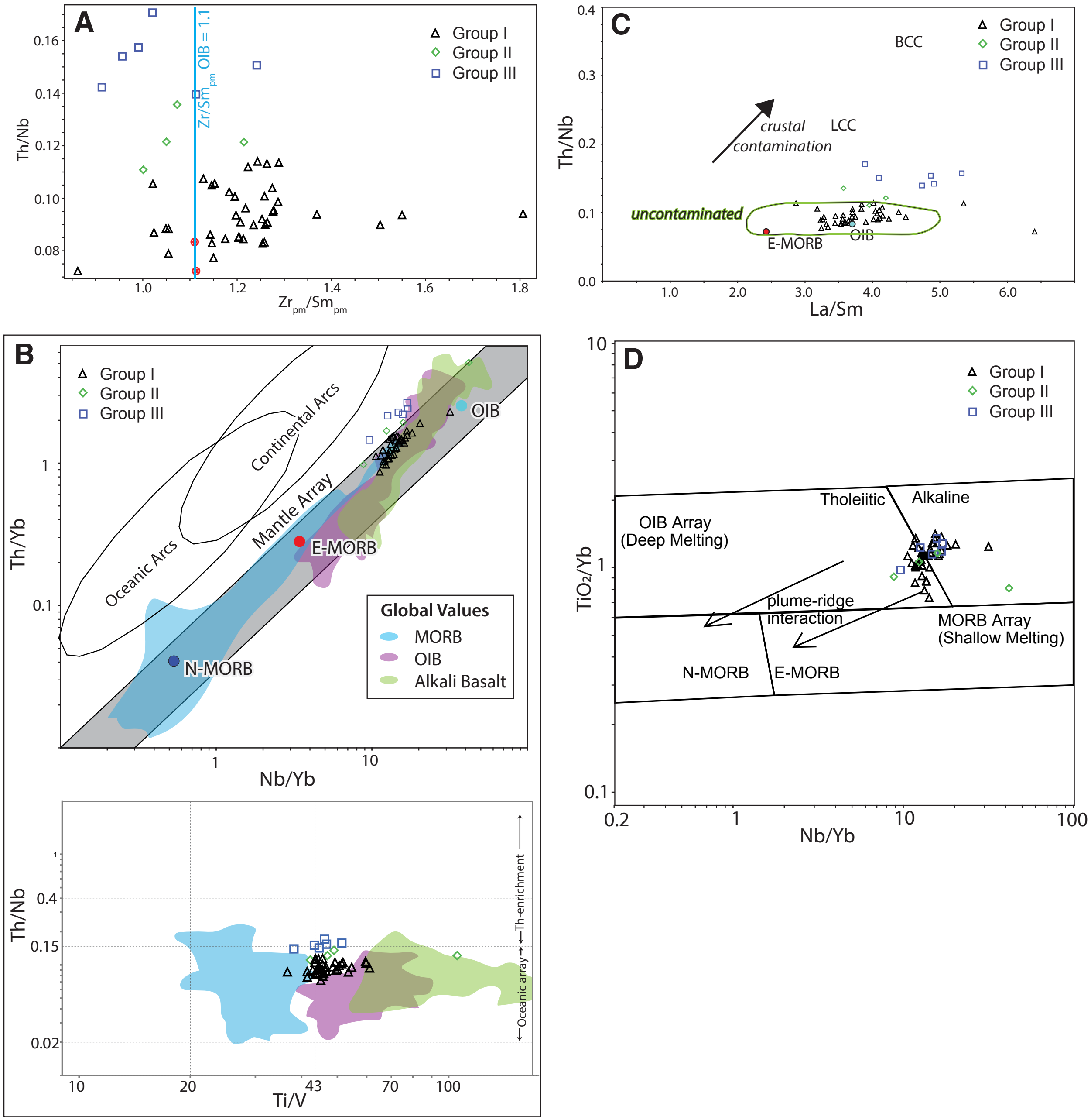

Figure 12. Trace element plots illustrate differences in the three geochemical groups of the Menzie Creek Formation rocks. (A) Th/Nb versus primitive mantle-normalized Zr/Sm. Most Menzie Creek Formation Group I samples show higher Zr/Sm ratios than average oceanic-island basalt (OIB). (B) Upper plot shows Th/Yb versus Nb/Yb with Menzie Creek Formation rocks superimposed on the mantle array. Lower plot is Th/Nb versus Ti/V, modified from Shervais (2022) to show Th-enrichment of groups II and III compared to Group I of the Menzie Creek Formation. Colored shapes approximate the majority of global data for MORB (blue), OIB (purple), alkali basalt (green) from Shervais (2022), and enriched mid-oceanic-ridge basalt (E-MORB; red). Menzie Creek Formation Group I rocks plot on the array, near OIB. Group II and III rocks plot on the array boundary and off the array toward values of continental arcs, respectively (Pearce, 2008). (C) The trend of Group II and III rocks from mantle-derived values toward values of continental crust on Th/Nb versus La/Sm suggest the three geochemical groups may result from mantle-derived magmas being partially contaminated by continental crust. BCC—bulk continental crust, LCC—lower continental crust. (D) Diagram using TiO_2/Yb versus Nb/Yb to differentiate deep melting versus shallow melting (Pearce, 2008). N-MORB—normal mid-oceanic-ridge basalt.

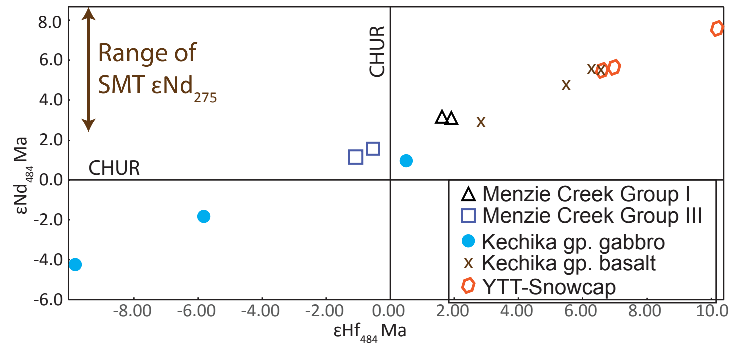

Figure 13. Initial εNd versus initial εHf of Menzie Creek Formation volcanic rocks. Also shown are values from the Kechika group (gp.) of south-central Yukon, Snowcap Assemblage of Yukon-Tanana terrane (YTT-Snowcap), and the Slide Mountain terrane (SMT; Campbell et al., 2019; Piercey and Colpron, 2009; Piercey et al., 2012). CHUR—chondritic uniform reservoir.

(e.g., Fouquet et al., 1998; Sohn et al., 2008). These units are mapped up to 7 km from basalt and hyaloclastite breccia units and are interpreted to have formed blankets of ash. Crudely bedded, volcanogenic conglomerate (Fig. 7C) and sandstone (Fig. 7B) probably formed due to the transport of fragments of basaltic rocks downslope, where they became rounded and sorted before deposition (e.g., Staudigel and Koppers, 2015). These deposits are mapped up to several kilometers from areas dominated by basalt and hyaloclastite breccia. Green, fine-grained chlorite schist units that are interbedded with massive basalt near the Earn River may be a metamorphosed equivalent to volcaniclastic siltstone and sandstone.

Seamount Deposits in the Menzie Creek Formation

Field observations of Menzie Creek Formation lithofacies, such as the thickness and overall volume of the basaltic rocks west of Mark's Mountain, the specific facies and distribution of facies of the mafic volcanic and volcaniclastic rocks, the lack of massive lava flows, and the shape of the volcanic deposits, are consistent with the interpretation that the volcanic rocks (Omv) are partially preserved seamounts (Fig. 14; Staudigel and Koppers, 2015). Seamounts, isolated topographic features rising from 100 m to 7 km above the surrounding seafloor, form in varying tectonic settings and contain facies dominated by pillow basalt, autoclastic breccia, and volcaniclastic rocks (Staudigel et al., 2010; Staudigel and Koppers, 2015). The Menzie Creek Formation volcanic rocks share several features with modern seamounts, including: (1) an abundance of hyaloclastite breccia (e.g., Smith and Batiza, 1989; Davis and Clague, 2003); (2) abundant pillow basalt; (3) volcaniclastic aprons (Staudigel and Koppers, 2015); and (4) rough conical shape (e.g., Pe-Piper et al., 2013). For example, Miocene seamounts offshore of central California contain abundant hyaloclastite deposits composed of basaltic glass fragments similar to breccias observed near Mark's Mountain (Davis and Clague, 2003). Facies models for modern seamounts along the East Pacific Rise include an apron of hyaloclastite deposits between lava vents and more vent-distal deposits composed of basalt pillows and tubes (Smith and Batiza, 1989).

The Menzie Creek Formation seamounts may have reached heights of several kilometers based on the regional mapping by Pigage (2004). At minimum, there is 1 km of basalt and basalt breccia documented in this study and a cross sectional, true thickness for the Menzie Creek Formation of ~1.8 km near Mark's Mountain, which represents the southeasternmost seamount (plate 2 in Pigage, 2004). Thinly bedded volcaniclastic siltstone and sandstone occur along the margins of the volcanic rocks mapped near Tay Mountain and near the top of the volcanic stratigraphy north of the Earn River. Basalt breccia included within Facies Association 2 occurs near the margins of the volcanic rocks near Mark's Mountain and Tay Mountain and may represent reworked and locally transported volcanic material deposited on the flanks of the seamount. The breccia is locally crudely bedded near Tay Mountain, which supports a reworked and transported origin for these rocks. The conical shape of the Menzie Creek Formation is also comparable to modern seamount geometries. Although the Menzie Creek seamounts have been variably deformed and partially eroded, their shape on the map is interpreted to reflect the original geometries because they are preserved within a single thrust panel, and the competent nature of the volcanic rocks allowed preservation of most primary features in the volcanic stratigraphy and facies (Fig. 3).

Petrogenesis of Menzie Creek Formation

Alkali basalts with compositions similar to those of the Menzie Creek Formation are typical of rifts (e.g., Goodfellow et al., 1995) or continental arc rifts (e.g., van Staal et al., 1991; Shinjo et al., 1999), and their petrogenesis can assist in critically evaluating tectonic models and deciphering mechanisms of magma generation. Key parameters such as depth of melting, degree of partial melting, mantle source composition, and the role of crustal contamination can be determined by understanding how melt evolved from its origin to crustal emplacement. These parameters are deciphered using whole-rock major and trace element and Nd-Hf isotope geochemical compositions of Menzie Creek Formation rocks, which have been subdivided into three groups based on Th-Nb-La systematics. Most of the Group I rocks are unaltered alkali basalts with LREE enrichment, steep negative slopes, and positive Nb anomalies on multi-element plots (Fig. 11). Groups II and III have similar LREE enrichment and steep negative slops on multi-element plots but have flat and negative Nb anomalies (that result from higher Th values), respectively (Fig. 11).

The LREE enrichment of the Menzie Creek Formation rocks is typical of OIBs and other continental margin volcanic rocks that are generated by the low-degree partial melting of incompatible element-enriched mantle sources

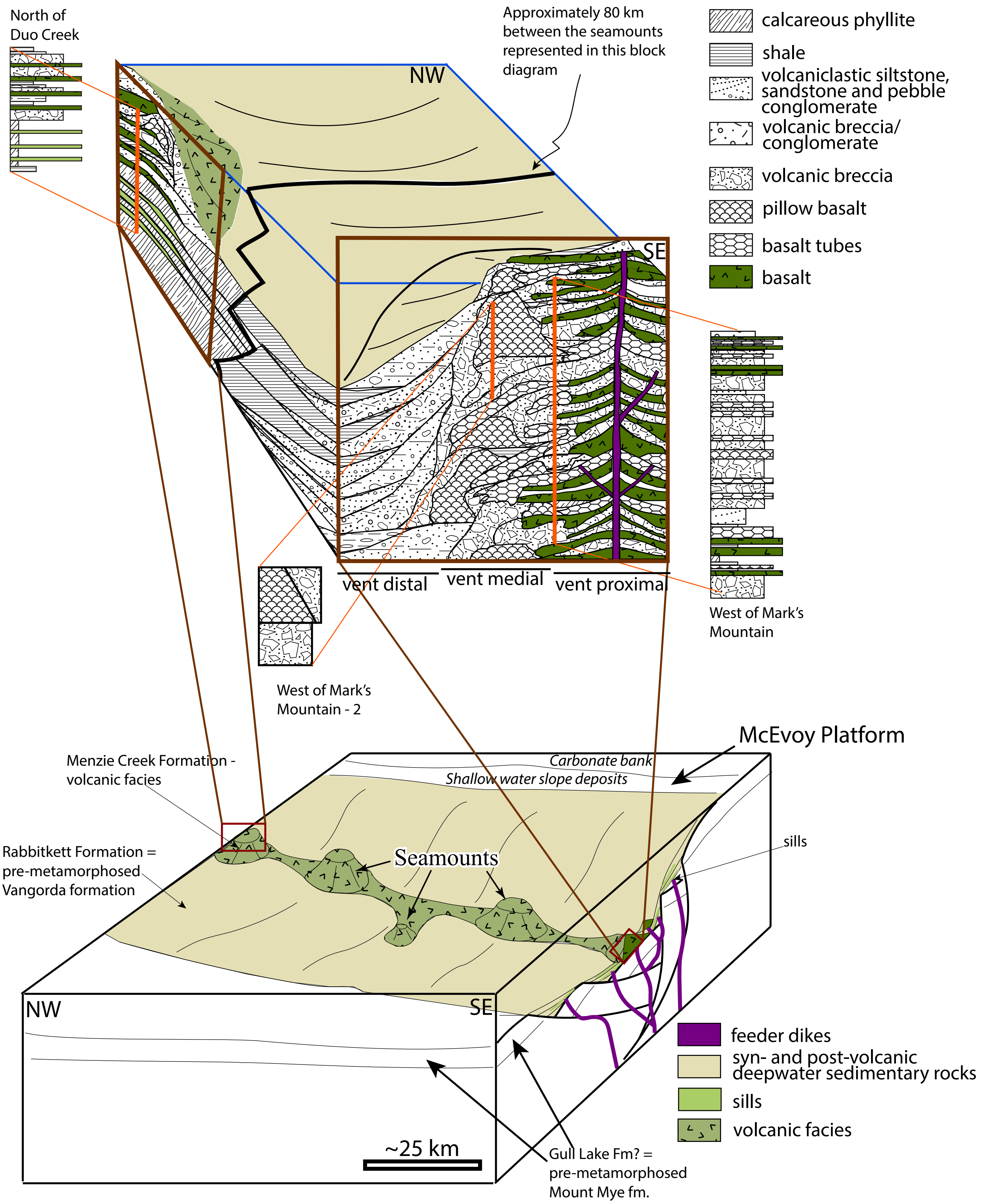

Figure 14. Interpreted depositional environment of Menzie Creek Formation volcanic rocks and sill-sediment complexes. Upper block diagram shows volcanic facies and their relative proximity to vents. Near-vent facies include basalt flows, which give way to basalt tubes further from the vent and to pillows even further as the flow rate wanes. Hyaloclastite breccia can occur in both vent-proximal and vent-medial areas. Pillow breccia is considered a vent-medial facies. Volcanic conglomerate and volcaniclastic rocks are vent distal and are interpreted to result from collapse of over-steepened parts of the volcanic pile and/or from weathering of subaerial parts of the seamount. Lower block diagram shows seamounts aligned parallel to growth faults within the central part of a graben. Seamounts are fed by a fissure that opens in response to faulting. Vents that occur closer to the graben shoulders result in sill emplacement because the sedimentation rate is higher in these areas than in the center of the basin, where magma erupts onto the surface.

(e.g., Kay and Gast, 1973; Rogers, 2015). Enriched mantle sources include asthenosphere associated with plumes and lithospheric mantle (e.g., McDonough, 1990). The volcanic rocks of the Menzie Creek Formation are probably not sourced from a plume, because the volume of magma is small compared to the volume of known plume-related magmatic events, which often result in thousands of square kilometers of magma (e.g., White and McKenzie, 1995). Given the uncertain nature of outboard (seaward) rocks, the Menzie Creek Formation could have formed on the periphery of a plume; however, this possibility is speculative and does not fit with any of the available data except for the geochemical compositions of volcanic units. Lithospheric mantle can be enriched in incompatible elements in several ways, providing alternative explanations for the plume-like geochemical signatures, including: (1) the percolation of low-degree partial melts that originate in the low-velocity zone between the lithosphere and asthenosphere (Humphreys and Niu, 2009); (2) "plums" or streaks within the mantle that are left behind from previous melt events (e.g., Fitton and Dunlop, 1985; Piercey et al., 2012); and (3) metasomatization of the subcontinental lithospheric mantle (SCLM; Hawkesworth et al., 1990; Gallagher and Hawkesworth, 1992; Roex et al., 2001). The lithospheric mantle is fused to the continents and therefore cannot be recycled into the asthenosphere or diluted by mixing with the depleted mantle and hence retains its LREE and incompatible element enrichment (e.g., Arndt et al., 2009).

The lithospheric mantle beneath the Laurentian craton is interpreted to have been fertilized since the Proterozoic (e.g., Milton et al., 2017). For example, Proterozoic plume-related magmatism beneath ancestral North America may have enriched the SCLM through the ponding magma or stalled melts (Piercey et al., 2006). New whole-rock Nd-Hf isotope results of the Menzie Creek Formation overlap with those of Ordovician igneous rocks along the Cordilleran margin that were derived from the lithospheric mantle (εNd_t between –4.2 and +7.8; εHf_t between –9.8 and +10.5; Piercey et al., 2002, 2012; Piercey and Colpron, 2009; Campbell et al., 2019). For example, Kechika group volcanic rocks in eastern Yukon have εNd_{480} values that range from +2.0 to +5.5, and εHf_{480} values that range from +2.9 to +6.6, and plutonic rocks that have εNd_{480} from –4.2 to +1.0, and εHf_{480} values that range from –9.8 to +0.6 (Fig. 13; Campbell et al., 2019). Kechika group rocks were sourced from incompatible element-enriched lithospheric mantle with variable contamination by the continental crust (Campbell et al., 2019), similar to the Menzie Creek Formation rocks. Further examples include alkaline mafic rocks of the Yukon-Tanana terrane that have εNd_{350} = +1.1 and –2.8 (that are interpreted to be contaminated by continental crust; Piercey et al., 2002); the Snowcap assemblage, which is the basement to the Yukon Tanana terrane and has εNd_{360} = +5.5 to +7.8 and εHf_{360} = +6.7 to +10.5 (Fig. 13; Piercey and Colpron, 2009); and oceanic-island basalt from the Lower Permian Campbell Range formation (Slide Mountain terrane) that yields εNd_{275} = +2.2 and +8.9 (Piercey et al., 2012).

During low-degree partial melting, highly incompatible elements preferentially partition into the melt relative to the source region, and they are not subsequently diluted by higher melt fractions. Decompression melting that is the result of lithospheric stretching and thinning initially produces alkali basalts, whereas tholeiitic compositions later dominate as the asthenosphere rises beneath the thinned lithosphere and facilitates a higher degree of melting at shallower depths (e.g., Perry et al., 1987; McKenzie and Bickle, 1988; Gallagher and Hawkesworth, 1992; Peate and Hawkesworth, 1996; Pearce, 2008). There is no evidence for high-degree partial melts of asthenospheric sources, such as basalt with E-MORB signatures nor large volumes of magma, in the Menzie Creek Formation (Figs. 11 and 12). Melting processes that initiate at deeper mantle levels beneath thick lithosphere are consistent with low-degree partial melting and low volumes of magma (Humphreys and Niu, 2009).

The trace element concentrations of Menzie Creek Formation mafic rocks indicate that the melts initiated in a part of the mantle where both garnet and amphibole were present. Heavy REE depletion compared to LREE depletion is a distinct geochemical characteristic of Menzie Creek Formation rocks (Fig. 11) and along with the high Ti/Yb values (Fig. 12D) reflect partitioning of HREE into garnet, which is the stable aluminous phase in the mantle below ~75 km (Ellam, 1992; Roex et al., 2001; Pearce, 2008, 2014). Elevated concentrations of Hf and Zr compared to those of Sm are additional geochemical features that place depth constraints on the melts. Amphibole more strongly retains Sm over Hf and Zr, resulting in higher Sm/Zr and Sm/Hf ratios in amphibole (Foley et al., 2002). During partial melting of amphibole-bearing mantle, where amphibole remains in the restite, the melts have high Zr/Sm and Hf/Sm ratios similar to the geochemical composition of the Menzie Creek Formation. The only other way to get these ratios is to have amphibole as a fractionating phase during emplacement. The Menzie Creek Formation rocks are pyroxene-bearing, which suggests that amphibole was not a fractionating phase during emplacement because amphibole would fractionate later than pyroxene. Gallagher and Hawkesworth (1992) showed that a small amount of fluid added to the base of thick SCLM can alter pyroxene to amphibole. Furthermore, the xenoliths found within alkaline volcanic rocks that erupted onto continents contain hydrated minerals such as amphibole and phlogopite that are evidence of SCLM metasomatism (e.g., Hawkesworth et al., 1990). Amphibole is not stable below a depth of ~100 km (Wallace and Green, 1991; Mandler and Grove, 2016). Based on the Zr-Sm and Hf-Sm systematics and HREE depletion, which require both garnet and amphibole to be present in the restite of the melts, we suggest that amphibole and garnet co-existed in the residue, and this restricts the melting depth for the Menzie Creek Formation rocks to 75–100 km.

The Th-Nb-La variation of groups II and III, compared to that of Group I, primarily reflects Th enrichment (Fig. 12B) and is related to: (1) crustal contamination during magma ascent or seafloor emplacement; or (2) mantle metasomatism related to subduction processes (the addition of water-soluble elements such as Th to the mantle prior to partial melting; e.g., Pearce and Peate, 1995). There is no evidence that subduction processes were active during the formation of the Menzie Creek Formation, such as the occurrence of spatially associated subalkaline arc rocks (Fig. 10). Therefore, the negative Nb anomalies (or higher values of Th) observed in groups II and III are interpreted to reflect continental crustal contamination. This is supported by the Nb/U values of Group II and Group III rocks that trend away from those of oceanic basalt and toward values common to continental crust (Fig. S5, see footnote 1). Similarly, La/Sm and Zr compared to Th/Nb also show that groups II and III trend toward values common to continental crust (Figs. 12B and 12C; e.g., Piercey et al., 2002), albeit with Group III rocks exhibiting a greater degree of contamination than those of Group II.

Crustal influences are also supported by the Nd-Hf isotope compositions of Menzie Creek Formation rocks. For example, Group III samples have lower εHf_{484} values and lower εNd_{484} values than Group I rocks (Group II was not sampled for isotopic analysis; Fig. 13). The εHf_{484} and εNd_{484} values of Group I rocks are also lower than those for the depleted mantle at 484 Ma (εNd_{484} = +9.3; εHf_{484} = +13.99; Vervoort and Blichert-Toft, 1999; Hamilton et al., 1983). These are similar to the compositions of continental rift rocks derived from enriched mantle domains (e.g., Perry et al., 1987). The lower values found in Group III, however, are not consistent with derivation solely from enriched mantle and require the influence of a more evolved source. It is notable that the lower εNd_{484} values trend toward the values of northern Cordilleran passive margin strata that range from –5 to –10 (Garzione et al., 1997), and these rocks have a depleted mantle model age T_{DM}(Nd) of 1.3 Ga and T_{DM}(Hf) of 1.05–1.08 Ga (Goldstein et al., 1984), which are both consistent with the Menzie Creek Formation magmas having interacted with passive margin sediment and/or a source with evolved isotopic characteristics upon emplacement.

Structural Controls on the Location of Seamount Complexes in Central Yukon

Sedimentary rocks that both underlie and overlie the Menzie Creek Formation are generally interpreted to be offshelf facies deposited along a passive margin following crustal thinning related to rifting (e.g., Gordey and Anderson, 1993). Extensional faults associated with crustal thinning are not readily recognized because of overprinting by Mesozoic contractional deformation, but there is evidence that the Twopete fault originated as a growth fault during the Ordovician (Cobbett, 2019). Cambrian to Ordovician strata mapped within a fault-bounded block (MEP in Figs. 1 and 3) adjacent to the Twopete fault comprise cross-bedded sandstone with ripple marks that suggest shallow-water deposition (Cobbett, 2019), whereas coeval units of shale and chert mapped northeast of the fault in the Selwyn basin are consistent with deep-water deposition (Road River Group; Gordey and Anderson, 1993). One explanation for this difference is that the Twopete fault traces an ancient platform (McEvoy platform in Fig. 1) to basin transition and originated as a growth fault. The fault facilitated deepening to its southwest into a local graben that hosted the Menzie Creek seamounts (Figs. 1C and 14). A margin-parallel graben that developed in response to extension and related growth faults would explain the interfingering of Menzie Creek Formation basalt with Road River Group shale units near the edges of the basaltic edifices. This structural configuration also supports the evidence for the emplacement of sills in some areas and the eruption of lava in other areas. Sill emplacement may have occurred near the edges of a graben where sedimentation rates were higher, whereas near the graben center, lower sedimentation rates accommodated volcanic eruption (Fig. 14; Einsele, 1985).

Timing and Significance of Post-Rift Ordovician Magmatism in Yukon and Greater Cordilleran Margin System

The high-precision zircon U-Pb dates of Menzie Creek Formation rock units are interpreted to represent the timing of seafloor eruption and seamount construction at ca. 484 Ma. The zircon grains dated are likely igneous, based on their faceted shapes, chemical compositions, zoning, and lack of inherited cores. The uniformity of the zircons suggests that the grains are syn-magmatic and not xenocrystic (e.g., sourced and recycled Proterozoic grains from nearby sedimentary strata; McMechan et al., 2017). The dates broadly coincide with fossil ages from carbonate lenses within the basaltic rocks of the Menzie Creek Formation (Pigage, 2004) and allow for better correlation with other magmatic and tectonic events along western Laurentia.

The high-precision U-Pb date from the Crow Formation pebbly sandstone is interpreted to represent the ca. 486 Ma eruption age of nearby volcanic rocks. The quartz grains within the sample suggest that early eruptions may have been more felsic or bimodal. Alternatively, the quartz grains could be sourced from underling strata, but in this scenario Proterozoic zircon grains should also occur in the sample, and these are notably absent in Crow Formation sandstone from this location (Table S1).

Studies of lower Paleozoic volcanic rocks along the western Laurentian margin indicate that post-rift magmatism occurred in separate, episodic events during the Late Cambrian, Early Ordovician, and Late Ordovician (Larson et al., 1985; Leslie, 2009; Pigage et al., 2012; MacNaughton et al., 2016; Campbell et al., 2019; Cobbett, 2020). The Menzie Creek and Crow formations in southeast Yukon document part of the Early Ordovician pulse of magmatism in the northern Canadian Cordillera. This event is regionally widespread in southern Yukon and includes alkali basalt and gabbro in the Upper Cambrian to Lower Ordovician Kechika group with U-Pb dates of between 488 Ma and 483 Ma (Campbell et al., 2019), a felsic volcanic rock associated with the alkaline VMS Matt Berry deposit that is dated at 486.69 ± 0.15 Ma (Fonseca, 2001; Yukon Geological Survey, 2022; D. Moynihan, 2018, personal commun.), and 491.04 ± 0.13 Ma rhyolite tuff in the Crow Formation (Fig. 1B; Pigage et al., 2012, 2015). In addition to Early Ordovician magmatism in Yukon, broadly coeval 497–486 Ma alkaline magmatism occurred in central Idaho to the north of the Snake River transfer zone and adjacent to the Lemhi Arch (Lund et al., 2010). Some of these dates are within error of the interpreted age of the Menzie Creek Formation (and several are both older and younger), which suggests that magmatism in the Cassiar terrane of Yukon and in Idaho is synchronous with the eruption of the Menzie Creek seamounts and documents a margin-scale magmatic event that must be considered when reconstructing the Late Cambrian to Early Ordovician evolution of the western Laurentian margin. Younger

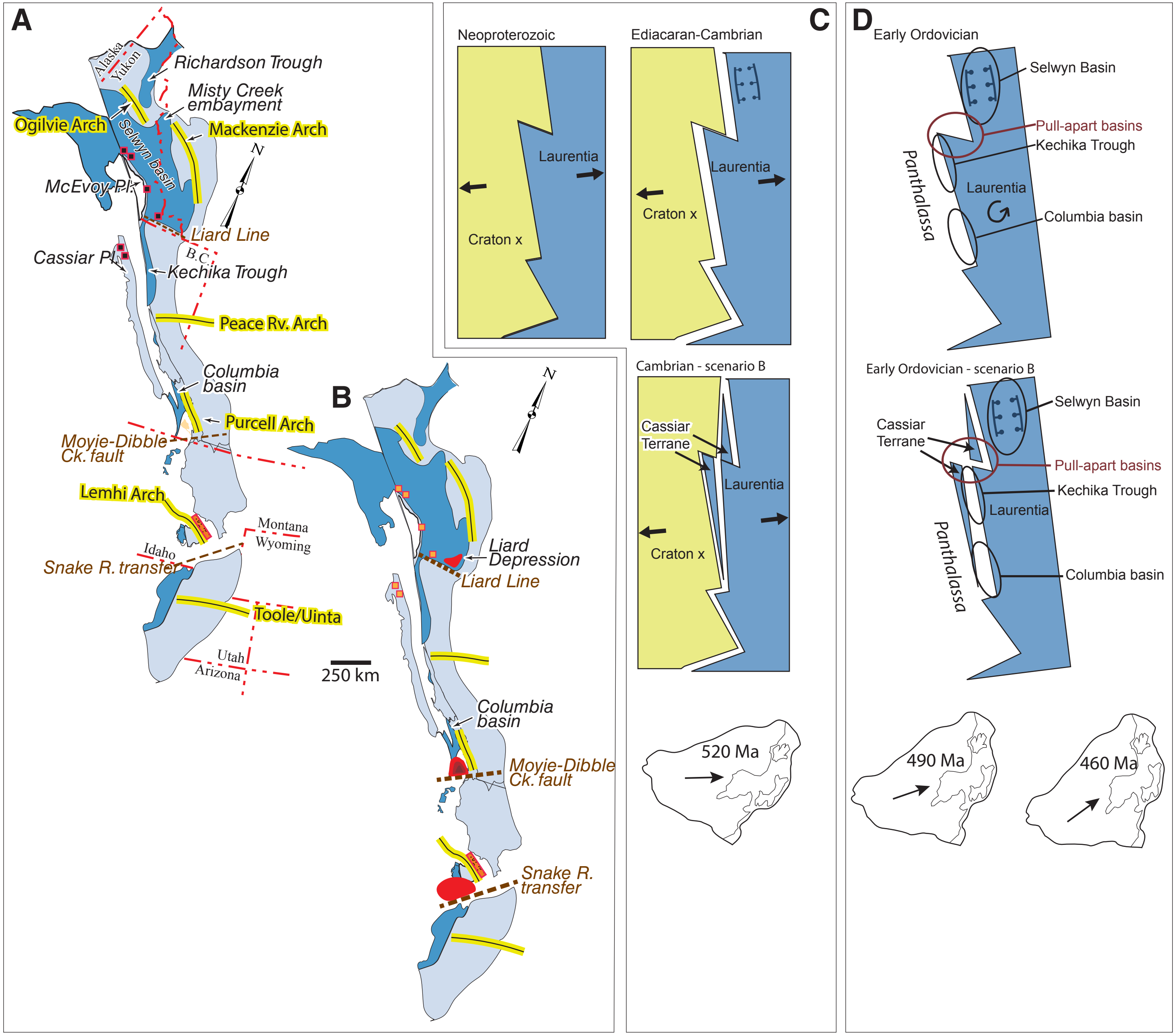

Figure 15. (A) Western Laurentian margin with major Cretaceous and Eocene faults restored based on Figures 3 and 4 of Wyld et al. (2006). Restoration includes reversing Basin and Range extension, rotation of the Blue Mountains province, shortening in the Sevier fold-and-thrust belt, and strike-slip motion on the Tintina–northern Rocky Mountain Trench faults. The Selwyn basin would have been wider in the Cambrian and Ordovician because it was affected by Mesozoic folding and thrusting; however, limited data preclude an estimate of the amount of shortening, and therefore it has not been modified. Early Paleozoic arches are traced with yellow lines, and transfer faults are shown by dark brown dashed lines. Orange squares show the approximate location of Early Ordovician magmatism. (B) Simplified version of the map shows relative thickness (darker red colors represent thicker basin fill) of sedimentary cover in areas proposed to be pull-apart basins that occur north of transfer faults. Orange squares show the approximate location of Early Ordovician magmatism. (C) Rifting of craton X away from Laurentia in the Cambrian. (D) Counterclockwise rotation of Laurentia is shown by the orientation of North America at the bottom (Cocks and Torsvik, 2011). Resulting rift geometries show that transfer faults open as pull-apart basins. The rotation provides an explanation for the diachronous rift, with older breakup ages in the southern Cordillera than in the north. Scenario B shows a margin-parallel block separating from the main Laurentian craton during or after rifting, which eventually becomes the Cassiar terrane. Pl.—Platform, Rv.—River, Ck.—Creek.

magmatism that is less precisely dated may also need to be considered when reconstructing the Early Ordovician margin. For example, Middle Ordovician seamounts are preserved in continental margin strata in Nevada (Watkins and Browne, 1989). Although no precise radiometric ages have been reported, the basaltic rocks are constrained by fossils to be Lower and Middle Ordovician.

A regional sub-Jiangshanian (ca. 500 Ma) unconformity has been proposed as the base of the passive continental margin succession in the northern Canadian Cordillera (Moynihan et al., 2019), which implies a post-rift tectonic setting for volcanism in the Menzie Creek Formation and extension along the Twopete fault system in central Yukon. The mechanism for post-rift magma generation remains unclear. The small volume of magma argues against a plume origin, and there is geochemical and isotopic evidence for deep melting of the lithospheric mantle. Thick lithosphere shortens the height of the melting column and inhibits shallow mantle melting at low pressures (Humphreys and Niu, 2009), which is consistent with the composition and low volume of the Menzie Creek Formation rocks. It is plausible that thinning-related decompression melting drove Early Ordovician magmatism, but the mechanism for post-rift lithospheric thinning in the necking or proximal domain of the rifted margin requires explanation. An overview of the paleogeography along the western Laurentian margin is important for predicting viable mechanisms for post-rift magmatism. Deep basins with anomalously thick sediment can be interpreted as areas that underwent lithospheric thinning prior to basin development. Similarly, high-standing blocks subject to erosion or carbonate deposition are interpreted as areas that did not undergo as much crustal extension (e.g., Fig. 1C).

Implications for Western Laurentian Rift to Post-Rift Evolution and Late Cambrian to Early Ordovician Paleogeography

Three models for post-rift magmatism that are variably consistent with the known paleogeography along the western Laurentian margin are: (1) magmatism linked to leaky transfer faults (e.g., Campbell et al., 2019); (2) a late-stage secondary rift (e.g., Peron-Pinvidic et al., 2013); and (3) mantle perturbations that cause small volume decompression melting after breakup (e.g., Peron-Pinvidic et al., 2010). After a discussion of these three models, we propose two new scenarios that build on these ideas and better account for the timing and geologic setting of the Menzie Creek Formation.

Lower Paleozoic continental margin strata from northwestern Canada to the southwestern USA form a stepped or zigzag pattern in which platform and basin facies are offset across lineaments or faults that range from margin-perpendicular to oblique (see Cecile et al., 1997; Lund, 2008). In southeast Yukon, the platformal margin is offset dextrally along the Liard Line, a lineament that has been identified as a rift-related transfer fault that may have locally controlled early Paleozoic magmatism (e.g., Fritz et al., 1991; Hayward, 2015; Campbell et al., 2019). North of this lineament, the Liard Depression represents an anomalous thickness of Lower Ordovician and younger rocks (Cecile et al., 1997). South of the Liard Line, the preserved parts of the continental margin are narrower and less completely preserved, but several notable features include the Peace River, Purcell, Lemhi, and Toole/Uinta arches. The Peace River Arch was a northeast-trending, high-standing block from the Cambrian until the Silurian (Norford, 1990) and was probably controlled by basement structures associated with the development of the Laurentian craton (e.g., O'Connell et al., 1990). The northwest-trending Purcell Arch parallels the Columbia basin in southern British Columbia and lower Paleozoic mafic volcanic rocks that have both mid-oceanic-ridge basalt, and oceanic-island basalt-like geochemical compositions occur to the west (Logan and Colpron, 2006). Another dextral offset in platformal strata occurs where the Moyie-Dibble Creek fault system follows the trace of an early Paleozoic, down-to-the-northwest structure that facilitated the deposition of ~7 km of sediment (Price and Sears, 2000). In this area, Late Cambrian to Early Ordovician alkalic igneous rocks occur near the eastern end of the fault system (see Lund et al., 2010). The Lemhi Arch is oriented similarly to the Purcell Arch in Idaho, where lower Paleozoic igneous rocks that are coeval with the Menzie Creek Formation occur along its western edge (Lund et al., 2010). The Snake River transfer fault, where continental margin facies are also offset dextrally, is a structure that delineates a belt of slope-facies strata that strikes northeast and deepens to the north (Poole et al., 1992; Lund, 2008). Lastly, the Toole/Uinta Arch was a prominent high-standing feature in the early Paleozoic that trends roughly east–west (Poole et al., 1992). Notably, anomalous post-Early Ordovician subsidence occurred to the north and northwest of each of the margin-perpendicular lineaments or transfer faults. It is possible that pull-apart basins opened up along these transfer faults as extension proceeded, which suggests that the margin underwent northwest–southeast transtension. The pull-apart basin would have formed from crustal- to lithospheric-scale thinning and resulted in a large net subsidence following extension (Fig. 15).

Campbell et al. (2019) explored the possibility that Late Cambrian to Silurian post-rift magmatism in the Cassiar terrane of south-central Yukon was spatially related to the Liard Line. Similar post-rift seamounts are located near transfer faults or fracture zones along the modern Newfoundland rift margin, and magmas used these crustal breaks to migrate to the surface (e.g., Pe-Piper et al., 1994; Keen et al., 2014). The timing of magmatism broadly overlaps the Menzie Creek Formation rocks and those in the Cassiar terrane; however, after restoration of Eocene faults there is an absence of nearby lineaments, such as the Liard Line, to explain the Menzie Creek Formation volcanism (Fig. 15B).

Margin-parallel detachment faults responsible for crustal thinning have been documented in the proximal domains of modern rifts (e.g., Newfoundland-Iberia) and could provide a mechanism for Menzie Creek Formation magmatism. Peron-Pinvidic et al. (2013) showed an aborted V-shaped basin that formed during rifting along the Iberia margin. This basin is associated with lithospheric thinning and provides a mechanism for small-volume magmatism (e.g., McKenzie and Bickle, 1988). Thicker crust would be analogous to the McEvoy platform, similar to the configuration proposed by Beranek (2017) for the Cassiar platform–Kechika trough portion of the margin (Fig. 1C; Peron-Pinvidic et al., 2013, their fig. 4). The main problem with this comparison is that the formation of the aborted basin along the Newfoundland-Iberia margins is considered a syn-rift feature, and the Menzie Creek Formation seamounts formed during the drift stage (Peron-Pinvidic et al., 2013; Moynihan et al., 2019). Thomas (2014) argued that ductile extension of the mantle lithosphere can transmit extensional forces into the upper brittle crust that lead to the development of intracratonic basins that can occur after breakup, be filled with mantle-derived lava, and have anomalously thick post-rift sedimentary fill, similar to what is proposed here for the Menzie Creek Formation.

Off-axis, post-rift alkaline magmatism has been documented along the Newfoundland-Iberia margins and is explained by: (1) the release of in-plane tensile stresses resulting in extension and decompression melting after breakup (Jagoutz et al., 2007); and (2) convection cells or thermal anomalies that persist in the mantle after breakup (Peron-Pinvidic et al., 2010). If fertile streaks in the mantle coincided with a mantle perturbation, it is possible that it would induce small-volume alkaline melts. There is good evidence that breakup in the U.S. Cordillera occurred earlier than in the north, and this difference should be reflected in the post-rift magmatism if it is linked to stress release associated with lithospheric rupture (e.g., Colpron et al., 2002; Keller et al., 2012; Yonkee et al., 2014; Moynihan et al., 2019). Early Ordovician magmatism is well constrained between 491 Ma and 473 Ma from Idaho to central Yukon, and given the uncertainties associated with the age of breakup, this model possibly explains the post-rift magmatism.

We propose new plate tectonic scenarios that provide alternative explanations for the post-rift magmatism found along the western Laurentian margin during the Late Cambrian to Early Ordovician. The first hypothesis for Early Ordovician plate-scale magmatism features extension and partial separation of a continental fragment off the western Laurentian margin after continental breakup (Figs. 15C and 15D; scenario B). Cawood et al. (2001) proposed such a model for the eastern Laurentian margin during the early Paleozoic to account for two pulses of rift-related magmatism prior to thermal subsidence and passive margin development. The Menzie Creek Formation could represent a later pulse of magmatism associated with an extensional event that included a crustal block moving away from northern Laurentia after the successful breakup of Rodinia at ca. 500 Ma (Moynihan et al., 2019). The McEvoy platform and its southern extension, the Cassiar terrane (Fig. 1), is a possible candidate for this fragment along western Laurentia because it is a fault-bounded, carbonate-dominated block of North American affinity that is situated to the west (outboard) of the Selwyn basin and Menzie Creek Formation volcanic rocks. In this model, lithospheric extension and related thinning inboard of the Panthalassa mid-oceanic ridge facilitated decompression melting and the eruption of the Menzie Creek Formation into a margin-parallel graben. The driving force that would cause extension after the successful breakup of Rodinia is uncertain; however, as discussed in the previous section, ductile mantle flow may exert extensional forces on the crust even after breakup, and this would provide a driving force for multiple rifts (e.g., Thomas, 2014). A likely scenario for the formation of the Menzie Creek Formation seamounts is that they formed in an offshore basin associated with margin-parallel growth faults that were activated by the transfer of extensional strain either through ductile shear in the mantle or via transtensional margin-scale kinematics, or both.

A second hypothesis works in conjunction with published depth-dependent rift models that segment the margin into upper- and lower-plate segments, but adds a component of rotation that may explain the origin of several paleogeographic features and post-rift magmatism. In the present-day Gulf of California, highly oblique extension facilitates the long-lived transition from continental rifting to seafloor spreading (Fletcher and Munguia, 2000; Bennett and Oskin, 2014). Along segments of the margin where strike-slip motion dominates, the plates are coupled and allow the transfer of stresses inboard through the upper crust. This model provides an explanation for modern magmatism in the proximal domain (close to continent, i.e., Sierra Madre Occidental; Henry and Aranda-Gomez, 1992) that is occurring contemporaneous with seafloor spreading elsewhere. In our model, the Lower Ordovician volcanic rocks along western Laurentia (i.e., Menzie Creek Formation in Yukon) would have formed inboard of crustal-scale, margin-parallel, strike-slip faults (Figs. 15C and 15D). Mid-oceanic-ridge–like, lower Paleozoic igneous rocks linked to rifting have also been identified in southeast British Columbia to the west of the Purcell Arch and may represent a localized area of seafloor spreading (Logan and Colpron, 2006). Paleomagnetic data indicate that the Laurentian craton rotated ~25° counterclockwise between 520 Ma and 460 Ma (Cocks and Torsvik, 2011), which could have induced transtensional kinematics along the margin during and after rifting (Fig. 15C), assuming that Panthalassa is relatively fixed with respect to western Laurentia. Existing transfer faults in this scenario would have been under extension, and this provides an explanation for the anomalous post-rift subsidence that is documented north of most of these faults (e.g., Liard Depression; Fig. 15B).

The combination of the geochronology, geochemistry, and stratigraphy of magmatic rocks associated with rifting and post-rift passive margin development provides essential information for deciphering the evolution of ancient rifts and subsequent passive margins and adds to our knowledge of global tectonics.

CONCLUSIONS

The facies and distribution of the Menzie Creek Formation rocks suggests they represent partially preserved seamounts. Several kilometers of basaltic rocks dominated by pillow basalt and hyaloclastite breccia occur in one section with almost no interbedded sedimentary rocks. The seamounts developed in a graben that was offshelf of the western Laurentian platform. Basaltic volcanism occurred along the center of the graben, where sedimentation rates were relatively low. Magma was emplaced as sills closer to the edges of the graben, where sedimentation rates were higher.

The eruption age of the Menzie Creek Formation is ca. 484 Ma based on two U-Pb zircon ages from volcaniclastic rocks within the seamount edifices. Coeval magmatism is documented in the Crow Formation of southeast Yukon, where a single sample of volcanogenic pebbly sandstone yielded a U-Pb zircon age of ca. 486 Ma, and at various localities in southeast Yukon and in Idaho.

The whole-rock geochemical signatures of Menzie Creek Formation rocks require low-degree partial melting of an enriched mantle source. Trace element compositions imply that this source was metasomatized subcontinental lithospheric mantle (SCLM). The alkaline nature of Menzie Creek Formation rocks suggests that magmatism was produced from moderate amounts of lithospheric stretching and thinning and did not induce melt input from the asthenosphere. If the source for the Menzie Creek Formation rocks were the SCLM, then the thickness of the lithosphere along the Laurentian margin during the Early Ordovician would have been 75–100 km.

Menzie Creek Formation volcanic rocks are alkali basalts with OIB-like geochemical affinities. A subset of these rocks with negative Nb anomalies (compared to Th and La) was contaminated by continental crust upon emplacement into seafloor sediments or by wallrock during ascent. The lower εNd_{484} and εHf_{484} values of Group III rocks is consistent with contamination by continent-derived, passive margin strata.

Two new plate tectonic scenarios are proposed to account for post-rift magmatism along the western Laurentian margin: (1) a secondary crustal block rifting off the northern part of the margin after breakup, and (2) transtensional margin-scale kinematics. In the first scenario, stress is exerted on the crust by mantle flow, driving a secondary rift event that accounts for basin development and post-rift magmatism. In the second scenario, counterclockwise rotation of Laurentia is the driving force for a prolonged breakup during which the margin is partitioned into strike-slip and extensional domains. Along strike-slip portions, stresses are transferred inboard of the ridge axes, which allows extension and magmatism in the proximal rift domain after breakup.

ACKNOWLEDGMENTS

We thank Dominique Weis (Pacific Centre for Isotopic and Geochemical Research at the University of British Columbia) for performing the Nd and Hf isotopic analyses. Comments and suggestions by Associate Editor Nancy Riggs, Adolph Yonkee, and an anonymous reviewer improved the manuscript and are gratefully acknowledged. This project was supported by the Yukon Geological Survey and Natural Sciences and Engineering Research Council of Canada (NSERC) Discovery Grants to Luke Beranek and Stephen Piercey. This is Yukon Geological Survey contribution 063.

REFERENCES CITED

Abbott, G., 1997, Geology of the Upper Hart River area, Eastern Ogilvie Mountains, Yukon Territory (116A/10, 116A/11): Exploration and Geological Services Division, Yukon, Indian and Northern Affairs Canada, Bulletin 9, 92 p.

Alves, T.M., and Cunha, T.A., 2018, A phase of transient subsidence, sediment bypass and deposition of regressive–transgressive cycles during the breakup of Iberia and Newfoundland: Earth and Planetary Science Letters, v. 484, p. 168–183, https://doi.org/10.1016/j.epsl.2017.11.054.

Arndt, N., Coltice, N., Helmstaedt, H., and Gregoire, M., 2009, Origin of Archean subcontinental lithospheric mantle: Some petrological constraints: Lithos, v. 109, no. 1–2, p. 61–71, https://doi.org/10.1016/j.lithos.2008.10.019.

Bennett, S.E., and Oskin, M.E., 2014, Oblique rifting ruptures continents: Example from the Gulf of California shear zone: Geology, v. 42, no. 3, p. 215–218, https://doi.org/10.1130/G34904.1.

Beranek, L.P., 2017, A magma-poor rift model for the Cordilleran margin of western North America: Geology, v. 45, no. 12, p. 1115–1118, https://doi.org/10.1130/G39265.1.

Blichert-Toft, J., and Albarède, F., 1997, The Lu-Hf isotope geochemistry of chondrites and the evolution of the mantle-crust system: Earth and Planetary Science Letters, v. 148, p. 243–258, https://doi.org/10.1016/S0012-821X(97)00040-X.

Bond, G., and Kominz, M.A., 1984, Construction of tectonic subsidence curves for the early Paleozoic miogeocline, southern Canadian Rocky Mountains: Implications for subsidence mechanisms, age of breakup and crustal thinning: Geological Society of America Bulletin, v. 95, p. 155–173, https://doi.org/10.1130/0016-7606(1984)95<155:COTSCF>2.0.CO;2.

Bond, G.C., Christie-Blick, N., Kominz, M.A., and Devlin, W.J., 1985, An Early Cambrian rift to post-rift transition in the Cordillera of western North America: Nature, v. 315, p. 742–746, https://doi.org/10.1038/315742a0.

Bouvier, A., Vervoort, J.D., and Patchett, P.J., 2008, The Lu–Hf and Sm–Nd isotopic composition of CHUR: Constraints from unequilibrated chondrites and implications for the bulk composition of terrestrial planets: Earth and Planetary Science Letters, v. 273, no. 1–2, p. 48–57, https://doi.org/10.1016/j.epsl.2008.06.010.

Brenan, J.M., Shaw, H.F., Ryerson, F.J., and Phinney, D.L., 1995, Mineral-aqueous fluid partitioning of trace elements at 900°C and 2.0 GPa: Constraints on the trace element chemistry of mantle and deep crustal fluids: Geochimica et Cosmochimica Acta, v. 59, no. 16, p. 3331–3350, https://doi.org/10.1016/0016-7037(95)00215-L.

Campbell, R.W., Beranek, L.P., Piercey, S.J., and Friedman, R., 2019, Early Paleozoic post-breakup magmatism along the Cordilleran margin of western North America: New zircon U-Pb age and whole-rock Nd-and Hf-isotope and lithogeochemical results from the Kechika group, Yukon, Canada: Geosphere, v. 15, p. 1262–1290, https://doi.org/10.1130/GES02044.1.

Cawood, P.A., McCausland, P.J., and Dunning, G.R., 2001, Opening Iapetus: Constraints from the Laurentian margin in Newfoundland: Geological Society of America Bulletin, v. 113, no. 4, p. 443–453, https://doi.org/10.1130/0016-7606(2001)113<0443:OICFTL>2.0.CO;2.

Cecile, M., Morrow, D., and Williams, G., 1997, Early Paleozoic (Cambrian to Early Devonian) tectonic framework, Canadian Cordillera: Bulletin of Canadian Petroleum Geology, v. 45, no. 1, p. 54–74.

Cecile, M.P., 1982, The Lower Paleozoic Misty Creek embayment, Selwyn basin, Yukon and Northwest Territories: Geological Survey of Canada, Bulletin 335, 78 p., https://doi.org/10.4095/111346.

Cobbett, R.N., 2016a, Geological map of the Earn Lake area, central Yukon, parts of NTS 105L/09, 15 and 16: Yukon Geological Survey Open File 2016–1, scale 1:50,000.

Cobbett, R.N., 2016b, Preliminary observations on the geology of the Tay Mountain area (parts of NTS 105K/12 and 13, 105/09 and 16), central Yukon, *in* MacFarlane, K.E., and Nordling, M.G., eds., Yukon Exploration and Geology 2015: Yukon Geological Survey, p. 79–98.

Cobbett, R.N., 2019, Preliminary observations on the geology of northeastern Glenlyon area, central Yukon (parts of NTS 105L/10, 14, 15), *in* MacFarlane, K.E., ed., Yukon Exploration and Geology: Yukon Geological Survey, p. 43–60.

Cobbett, R.N., 2020, Preliminary report on the bedrock geology of Castle Mountain area, Yukon (parts of NTS 105D/6), *in* MacFarlane, K.E., ed., Yukon Exploration and Geology: Yukon Geological Survey, p. 43–55.

Cocks, L.R.M., and Torsvik, T.H., 2011, The Palaeozoic geography of Laurentia and western Laurussia: A stable craton with mobile margins: Earth-Science Reviews, v. 106, no. 1–2, p. 1–51, https://doi.org/10.1016/j.earscirev.2011.01.007.

Colpron, M., Logan, J.M., and Mortensen, J.K., 2002, U-Pb zircon age constraint for late Neoproterozoic rifting and initiation of the lower Paleozoic passive margin of western Laurentia: Canadian Journal of Earth Sciences, v. 39, p. 133–143, https://doi.org/10.1139/e01-069.

Davis, A.S., and Clague, D.A., 2003, Hyaloclastite from Miocene seamounts offshore central California: Compositions, eruption styles, and depositional processes, *in* White, J.D.L., Smellie, J.L., and Clague, D.A., eds., Explosive Subaqueous Volcanism: Washington, D.C., American Geophysical Union, Geophysical Monograph Series, v. 140, p. 129–142.

Einsele, G., 1985, Basaltic sill-sediment complexes in young spreading centers: Genesis and significance: Geology, v. 13, no. 4, p. 249–252, https://doi.org/10.1130/0091-7613(1985)13<249:BSCIYS>2.0.CO;2.

Ellam, R., 1992, Lithospheric thickness as a control on basalt geochemistry: Geology, v. 20, no. 2, p. 153–156, https://doi.org/10.1130/0091-7613(1992)020<0153:LTAACO>2.3.CO;2.

Evans, K.V., and Zartman, R.E., 1988, Early Paleozoic alkalic plutonism in east-central Idaho: Geological Society of America Bulletin, v. 100, no. 12, p. 1981–1987, https://doi.org/10.1130/0016-7606(1988)100<1981:EPAPIE>2.3.CO;2.

Eyster, A., Ferri, F., Schmitz, M.D., and Macdonald, F.A., 2018, One diamictite and two rifts: Stratigraphy and geochronology of the Gataga Mountain of northern British Columbia: American Journal of Science, v. 318, no. 2, p. 167–207, https://doi.org/10.2475/02.2018.1.

Ferri, F., Rees, C.J., Nelson, J.L., and Legun, A.S., 1999, Geology and mineral deposits of the northern Kechika trough between Gataga River and the 60^{th} parallel: British Columbia Ministry of Energy and Mines, Bulletin 107, 113 p.

Fitton, J., and Dunlop, H., 1985, The Cameroon line, West Africa, and its bearing on the origin of oceanic and continental alkali basalt: Earth and Planetary Science Letters, v. 72, no. 1, p. 23–38, https://doi.org/10.1016/0012-821X(85)90114-1.

Fletcher, J.M., and Munguia, L., 2000, Active continental rifting in southern Baja California, Mexico: Implications for plate motion partitioning and the transition to seafloor spreading in the Gulf of California: Tectonics, v. 19, no. 6, p. 1107–1123, https://doi.org/10.1029/1999TC001131.

Foley, S., Tiepolo, M., and Vannucci, R., 2002, Growth of early continental crust controlled by melting of amphibolite in subduction zones: Nature, v. 417, no. 6891, p. 837–840, https://doi.org/10.1038/nature00799.

Fonseca, A., 2001, Felsic metavolcanic rocks at Matt Berry: A new deposit model, *in* Esmond, D.D., and Weston, L.H., eds., Yukon Exploration and Geology 2000: Exploration and Geological Division, Yukon, Indian and Northern Affairs Canada, p. 311–318.

Fouquet, Y., Eissen, J.-P., Ondreas, H., Barriga, F., Batiza, R., and Danyushevsky, L., 1998, Extensive volcaniclastic deposits at the Mid-Atlantic Ridge axis: Results of deep-water basaltic explosive volcanic activity?: Terra Nova, v. 10, no. 5, p. 280–286, https://doi.org/10.1046/j.1365-3121.1998.00204.x.

Fritz, W.H., Cecile, M.P., Norford, B.S., Morrow, D., Geldsetzer, H.H.J., Gabrielse, H., and Yorath, C.J., 1991, Cambrian to Middle Devonian assemblages, *in* Gabrielse, H., and Yorath, C.J., eds., Geology of the Cordilleran Orogen in Canada: Boulder, Colorado, Geological Survey of America, Geology of North America, v. G2, p. 151–218, https://doi.org/10.1130/DNAG-GNA-G2.151.

Gabrielse, H., Blusson, S.L., and Roddick, J., 1973, Geology of Flat River, Glacier Lake, and Wrigley Lake Map-Areas, District of Mackenzie and Yukon Territory: Geological Survey of Canada, Department of Energy, Mines and Resources, Memoir 366, 153 p.

Gabrielse, H., Murphy, D.C., and Mortensen, J.K., 2006, Cretaceous and Cenozoic dextral orogen-parallel displacements, magmatism and paleogeography, north-central Canadian Cordillera, *in* Haggart, J., Enkin, R., and Monger, J.W.H., eds., Paleogeography of North America Cordillera: Evidence for and against Large-Scale Displacements: Geological Association of Canada, Special Paper 46, p. 255–276.

Gallagher, K., and Hawkesworth, C., 1992, Dehydration melting and the generation of continental flood basalts: Nature, v. 358, p. 57–59, https://doi.org/10.1038/358057a0.

Garzione, C.N., Patchett, P.J., Ross, G.M., and Nelson, J., 1997, Provenance of Paleozoic sedimentary rocks in the Canadian Cordilleran miogeocline: A Nd isotopic study: Canadian Journal of Earth Sciences, v. 34, p. 1603–1618, https://doi.org/10.1139/e17-129.

Goldstein, S.L., O'Nions, R.K., and Hamilton, P.J., 1984, A Sm-Nd isotopic study of atmospheric dusts and particulates from major river systems: Earth and Planetary Science Letters, v. 70, no. 2, p. 221–236, https://doi.org/10.1016/0012-821X(84)90007-4.

Goodfellow, W.D., Cecile, M.P., and Leybourne, M.I., 1995, Geochemistry, petrogenesis, and tectonic setting of lower Paleozoic alkalic and potassic volcanic rocks, Northern Canadian Cordillera Miogeocline: Canadian Journal of Earth Sciences, v. 32, p. 1236–1254, https://doi.org/10.1139/e95-101.

Gordey, S.P., 2013, Evolution of the Selwyn basin region, Sheldon Lake (105J) and Tay River (105K) map areas, central Yukon Territory: Geological Survey of Canada, Bulletin 599, 190 p., https://doi.org/10.4095/293034.

Gordey, S.P., and Anderson, R.G., 1993, Evolution of the Northern Cordilleran Miogeocline, Nahanni Map Area (105I), Yukon and Northwest Territories: Geological Survey of Canada Memoir 428, 214 p., https://doi.org/10.4095/183983.

Green, L.H., 1972, Geology of Nash Creek, Larsen Creek, and Dawson Map Areas, Yukon Territory: Geological Survey of Canada Memoir 364, 157 p., https://doi.org/10.4095/100697.

Hamilton, P.J., O'Nions, R.K., Bridgwater, D., and Nutman, A., 1983, Sm-Nd studies of Archaean metasediments and metavolcanics from West Greenland and their implications for the Earth's early history: Earth and Planetary Science Letters, v. 62, p. 263–272, https://doi.org/10.1016/0012-821X(83)90089-4.

Hansen, V.L., Goodge, J.W., Keep, M., and Oliver, D.H., 1993, Asymmetric rift interpretation of the western North American margin: Geology, v. 21, p. 1067–1070, https://doi.org/10.1130/0091-7613(1993)021<1067:ARIOTW>2.3.CO;2.

Hawkesworth, C., Kempton, P., Rogers, N., Ellam, R., and Van Calsteren, P., 1990, Continental mantle lithosphere, and shallow level enrichment processes: Earth and Planetary Science Letters, v. 96, p. 256–268, https://doi.org/10.1016/0012-821X(90)90006-J.

Hayward, N., 2015, Geophysical investigation and reconstruction of lithospheric structure and its control on geology, structure, and mineralization in the Cordillera of northern Canada and eastern Alaska: Tectonics, v. 34, no. 10, p. 2165–2189, https://doi.org/10.1002/2015TC003871.

Henry, C.D., and Aranda-Gomez, J.J., 1992, The real southern Basin and Range: Mid- to late Cenozoic extension in Mexico: Geology, v. 20, no. 8, p. 701–704, https://doi.org/10.1130/0091-7613(1992)020<0701:TRSBAR>2.3.CO;2.

Humphreys, E.R., and Niu, Y., 2009, On the composition of ocean island basalts (OIB): The effects of lithospheric thickness variation and mantle metasomatism: Lithos, v. 112, no. 1–2, p. 118–136, https://doi.org/10.1016/j.lithos.2009.04.038.

Isakson, V.H., Schmitz, M.D., Dehler, C.M., Macdonald, F.A., and Yonkee, A.W., 2022, A robust age model for the Cryogenian Pocatello Formation of southeastern Idaho (northwestern USA) from tandem in situ and isotope dilution U-Pb dating of volcanic tuffs and epiclastic detrital zircons: Geosphere, v. 18, no. 2, p. 825–849, https://doi.org/10.1130/GES02437.1.

Jaffey, A.H., Flynn, K.F., Glendenin, L.E., Bentley, W.C., and Essling, A.M., 1971, Precision measurement of half-lives and specific activities of ^{235}U and ^{238}U: Physical Review C, v. 4, no. 5, p. 1889–1906, https://doi.org/10.1103/PhysRevC.4.1889.

Jagoutz, O., Müntener, O., Manatschal, G., Rubatto, D., Péron-Pinvidic, G., Turrin, B.D., and Villa, I.M., 2007, The rift-to-drift transition in the North Atlantic: A stuttering start of the MORB machine?: Geology, v. 35, no. 12, p. 1087–1090, https://doi.org/10.1130/G23613A.1.

Jenner, G.A., 1996, Trace element geochemistry of igneous rocks: Geochemical nomenclature and analytical geochemistry, *in* Wyman, D.A., ed., Trace Element Geochemistry of Volcanic Rocks: Applications for Massive Sulfide Exploration: Geological Association of Canada, Short Course Notes, v. 12, p. 51–77.

Kay, R.W., and Gast, P.W., 1973, The rare earth content and origin of alkali-rich basalts: The Journal of Geology, v. 81, no. 6, p. 653–682, https://doi.org/10.1086/627919.

Keen, C., Dafoe, L., and Dickie, K., 2014, A volcanic province near the western termination of the Charlie-Gibbs Fracture Zone at the rifted margin, offshore northeast Newfoundland: Tectonics, v. 33, no. 6, p. 1133–1153, https://doi.org/10.1002/2014TC003547.

Keller, M., Cooper, J.D., and Lehnert, O., 2012, Sauk megasequence supersequences, southern Great basin: Second-order accommodation events on the southwestern Cordilleran margin platform, *in* Derby, J.R., Longacre, S.A., Morgan, M.A., and Sternbach, C.A., eds., The Great American Carbonate Bank: The Geology and Economic Resources of the Cambrian–Ordovician Sauk Megasequence of Laurentia: American Association of Petroleum Geologists Memoir 98, p. 873–896, https://doi.org/10.1306/13331519M983514.

Larson, E., Patterson, P., Curtis, G., Drake, K., and Mutschler, F., 1985, Petrologic, paleomagnetic, and structural evidence of a Paleozoic rift system in Oklahoma, New Mexico, Colorado, and Utah: Geological Society of America Bulletin, v. 96, p. 1364–1372, https://doi.org/10.1130/0016-7606(1985)96<1364:PPASEO>2.0.CO;2.

Lesher, C., Gibson, H., and Campbell, I., 1986, Composition-volume changes during hydrothermal alteration of andesite at Buttercup Hill, Noranda District, Quebec: Geochimica et Cosmochimica Acta, v. 50, no. 12, p. 2693–2705, https://doi.org/10.1016/0016-7037(86)90219-X.

Leslie, C.D., 2009, Detrital zircon geochronology and rift-related magmatism: Central Mackenzie Mountains, Northwest Territories [M.Sc. thesis]: Vancouver, University of British Columbia, 224 p.

Li, Z.X., Bogdanova, S., Collins, A.S., Davidson, A., De Waele, B., Ernst, R.E., Fitzsimons, I.C.W., Fuck, R.A., Gladkochub, D.P., Jacobs, J., and Karlstrom, K.E., 2008, Assembly, configuration, and break-up history of Rodinia: A synthesis: Precambrian Research, v. 160, no. 1–2, p. 179–210, https://doi.org/10.1016/j.precamres.2007.04.021.

Lister, G., Etheridge, M., and Symonds, P., 1986, Detachment faulting and the evolution of passive continental margins: Geology, v. 14, no. 3, p. 246–250, https://doi.org/10.1130/0091-7613(1986)14<246:DFATEO>2.0.CO;2.

Logan, J.M., and Colpron, M., 2006, Stratigraphy, geochemistry, syngenetic sulphide occurrences and tectonic setting of the lower Paleozoic Lardeau Group, northern Selkirk Mountains, British Columbia, *in* Colpron, M., and Nelson, J.A., eds., Paleozoic Evolution and Metallogeny of Pericratonic Terranes at the Ancient Pacific Margin of North America, Canadian and Alaskan Cordillera: Geological Association of Canada Special Paper 45, p. 361–382.

Ludwig, K.R., 2003, User's Manual for Isoplot 3.00: A Geochronological Toolkit for Microsoft Excel: Berkeley Geochronology Center Special Publication 4.

Lund, K., 2008, Geometry of the Neoproterozoic and Paleozoic rift margin of western Laurentia: Implications for mineral deposit settings: Geosphere, v. 4, no. 2, p. 429–444, https://doi.org/10.1130/GES00121.1.

Lund, K., Aleinikoff, J.N., Evans, K.V., and Fanning, C.M., 2003, SHRIMP U-Pb geochronology of Neoproterozoic Windermere Supergroup, central Idaho: Implications for rifting of western Laurentia and synchroneity of Sturtian glacial deposits: Geological Society of America Bulletin, v. 115, no. 3, p. 349–372, https://doi.org/10.1130/0016-7606(2003)115<3C0349:SUPGON>3E2.0.CO;2.

Lund, K., Aleinikoff, J., Evans, K., DuBray, E., Dewitt, E., and Unruh, D., 2010, SHRIMP U-Pb dating of recurrent Cryogenian and Late Cambrian–Early Ordovician alkalic magmatism in central Idaho: Implications for Rodinian rift tectonics: Geological Society of America Bulletin, v. 122, no. 3–4, p. 430–453, https://doi.org/10.1130/B26565.1.

Macdonald, F.A., Yonkee, W.A., Flowers, R.M., and Swanson-Hysell, N.L., 2023, Neoproterozoic of Laurentia: Turning points in the evolution of a continent, *in* Whitmeyer, S.J., Williams, M.L., Kellett, D.A., and Tikoff, B., eds., Laurentia: Turning Points in the Evolution of a Continent: Geological Society of America Memoir 220, p. 331–380, https://doi.org/10.1130/2022.1220(19).

MacIntyre, D.G., 1998, Geology, geochemistry and mineral deposits of the Akie River area, northeast British Columbia: British Columbia Geological Survey Branch Bulletin 103, 91 p.

MacLean, W., 1990, Mass change calculations in altered rock series: Mineralium Deposita, v. 25, no. 1, p. 44–49, https://doi.org/10.1007/BF03326382.

MacNaughton, R.B., Moynihan, D.P., Roots, C.F., and Crowley, J.L., 2016, New occurrences of Oldhamia in eastern Yukon, Canada: Stratigraphic context and implications for Cambrian deep-marine biostratigraphy: Ichnos, v. 23, no. 1–2, p. 33–52, https://doi.org/10.1080/10420940.2015.1127232.

Manatschal, G., 2004, New models for evolution of magma-poor rifted margins based on a review of data and concepts from West Iberia and the Alps: International Journal of Earth Sciences, v. 93, no. 3, p. 432–466, https://doi.org/10.1007/s00531-004-0394-7.

Mandler, B.E., and Grove, T.L., 2016, Controls on the stability and composition of amphibole in the Earth's mantle: Contributions to Mineralogy and Petrology, v. 171, no. 8–9, https://doi.org/10.1007/s00410-016-1281-5.

McDonough, W.S., 1990, Constraints on the composition of the continental lithospheric mantle: Earth and Planetary Science Letters, v. 101, no. 1, p. 1–18, https://doi.org/10.1016/0012-821X(90)90119-I.

McKenzie, D., and Bickle, M., 1988, The volume and composition of melt generated by extension of the lithosphere: Journal of Petrology, v. 29, no. 3, p. 625–679, https://doi.org/10.1093/petrology/29.3.625.

McMechan, M., Currie, L., Ferri, F., Matthews, W., and O'Sullivan, P., 2017, Cambrian detrital zircon signatures of the northern Cordilleran passive margin, Liard area, Canada: Evidence of sediment recycling, non-Laurentian ultimate sources, and basement denudation: Canadian Journal of Earth Sciences, v. 54, no. 6, p. 609–621, https://doi.org/10.1139/cjes-2016-0127.

McPhie, J., Doyle, M., and Allen, R., 1993, Volcanic Textures: A Guide to the Interpretation of Textures in Volcanic Rocks: Centre for Ore Deposit and Exploration Studies, University of Tasmania, 196 p.

Milton, J.E., Hickey, K.A., Gleeson, S.A., and Friedman, R.M., 2017, New U-Pb constraints on the age of the Little Dal Basalts and Gunbarrel-related volcanism in Rodinia: Precambrian Research, v. 296, p. 168–180, https://doi.org/10.1016/j.precamres.2017.04.030.

Moynihan, D.P., Strauss, J.V., Nelson, L.L., and Padget, C.D., 2019, Upper Windermere Supergroup and the transition from rifting to continent-margin sedimentation, Nadaleen River area, northern Canadian Cordillera: Geological Society of America Bulletin, v. 131, no. 9–10, p. 1673–1701, https://doi.org/10.1130/B32039.1.

Norford, B., 1990, Ordovician and Silurian stratigraphy, paleogeography and depositional history in the Peace River Arch area, Alberta and British Columbia: Bulletin of Canadian Petroleum Geology, v. 38, no. 1, p. 45–54.

O'Connell, S.C., Dix, G.R., and Barclay, J.E., 1990, The origin, history, and regional structural development of the Peace River Arch, Western Canada: Bulletin of Canadian Petroleum Geology, v. 38, no. 1, p. 4–24.

Pe-Piper, G., Jansa, L., and Palacz, Z., 1994, Geochemistry and regional significance of the Early Cretaceous bimodal basalt-felsic associations on Grand Banks, eastern Canada: Geological Society of America Bulletin, v. 106, p. 1319–1331, https://doi.org/10.1130/0016-7606(1994)106<1319:GARSOT>2.3.CO;2.

Pe-Piper, G., Meredyk, S., Zhang, Y., Piper, D.J., and Edinger, E., 2013, Petrology and tectonic significance of seamounts within transitional crust east of Orphan Knoll, offshore eastern Canada: Geo-Marine Letters, v. 33, p. 433–447, https://doi.org/10.1007/s00367-013-0342-2.

Pearce, J.A., 1996, A user's guide to basalt discrimination diagrams, *in* Wyman, D.A., ed., Trace Element Geochemistry of Volcanic Rocks: Applications for Massive Sulphide Exploration: Geological Association of Canada, Short Course Notes, v. 12, p. 79–113.

Pearce, J.A., 2008, Geochemical fingerprinting of oceanic basalts with applications to ophiolite classification and the search for Archean oceanic crust: Lithos, v. 100, no. 1–4, p. 14–48, https://doi.org/10.1016/j.lithos.2007.06.016.

Pearce, J.A., 2014, Immobile element fingerprinting of ophiolites: Elements, v. 10, no. 2, p. 101–108, https://doi.org/10.2113/gselements.10.2.101.

Pearce, J.A., and Peate, D.W., 1995, Tectonic implications of the composition of volcanic arc magmas: Annual Review of Earth and Planetary Sciences, v. 23, p. 251–285, https://doi.org/10.1146/annurev.ea.23.050195.001343.

Peate, D.W., and Hawkesworth, C.J., 1996, Lithospheric to asthenospheric transition in low-Ti flood basalts from southern Parana, Brazil: Chemical Geology, v. 127, no. 1–3, p. 1–24, https://doi.org/10.1016/0009-2541(95)00086-0.

Peron-Pinvidic, G., Shillington, D.J., and Tucholke, B.E., 2010, Characterization of sills associated with the U reflection on the Newfoundland margin: Evidence for widespread early post-rift magmatism on a magma-poor rifted margin: Geophysical Journal International, v. 182, no. 1, p. 113–136, https://doi.org/10.1111/j.1365-246X.2010.04635.x.

Peron-Pinvidic, G., Manatschal, G., and Osmundsen, P.T., 2013, Structural comparison of archetypal Atlantic rifted margins: A review of observations and concepts: Marine and Petroleum Geology, v. 43, p. 21–47, https://doi.org/10.1016/j.marpetgeo.2013.02.002.

Perry, F.V., Baldridge, W.S., and DePaolo, D.J., 1987, Role of asthenosphere and lithosphere in the genesis of late Cenozoic basaltic rocks from the Rio Grande rift and adjacent regions of the southwestern United States: Journal of Geophysical Research: Solid Earth, v. 92, no. B9, p. 9193–9213, https://doi.org/10.1029/JB092iB09p09193.

Piercey, S.J., and Colpron, M., 2009, Composition and provenance of the Snowcap assemblage, basement to the Yukon-Tanana terrane, northern Cordillera: Implications for Cordilleran crustal growth: Geosphere, v. 5, no. 5, p. 439–464, https://doi.org/10.1130/GES00505.S3.

Piercey, S.J., Mortensen, J.K., Murphy, D.C., Paradis, S., and Creaser, R.A., 2002, Geochemistry and tectonic significance of alkalic mafic magmatism in the Yukon-Tanana Terrane, Finlayson Lake Region, Yukon: Canadian Journal of Earth Sciences, v. 39, p. 1729–1744, https://doi.org/10.1139/e02-090.

Piercey, S.J., Nelson, J.L., Colpron, M., Dusel-Bacon, C., Simard, R.-L., and Roots, C.F., 2006, Paleozoic magmatism and crustal recycling along the ancient Pacific margin of North America, northern Cordillera, *in* Colpron, M., and Nelson, J.L., eds., Paleozoic Evolution and Metallogeny of Pericratonic Terranes at the Ancient Pacific Margin of North America, Canadian and Alaskan Cordillera: Geological Association of Canada Special Paper 45.

Piercey, S.J., Murphy, D.C., and Creaser, R.A., 2012, Lithosphere-asthenosphere mixing in a transform-dominated late Paleozoic backarc basin: Implications for northern Cordilleran crustal growth and assembly: Geosphere, v. 8, no. 3, p. 716–739, https://doi.org/10.1130/GES00757.1.

Pigage, L., Crowley, J., Pyle, L., Abbott, J., Roots, C., and Schmitz, M., 2012, U–Pb zircon age of an Ordovician tuff in southeast Yukon: Implications for the age of the Cambrian–Ordovician boundary: Canadian Journal of Earth Sciences, v. 49, no. 6, p. 732–741, https://doi.org/10.1139/e2012-017.

Pigage, L., Roots, C., and Abbott, J., 2015, Regional bedrock geology for Coal River map area (NTS 95D), southeast Yukon: Yukon Geological Survey Bulletin, v. 17, 167 p.

Pigage, L.C., 2004, Bedrock geology compilation of the Anvil District (parts of 105K/2, 3, 5, 6, 7 and 11), central Yukon: Yukon Geological Survey Bulletin 15, 103 p.

Poole, F.G., Stewart, J.H., Palmer, A.R., Sandberg, C.A., Madrid, R.J., Ross, R.J., Jr., Hintze, L.F., Miller, M.M., and Wrucke, C.T., 1992, Latest Precambrian to latest Devonian time; Development of a continental margin; Chapter 2, *in* Burchfiel, B.C., Lipman, P.W., and Zoback, M.L., eds., The Cordilleran Orogen: Conterminous U.S.: Boulder, Colorado, Geological Society of America, Geology of North America, v. G-3, p. 9–56, https://doi.org/10.1130/DNAG-GNA-G3.9.

Price, R.A., and Sears, J.W., 2000, A preliminary palinspastic map of the mesoproterozoic belt-purcell supergroup, Canada and USA: Implications for the tectonic setting and structural evolution of the purcell anticlinorium and the Sullivan deposit, *in* Lydon, J.W., Hoy, T., Slack, J.F., and Kapp, M.E., eds., The Geological Environment of the Sullivan Deposit, British Columbia: Geological Association of Canada, Mineral Deposits Division, Special Paper 1, p. 61–81.

Pyle, L.J., and Barnes, C.R., 2003, Lower Paleozoic stratigraphic and biostratigraphic correlations in the Canadian Cordillera: Implications for the tectonic evolution of the Laurentian margin: Canadian Journal of Earth Sciences, v. 40, no. 12, p. 1739–1753, https://doi.org/10.1139/e03-049.

Read, P.B., Woodsworth, G.J., Greenwood, H.J., Ghent, E.D., and Evenchick, C.A., 1991, Metamorphic map of the Canadian Cordillera: Geological Survey of Canada, scale 1:2,000,000.

Roex, A.P., Späth, A., and Zartman, R.E., 2001, Lithospheric thickness beneath the southern Kenya Rift: Implications from basalt geochemistry: Contributions to Mineralogy and Petrology, v. 142, no. 1, p. 89–106, https://doi.org/10.1007/s004100100273.

Rogers, N., 2015, The composition and origin of magmas, *in* Sigurdsson, H., et al., eds., The Encyclopedia of Volcanoes: Elsevier, p. 93–112, https://doi.org/10.1016/B978-0-12-385938-9.00004-3.

Roots, C.F., 1988, Cambro-Ordovician volcanic rocks in Eastern Dawson map-area, Ogilvie Mountains, Yukon, Indian and Northern Affairs Canada, p. 81–87.

Roots, C.F., 2003, Bedrock geology of Lansing Range map area (NTS 105N), central Yukon: Yukon Geological Survey Geoscience Map 2003–1, scale 1:250,000.

Ruks, T.W., Piercey, S.J., Ryan, J.J., Villeneuve, M.E., and Creaser, R.A., 2006, Mid- to late Paleozoic K-feldspar augen granitoids of the Yukon-Tanana terrane, Yukon, Canada: Implications for crustal growth and tectonic evolution of the northern Cordillera: Geological Society of America Bulletin, v. 118, no. 9–10, p. 1212–1231, https://doi.org/10.1130/B25854.1.

Shervais, J.W., 2022, The petrogenesis of modern and ophiolitic lavas reconsidered: Ti-V and Nb-Th: Geoscience Frontiers, v. 13, no. 2, https://doi.org/10.1016/j.gsf.2021.101319.

Shinjo, R., Chung, S.L., Kato, Y., and Kimura, M., 1999, Geochemical and Sr-Nd isotopic characteristics of volcanic rocks from the Okinawa trough and Ryukyu arc: Implications for the evolution of a young, intracontinental back arc basin: Journal of Geophysical Research: Solid Earth, v. 104, no. B5, p. 10,591–10,608, https://doi.org/10.1029/1999JB900040.

Smith, T.L., and Batiza, R., 1989, New field and laboratory evidence for the origin of hyaloclastite flows on seamount summits: Bulletin of Volcanology, v. 51, p. 96–114, https://doi.org/10.1007/BF01081979.

Soares, D.M., Alves, T.M., and Terrinha, P., 2012, The breakup sequence and associated lithospheric breakup surface: Their significance in the context of rifted continental margins (West Iberia and Newfoundland margins, North Atlantic): Earth and Planetary Science Letters, v. 355–356, p. 311–326, https://doi.org/10.1016/j.epsl.2012.08.036.

Sohn, R.A., Willis, C., Humphris, S., Shank, T.M., Singh, H., Edmonds, H.N., Kunz, C., Hedman, U., Helmke, E., Jakuba, M., Liljebladh, B., Linder, J., Murphy, C., Nakamura, K.-i., Sato, T., Schlindwein, V., Stranne, C., Tausenfreund, M., Upchurch, L., Winsor, P., Jakobsson, M., and Soule, A., 2008, Explosive volcanism on the ultraslow-spreading Gakkel ridge, Arctic Ocean: Nature, v. 453, p. 1236–1238, https://doi.org/10.1038/nature07075.

Soule, S.A., 2015, Mid-ocean ridge volcanism, *in* Sigurdsson, H., et al., eds., The Encyclopedia of Volcanoes: Elsevier, p. 395–403, https://doi.org/10.1016/B978-0-12-385938-9.00021-3.

Spitz, G., and Darling, R., 1978, Major and minor element lithogeochemical anomalies surrounding the Louvem copper deposit, Val d'Or, Quebec: Canadian Journal of Earth Sciences, v. 15, no. 7, p. 1161–1169, https://doi.org/10.1139/e78-122.

Staudigel, H., and Koppers, A.A., 2015, Seamounts and island building, *in* Sigurdsson, H., et al., eds., The Encyclopedia of Volcanoes: Elsevier, p. 405–421, https://doi.org/10.1016/B978-0-12-385938-9.00022-5.

Staudigel, H., Koppers, A.A., Lavelle, J.W., Pitcher, T.J., and Shank, T.M., 2010, Defining the word "Seamount": Oceanography, v. 23, no. 1, p. 20–21, https://doi.org/10.5670/oceanog.2010.85.

Sun, S.S., and McDonough, W.F., 1989, Chemical and isotopic systematics of oceanic basalts: Implications for mantle composition and processes, *in* Saunders, A.D., and Norry, M.J., eds., Magmatism in Ocean Basins: Geological Society, London, Special Publication 42, p. 313–345, https://doi.org/10.1144/GSL.SP.1989.042.01.19.

Tanaka, T., Togashi, S., Kamioka, H., Amakawa, H., Kagami, H., Hamamoto, T., Yuhara, M., Orihashi, Y., Yoneda, S., and Shimizu, H., 2000, JNdi-1: A neodymium isotopic reference in consistency with LaJolla neodymium: Chemical Geology, v. 168, p. 279–281, https://doi.org/10.1016/S0009-2541(00)00198-4.

Thomas, W., 2014, A mechanism for tectonic inheritance at transform faults of the Iapetan margin of Laurentia: Geoscience Canada, v. 41, no. 3, p. 321–344, https://doi.org/10.12789/geocanj.2014.41.048.

Tucholke, B.E., Sawyer, D.S., and Sibuet, J.-C., 2007, Breakup of the Newfoundland-Iberia rift, *in* Karner, G., Manatschal, G., and Pinheiro, L.D., eds., Imaging, Mapping and Modelling Continental Lithosphere Extension and Breakup: Geological Society, London, Special Publication 282, p. 9–46.

Turner, R.J.W., Madrid, R.J., and Miller, E.L., 1989, Roberts Mountains allochthon: Stratigraphic comparison with lower Paleozoic outer continental margin strata of the northern Canadian Cordillera: Geology, v. 17, p. 341–344, https://doi.org/10.1130/0091-7613(1989)017<0341:RMASCW>2.3.CO;2.

van Staal, C.R., Winchester, J.A., and Bédard, J.H., 1991, Geochemical variations in Middle Ordovician volcanic rocks of the northern Miramichi Highlands and their tectonic significance: Canadian Journal of Earth Sciences, v. 28, p. 1031–1049, https://doi.org/10.1139/e91-094.

Vervoort, J.D., and Blichert-Toft, J., 1999, Evolution of the depleted mantle: Hf isotope evidence from juvenile rocks through time: Geochimica et Cosmochimica Acta, v. 63, no. 3–4, p. 533–556, https://doi.org/10.1016/S0016-7037(98)00274-9.

Wallace, M., and Green, D., 1991, The effect of bulk rock composition on the stability of amphibole in the upper mantle: Implications for solidus positions and mantle metasomatism: Mineralogy and Petrology, v. 44, no. 1–2, p. 1–19, https://doi.org/10.1007/BF01167097.

Watkins, R., and Browne, Q.J., 1989, An Ordovician continental-margin sequence of turbidite and seamount deposits in the Roberts Mountain allochthon, Independence Range, Nevada: Geological Society of America Bulletin, v. 101, p. 731–741, https://doi.org/10.1130/0016-7606(1989)101<0731:AOCMSO>2.3.CO;2.

Weis, D., Kieffer, B., Maerschalk, C., Barling, J., De Jong, J., Williams, G.A., Hanano, D., Pretorius, W., Mattielli, N., and Scoates, J.S., 2006, High-precision isotopic characterization of USGS reference materials by TIMS and MC-ICP-MS: Geochemistry, Geophysics, Geosystems, v. 7, no. 8, https://doi.org/10.1029/2006GC001283.

Weis, D., Kieffer, B., Hanano, D., Nobre Silva, I., Barling, J., Pretorius, W., Maerschalk, C., and Mattielli, N., 2007, Hf isotope compositions of US Geological Survey reference materials: Geochemistry, Geophysics, Geosystems, v. 8, no. 6, https://doi.org/10.1029/2006GC001473.

Wernicke, B., 1985, Uniform-sense normal simple shear of the continental lithosphere: Canadian Journal of Earth Sciences, v. 22, no. 1, p. 108–125, https://doi.org/10.1139/e85-009.

White, J.D., McPhie, J., and Soule, S.A., 2015, Submarine lavas and hyaloclastite, *in* Sigurdsson, H., et al., eds., The Encyclopedia of Volcanoes: Elsevier, p. 363–375, https://doi.org/10.1016/B978-0-12-385938-9.00019-5.

White, R., and McKenzie, D., 1995, Mantle plumes and flood basalts: Journal of Geophysical Research: Solid Earth, v. 100, no. B9, p. 17,543–17,585, https://doi.org/10.1029/95JB01585.

Whitford, D.J., McPherson, W.P., and Wallace, D.B., 1989, Geochemistry of the host rocks of the volcanogenic massive sulfide deposit at Que River, Tasmania: Economic Geology, v. 84, no. 1, p. 1–21, https://doi.org/10.2113/gsecongeo.84.1.1.

Whitmarsh, R., Manatschal, G., and Minshull, T., 2001, Evolution of magma-poor continental margins from rifting to seafloor spreading: Nature, v. 413, no. 6852, p. 150–154, https://doi.org/10.1038/35093085.

Wyld, S.J., Umhoefer, P.J., and Wright, J.E., 2006, Reconstructing northern Cordilleran terranes along known Cretaceous and Cenozoic strike-slip faults: Implications for the Baja British Columbia hypothesis and other models, *in* Haggart, J.W., Enkin, R.J., and Monger, J.W.H., eds., Paleogeography of the North American Cordillera: Evidence for and against Large-Scale Displacements: Geological Association of Canada Special Paper 46, p. 277–298.

Yonkee, W., Dehler, C., Link, P.K., Balgord, E., Keeley, J.A., Hayes, D., Wells, M., Fanning, C., and Johnston, S., 2014, Tectono-stratigraphic framework of Neoproterozoic to Cambrian strata, west-central US: Protracted rifting, glaciation, and evolution of the North American Cordilleran margin: Earth-Science Reviews, v. 136, p. 59–95, https://doi.org/10.1016/j.earscirev.2014.05.004.

Yukon Geological Survey, 2022, Yukon geochronology—A database of Yukon isotopic age determinations, Yukon Geological Survey: http://data.geology.gov.yk.ca/Compilation/22 (accessed September 2022).

Zhao, F., Berndt, C., Alves, T.M., Xia, S., Li, L., Mi, L., and Fan, C., 2021, Widespread hydrothermal vents and associated volcanism record prolonged Cenozoic magmatism in the South China Sea: Geological Society of America Bulletin, v. 133, p. 2645–2660, https://doi.org/10.1130/B35897.1.